

Exploring Molecular Complexity with ALMA (EMoCA): Deuterated complex organic molecules in Sagittarius B2(N2)

A. Belloche¹, H. S. P. Müller², R. T. Garrod³, and K. M. Menten¹

¹ Max-Planck-Institut für Radioastronomie, Auf dem Hügel 69, 53121 Bonn, Germany
e-mail: belloche@mpi-fr-bonn.mpg.de

² I. Physikalisches Institut, Universität zu Köln, Zùlpicher Str. 77, 50937 Köln, Germany

³ Depts. of Astronomy and Chemistry, University of Virginia, Charlottesville, VA 22904, USA

Received 28 August 2015; accepted 16 November 2015

ABSTRACT

Context. Deuteration is a powerful tracer of the history of the cold prestellar phase in star forming regions. Apart from methanol, little is known about deuterium fractionation of complex organic molecules in the interstellar medium, especially in high mass star forming regions.

Aims. Our goal is to detect deuterated complex organic molecules toward the high mass star forming region Sagittarius B2 (Sgr B2) and derive their level of deuteration.

Methods. We use a complete 3 mm spectral line survey performed with the Atacama Large Millimeter/submillimeter Array (ALMA) to search for deuterated complex organic molecules toward the hot molecular core Sgr B2(N2). Population diagrams and integrated intensity maps are constructed to fit rotational temperatures and emission sizes for each molecule. Column densities are derived by modelling the full spectrum under the assumption of local thermodynamic equilibrium. The results are compared to predictions of two astrochemical models that treat the deuteration process.

Results. We report the detection of CH₂DCN toward Sgr B2(N2) with a deuteration level of 0.4%, and tentative detections of CH₂DOH, CH₂DCH₂CN, the chiral molecule CH₃CHDCN, and DC₃N with levels in the range 0.05%–0.12%. A stringent deuteration upper limit is obtained for CH₃OD (< 0.07%). Upper limits in the range 0.5–1.8% are derived for the three deuterated isotopologues of vinyl cyanide, the four deuterated species of ethanol, and CH₂DOCHO. Ethyl cyanide is less deuterated than methyl cyanide by at least a factor five. The [CH₂DOH]/[CH₃OD] abundance ratio is higher than 1.8. It may still be consistent with the value obtained in Orion KL. Except for methyl cyanide, the measured deuteration levels lie at least a factor four below the predictions of current astrochemical models. The deuteration levels in Sgr B2(N2) are also lower than in Orion KL by a factor of a few up to a factor ten.

Conclusions. The discrepancy between the deuteration levels of Sgr B2(N2) and the predictions of chemical models, and the difference between Sgr B2(N2) and Orion KL may both be due to the higher kinetic temperatures that characterize the Galactic Center region compared to nearby clouds. Alternatively, they may result from a lower overall abundance of deuterium itself in the Galactic Center region by up to a factor ten.

Key words. astrochemistry – line: identification – stars: formation – ISM: individual objects: Sagittarius B2 – ISM: molecules

1. Introduction

Deuteration is a powerful tracer of the history of the cold prestellar phase in star forming regions (see, e.g., Caselli & Ceccarelli 2012; Ceccarelli et al. 2014). At low temperatures and high densities that prevail in prestellar cores, the gas-phase abundance of H₃⁺ gets enhanced thanks to the depletion of its main destroyer, CO, onto the surface of dust grains. The reaction of H₃⁺ with HD, the reservoir of deuterium in molecular clouds, produces H₂D⁺. The exothermicity of this reaction leads to an enhancement of the [H₂D⁺]/[H₃⁺] abundance ratio. The reaction of H₂D⁺ with other molecules then transfers the deuterium to other species, producing a significant increase in their deuterium fractionation that can reach several orders of magnitude compared to the low cosmic abundance of deuterium with respect to hydrogen (~ 1.5 × 10⁻⁵, Linsky 2003). Deuteration levels – i.e. the abundance ratio [XD]/[XH] of a deuterated molecule XD to the corresponding hydrogen-bearing one XH – above 10% are commonly found in low-mass star forming regions (e.g., Parise et al. 2006). Even molecules containing several deuterium atoms have been detected (e.g., Parise et al. 2004). Levels of deuteration

above 10% have also been found for small molecules such as ammonia in high mass star forming regions (Pillai et al. 2007; Fontani et al. 2015). Deuteration at somewhat higher temperatures (~ 30–50 K), at which the H₂D⁺ channel is not efficient anymore, can also occur in the gas phase via CH₂D⁺ which is, like H₂D⁺, produced by an exothermic reaction of CH₃⁺ with HD (e.g., Parise et al. 2009).

The overall increase in the deuterium fractionation of molecules in cold, prestellar cores leads to an abundance enhancement of atomic deuterium in the gas phase. These atoms can stick to the surface of dust grains and in turn participate in the deuterium fractionation of molecules already or subsequently formed on these grains, in particular of the complex organic ones¹. Once a protostar is formed, the energy it radiates heats up its circumstellar envelope and complex organic molecules desorb from the grain surfaces (e.g., Garrod et al. 2008). During this hot core phase, the relative abundances of these freshly desorbed molecules is expected to provide clues about their for-

¹ We adopt the definition of Herbst & van Dishoeck (2009): a complex organic molecule is an organic molecule containing six atoms or more.

mation paths during the past evolution of the core. In particular, their degree of deuterium fractionation is a relic of the conditions that were prevailing in earlier, colder stages (e.g. Taquet et al. 2012, 2014; Aikawa et al. 2012).

Apart from methanol, relatively little is known about deuteration of complex organic molecules in the interstellar medium, in particular in high mass star forming regions. A few detections or tentative detections of deuterated (complex) organic molecules have been reported toward Orion KL (Gerin et al. 1992; Daly et al. 2013; Esplugues et al. 2013; Neill et al. 2013; Coudert et al. 2013), but no systematic study of the deuteration of complex organic molecules in high mass star forming regions has been reported so far.

Sagittarius B2, hereafter Sgr B2, is one of the most massive star forming regions in the Galaxy. It is located in the Central Molecular Zone, close to the Galactic Center. Its current star formation rate qualifies Sgr B2 as a mini-starburst region (see, e.g., Appendix A of Belloche et al. 2013). The cloud contains several sites of on-going high-mass star formation. One of them, Sgr B2(N), contains two hot molecular cores that we name here Sgr B2(N1) and (N2)². Their angular separation is 5'' in the north-south direction, corresponding to 0.2 pc in projection at a distance of 8.3 kpc (Reid et al. 2014). Their velocities projected along the line of sight differ by 9–10 km s⁻¹. Both are characterized by extremely high H₂ column densities ($> 10^{25}$ cm⁻² over few arcsec, see Belloche et al. 2008, 2014; Qin et al. 2011). They are both in an early stage of star formation when a (massive) protostar has already formed and started to heat up its circumstellar envelope. The high kinetic temperatures of the hot cores (~ 150 –200 K) lead to the sublimation of molecules that formed in the ice mantles of dust grains during the prestellar phase and the warming-up period of the protostellar phase. As a result of both the high temperatures and column densities, numerous complex organic molecules have been detected toward Sgr B2(N) – many of them for the first time in the interstellar medium – since the beginning of radioastronomy nearly five decades ago.

Following up a molecular line survey of Sgr B2(N) performed with the IRAM 30 m telescope that led to the first detection in space of a few new complex organic molecules (Belloche et al. 2008, 2009, 2013), we performed a systematic line survey of Sgr B2(N) in the 3 mm atmospheric window at high angular resolution and sensitivity with the Atacama Large Millimeter/submillimeter Array (ALMA) in its Cycles 0 and 1. This survey is called EMOCA, which stands for “Exploring Molecular Complexity with ALMA”. It aims at investigating molecular complexity in the interstellar medium. One of the initial results of EMOCA was the first interstellar detection of a branched alkyl molecule (Belloche et al. 2014). Here, we take advantage of this sensitive survey to explore, for the first time in a systematic way, the deuterium fractionation of complex organic molecules in Sgr B2(N2). We focus on Sgr B2(N2) rather than the main hot core Sgr B2(N1) because the former has relatively narrow linewidths (~ 5 km s⁻¹) at the angular resolution of EMOCA ($\sim 1.8''$) while the latter still has prominent linewidths like in our previous single-dish survey. A companion paper reports on the detection of alkanols and alkanethiols based on EMOCA (Müller et al. 2015c).

The article is structured as follows. The observational setup and the process of data reduction are described in Sect. 2. Section 3 explains the method employed to model the observed

spectra in the approximation of local thermodynamic equilibrium and Sect. 4 gives some details about the spectroscopic predictions used to generate the synthetic spectra. The results of the analysis are reported in Sect. 5 and discussed in Sect. 6. Section 7 gives our conclusions about deuterium fractionation of complex organic molecules in Sgr B2(N2).

2. Observations and data reduction

2.1. Observations

We used the Atacama Large Millimeter/submillimeter Array (ALMA) to perform a complete spectral line survey toward Sgr B2(N) between 84.1 and 114.4 GHz. The field was centered at $(\alpha, \delta)_{J2000} = (17^h47^m19.87^s, -28^\circ22'16'')$, half way between Sgr B2(N1) and (N2) that are separated by 4.9'' in the north-south direction. The size (HPBW) of the primary beam of the 12 m antennas varies between 69'' at 84 GHz and 51'' at 114 GHz (Remijan et al. 2015).

The spectral line survey was divided into five spectral setups. Each setup was observed in one polarisation and delivered four spectral windows, two per sideband. The separation between the centers of the lower and upper sidebands is 12 GHz. Each spectral window has a bandwidth of 1875 MHz and a channel spacing of 244.141 kHz, but the spectra were smoothed to a spectral resolution of 488.3 kHz (1.7 to 1.3 km s⁻¹). Each pair of adjacent spectral windows has an overlap of about 50 MHz. Details about the frequency coverage, the date of observation, the number of antennas, the range of baselines, the on-source integration time, and the bandpass, amplitude, and phase calibrators are given in Table 1. Setups S1 to S4 were observed in Cycle 0 while setup S5 was observed in Cycle 1. As reported in Table 1, setups S1 and S5 were observed only once, but setups S2, S3, and S4 were observed on several days, between two and four times each.

2.2. Data reduction

The data was calibrated and imaged with CASA. We used version 4.2.0 (r28322) for setups S1 to S4 and version 4.2.1 (r29047) for setup S5. We used the standard procedures provided by the Joint ALMA Observatory to apply the bandpass, amplitude, and phase calibrations. The deconvolution was performed with the *csclean* imager mode and a *Briggs* weighting scheme with a *robust* parameter of 0.5. The cell size was set to 0.3''. In addition, three or four iterations of self-calibration were performed using a strong spectral line detected toward Sgr B2(N1) in each setup. This improved the dynamical range in the resulting images significantly.

The spectra toward Sgr B2(N1) and (N2) are full of lines and close to the confusion limit. It is thus difficult to separate the line emission from the continuum emission in a systematic way for the full data cubes, but it is a necessary step to produce separate line and continuum maps. For each spectral window of each setup, we selected six groups of few channels that seemed to be free of strong line emission. A first-order baseline was fitted to these selected channels and the result of the fit was used to split each data cube into two cubes, one for the line emission and one for the continuum emission. Given the difference in systemic velocity between the two hot cores (~ 10 km s⁻¹, see Belloche et al. 2013), we selected different sets of channels for the northern and southern parts of the field. This process of baseline subtraction was performed with the CLASS software³.

² They were named P1 and P2 in Belloche et al. (2008) and SMA1 and SMA2 in Qin et al. (2011).

³ See <http://www.iram.fr/IRAMFR/GILDAS>.

Table 1. Observational setups of the EMOCA survey.

Setup	Frequency range		Date of observation yyyy-mm-dd	t_{start}^a (UTC) hh:mm	N_a^b	Baseline range ^c m	t_{int}^d min	Calibrators ^e			Peak ^f	
	LSB GHz	USB GHz						B	A	P	$\Delta\alpha$ "	$\Delta\delta$ "
S1	84.1–87.8	96.2–99.8	2012-08-27	01:05	26	17–400	54.7	1	3	2	0.2	–2.4
S2	87.7–91.4	99.7–103.4	2012-06-05	09:03	20	14–392	24.2	1	3	2	1.2*	–2.4
			2012-07-01	07:04	13	25–393	40.0	1	3	2	1.2*	–2.6
			2012-07-03	06:36	21	14–395	48.4	1	3	2	0.6*	–2.3
			2012-09-28	21:57	25	20–387	44.1	1	4	2	0.2	–2.5
S3	91.4–95.1	103.4–107.1	2012-06-06	08:20	18	15–395	40.2	1	3	2	0.7*	–2.4
			2012-06-18	07:29	22	15–395	40.4	1	3	2	0.6*	–2.2
S4	95.0–98.7	107.0–110.7	2012-07-04	05:38	21	17–398	8.1	1	3	2	0.1	–2.3
			2012-08-01	02:32	24	19–442	34.9	1	3	2	0.1	–2.4
			2012-08-10	00:45	26	21–400	35.0	1	3	2	0.2	–2.4
S5	98.7–102.4	110.7–114.4	2014-04-05	06:22	38	15–413	24.4	2	4	5	0.2	–2.4

Notes. ^(a) Start time of observation. ^(b) Number of ALMA 12 m antennas. ^(c) Minimum and maximum projected baseline separations. ^(d) On-source integration time. ^(e) Bandpass (B), amplitude (A), and phase (P) calibrators. The calibrators are: 1: B1730-130, 2: J1700-2610, 3: Neptune, 4: Titan, 5: J1744-3116. ^(f) Offset of the continuum peak position of Sgr B2(N1) with respect to the phase center, in equatorial coordinate system (J2000). Measurement sets with $\Delta\alpha$ differing from 0.1" by more than 0.2" (marked with a ★) are believed to be affected by an astrometric problem.

We checked the accuracy of the relative astrometry between the ten measurement sets by fitting the peak position of the continuum emission toward Sgr B2(N1) using selected channels of the line+continuum data cubes that appeared to be free of line emission. It turns out that the first three measurement sets of setup S2 and both measurement sets of setup S3 are affected by an astrometric problem: the continuum peak of Sgr B2(N1) is shifted by 0.6" to 1.2" in right ascension with respect to all other measurement sets (see Table 1). The dispersion of the peak position in declination is also a bit higher for the former compared to the latter. The average peak position of Sgr B2(N1) in all non-affected measurement sets is at $(\Delta\alpha, \Delta\delta) = (0.15'', -2.40'')$, i.e. $(\alpha, \delta)_{\text{J2000}} = (17^{\text{h}}47^{\text{m}}19.881^{\text{s}}, -28^{\circ}22'18.40'')$. The five affected measurement sets were obtained after transit when the source was setting and the phase calibrator was at low elevation, which lets us think that the shift of the affected measurement sets may be due to an inaccurate calibration of the atmospheric phase fluctuations. As a result, we ignored the affected measurement sets of setup S2 and used only its fourth one. For setup S3, both measurement sets were used but the offset was approximately compensated for by modifying the visibilities of the phase calibrator with the CASA task *fixvis* before the phase calibration. After this correction, the relative positional accuracy of all measurement sets used in this work is on the order of $\pm 0.1''$ in both right ascension and declination.

The measurement sets of setup S3 were merged into one single measurement set with the CASA task *concat* before imaging. The same was done for setup S4. Only one measurement set was used for the other three setups. The size (HPBW) of the synthesized beam and the rms noise level in the final cubes are given in Table 2. The noise level of each spectral window corresponds to the median of the noise levels measured in all channel maps using the procedure *go noise* in GREG³. The noise levels reported in Table 2 were measured in the continuum-subtracted datacubes. They are typically a factor ~ 2 higher in the line+continuum datacubes.

Based on the redundancies of the measurement sets and the spectral overlap between the setups, we estimate the relative calibration uncertainty on the flux density to be on the order of 15%.

3. Radiative transfer modeling of the line survey

We used the input parameters of our LTE model of the IRAM 30 m spectrum of Sgr B2(N) (Belloche et al. 2013) as a starting point to assign the lines detected in the ALMA spectra and model the emission of the detected molecules. Given the high H_2 densities of Sgr B2(N1) and (N2) ($\sim 10^8 \text{ cm}^{-3}$ at arcsecond scale, Belloche et al. 2008, 2014; Qin et al. 2011), the LTE approximation is appropriate. We used the software Weeds (Maret et al. 2011) to produce synthetic LTE spectra that take into account the radiative transfer and the (spectral-window- and measurement-set-dependent) angular resolution of the observations. The modeling was performed for each species separately, and the contributions of all detected species to the emitted spectra were then added linearly to obtain the final synthetic spectrum (hereafter called the full LTE model). This approximation is valid for optically thin lines that overlap in frequency space or for (optically thick or thin) lines of species that are emitted from separated regions within the beam, but it is not correct anymore for frequency-overlapping optically thick lines of species that are cospatial or aligned along the line of sight. In such cases, the synthetic spectrum overestimates the actual line flux density.

The model of each species is defined by five parameters: angular size of the emitting region assumed to be Gaussian, column density, rotational temperature, velocity offset with respect to the assumed systemic velocity of the source, and linewidth (*FWHM*). For a given species, the source size was derived from two-dimensional Gaussian fits to the integrated intensity maps of all transitions that were well detected and found to be free of contamination (based on the full LTE model). The source size was set to the median deconvolved size of all such transitions. The other four parameters were optimized by eye. Population diagrams were constructed based on the transitions that are well detected and not severely contaminated by transitions of other species. In the case where a transition was partially contaminated, the contributions of the contaminating species was removed from the measured integrated intensities, on the basis of the full LTE model. Each population diagram was also corrected for optical depth following the method described in Goldsmith & Langer (1999), using the opacities delivered by Weeds. The population diagrams were used to verify that the ro-

Table 2. Beam sizes and noise levels.

Setup	SPW ^a	Frequency range MHz	Synthesized beam		rms ^c	
			HPBW	P.A. ^b	mJy	
			"×"	°	beam ⁻¹	K
S1	0	84091 – 85966	2.1 × 1.5	–85	3.0	0.16
	1	85904 – 87779	2.0 × 1.5	–83	2.7	0.14
	2	96154 – 98029	1.8 × 1.4	–85	3.0	0.16
	3	97904 – 99779	1.8 × 1.3	–85	3.1	0.16
S2	0	87729 – 89604	1.9 × 1.7	86	3.1	0.15
	1	89554 – 91429	1.8 × 1.6	52	2.8	0.15
	2	99728 – 101602	1.6 × 1.4	48	2.7	0.14
	3	101552 – 103427	1.6 × 1.4	49	2.7	0.14
S3	0	91368 – 93242	2.9 × 1.5	84	3.4	0.12
	1	93193 – 95067	2.8 × 1.5	83	3.1	0.10
	2	103365 – 105239	2.5 × 1.3	82	3.4	0.11
	3	105189 – 107064	2.5 × 1.3	82	3.6	0.12
S4	0	95021 – 96896	1.9 × 1.4	–82	1.9	0.10
	1	96846 – 98720	1.8 × 1.3	–82	1.9	0.10
	2	107019 – 108893	1.7 × 1.2	–83	2.2	0.11
	3	108843 – 110718	1.6 × 1.2	–82	2.3	0.12
S5	0	98672 – 100546	1.8 × 1.4	–76	2.8	0.14
	1	100496 – 102370	1.7 × 1.4	–76	2.7	0.13
	2	110669 – 112543	1.6 × 1.3	–72	3.5	0.17
	3	112494 – 114368	1.6 × 1.2	–77	4.9	0.24

Notes. ^(a) Spectral window. ^(b) Position angle east from north. ^(c) Median rms noise level measured in the channel maps of the continuum-removed data cubes.

tational temperature derived in the course of the (manual) modeling with Weeds made sense.

In the population diagrams corrected for optical depth and contamination, the residual dispersion of the synthetic datapoints (red crosses) results in part from the frequency boundaries set to integrate the intensity. These boundaries are a compromise between covering the line as much as possible and limiting as much as possible the contamination from other species emitting at nearby frequencies. In addition, the correction for optical depth is an approximation, and may also introduce some bias. Finally, another limitation of this fit is that it can be biased by residual contamination remaining even after removal of the contribution of the identified contaminating species. Therefore, we believe that the formal errors on the rotational temperature derived from the fit to the population diagrams do not necessarily represent the true errors on this temperature and should be viewed with caution.

The emission of vibrationally excited states of a given molecule were modeled independently of the vibrational ground state. The emission of isotopologues of a given molecule were also modeled separately.

The physical structure of the source assumed for the modeling is uniform. This may sound simplistic given that temperature and density gradients are expected in the envelope of Sgr B2(N2) (e.g., Rolfs et al. 2011). However, it turns out that, even with such a simple assumption, the spectra of most complex organic molecules detected toward Sgr B2(N2) can be well reproduced so we are confident that the rotational temperatures and column densities derived from our analysis are reliable.

In the following, we count a line of a given species as a “detected” line if its frequency, peak intensity, and width are well reproduced by our model and it is not (or barely) contaminated by emission from other species. As a counter example, a synthetic

line that is consistent with the observed spectrum – i.e. that has a peak intensity simply below the intensity of the detected signal – but would still remain consistent if it were shifted by a frequency offset typically equal to its linewidth is not counted as “detected”. We emphasize that our definition of a “detected” line is very conservative but we believe that it is required to avoid unsecure molecule detections.

The complete list of transitions identified in our survey is presently not available but the interested reader can refer to the list of lines identified in our previous single-dish survey of Sgr B2(N) (Belloche et al. 2013).

4. Spectroscopic predictions

The origin of the spectroscopic predictions used to model the emission of the species reported in Sect. 5 is provided here.

Predictions for the three singly-deuterated species of ethyl cyanide were taken from the catalog of the Cologne Database for Molecular Spectroscopy (CDMS⁴, Müller et al. 2001, 2005) (tags 56509, 56510, and 56511, all version 1). They are based on Margulès et al. (2009). All other ethyl cyanide data were also taken from the CDMS. The main species predictions are based on Brauer et al. (2009) with published data in the range of our survey from Fukuyama et al. (1996). Transition frequencies of the isotopologues containing one ¹³C were taken from Richard et al. (2012), those for the ¹⁵N isotopologue from Margulès et al. (2009). Vibrational corrections to the rotational partition function, and thus to the column density, were derived for the main isotopologue from Heise et al. (1981) and applied to all species. Only limited isotopic data are available. It is safe to assume that differences among the isotopologues are small, most

⁴ See <http://www.cdms.de>.

likely not exceeding a few percent, because of the large number of heavy atoms in the molecule.

Predictions for singly-deuterated methyl cyanide were taken from the CDMS catalog (tag 42511, version 2). This entry is based on Nguyen et al. (2013). Predictions for CH_3CN in its $v_8 = 1$ and 2 excited states are based on preliminary results from Müller et al. (2015a), those in $v_4 = 1$ are preliminary data from a subsequent study (Müller et al., in preparation). Transition frequencies in the range of our study are from Bauer & Maes (1969) and Bauer (1971) for $v_8 = 1$ and 2, respectively. Predictions for isotopic species with ^{15}N or one or two ^{13}C in their ground vibrational states are from the CDMS. They are based on Müller et al. (2009) with transition frequencies in the range of our survey from Demaison et al. (1979). Predictions for ^{13}C isotopologues in their $v_8 = 1$ states are based on preliminary data from Müller et al. (2015b). Vibrational corrections to the partition function were included in the private entries for the main isotopic species. They are now available in Müller et al. (2015a). As the corrections are small, the error by using the values from the main isotopic species also for the other isotopologues is very small, even for CH_2DCN .

Predictions for deuterated vinyl cyanide CH_2CDCN were taken from the molecular spectroscopic database of the Jet Propulsion Laboratory (JPL⁵, Pickett et al. 1998) (tag 54004, version 2). Predictions for *cis*-CHDCHCN and *trans*-CHDCHCN were prepared by us. All predictions are based on Colmont et al. (1997). Predictions for $\text{C}_2\text{H}_3\text{CN}$ and isotopic species with one ^{13}C or with ^{15}N were taken from the CDMS and are based on Müller et al. (2008). Transition frequencies in the range of our survey are mostly from that study. For the main species, they are, to a large extent, also from Baskakov et al. (1996). Predictions for excited states of vinyl cyanide used in the present work are based on Cazzoli & Kisiel (1988) and unpublished data from one of us (HSPM). These data included vibrational corrections which are essentially complete at 200 K. The vibrational energies were gathered from several sources. A recent compilation of low-lying vibrational states is available in Kisiel et al. (2015). It is safe to assume that differences among the isotopologues are small, most likely not exceeding a few percent, because of the large number of heavy atoms in the molecule.

Predictions for deuterated cyanoacetylene were taken from the CDMS catalog (tag 52508, version 2). This entry is based on Spahn et al. (2008). All other cyanoacetylene predictions were also taken from the CDMS. The $v_7 = 1$ predictions of the main species are based on Thorwirth et al. (2000) with data in the range of our survey from Yamada & Creswell (1986). All predictions of isotopologues containing one or two ^{13}C are based on Thorwirth et al. (2001), those for HC_3^{15}N on Fayt et al. (2004). Ground state transition frequencies for singly substituted species in the range of our survey were taken from Creswell et al. (1977). Vibrational contributions to the partition functions of HC_3N and DC_3N can be evaluated from the study of their low-lying vibrational states by Uyemura et al. (1982). Isotopic shifts, in particular of the lowest v_7 mode, are much smaller for ^{13}C or ^{15}N species. Therefore, using vibrational corrections of the main isotopologue introduces small errors for these species.

Predictions for deuterated methanol CH_2DOH were taken from the JPL catalog (tag 33004, version 1). They are based on Pearson et al. (2012) with rest frequencies almost entirely from that study. Using torsional energies from Lauvergnat et al. (2009), we estimate a vibrational correction factor to the par-

tition function of 1.15 at 160 K. For CH_3OD , we prepared a catalog entry based on Anderson et al. (1988), with frequencies updated to the values published in Duan et al. (2003). We estimated the partition function to be 11770 at 150 K and 25550 at 225 K, taking into account torsional energies of CH_3OD in Anderson et al. (1988). Details on other methanol isotopologues are given in Müller et al. (2015c).

Predictions for all singly-deuterated species of ethanol were taken from the CDMS (tags 47515 to 47518, all version 1). They are based on Walters et al. (2015) with rest frequencies almost entirely from that study. All other ethanol analyses were taken from Müller et al. (2015c), and further details can be found there. Conformational and vibrational corrections to the partition function were taken from the main isotopologue for which only data were available. This assumption is reasonable, though errors may not be completely negligible. They are, however, difficult to evaluate.

Predictions for both conformers of CH_2DOCHO were extracted from Table 7 of Coudert et al. (2013) and split into two separate entries. The partition function was taken from their Table 6. It is identical for both entries. Contrary to the CDMS entries for $\text{CH}_2\text{DCH}_2\text{CN}$ and $\text{CH}_2\text{DCH}_2\text{OH}$, this treatment means that the two entries represent a single species with a statistical distribution (the out-of-plane conformer being twice as abundant as the in-plane one). This means that the column density derived for each conformer represents the total column density of the molecule. However, we assumed a statistical distribution (2:1) to compute and report individual column densities in Sect. 5. Predictions for the main isotopologue were taken from the JPL catalog. The entry is based on Ilyushin et al. (2009). Vibrational corrections to the partition function were derived from the ^{13}C species (Favre et al. 2014). These authors provide rotational partition function values at different temperatures as well as detailed vibrational corrections that are complete up to 300 K. The correction factors are 1.59 and 1.23 at 150 K for the deuterated and main isotopic species, respectively. These values differ because values for the deuterated species refer to the ground state only whereas for the main isotopologue contributions of the first excited states were already included.

5. Results

In this section, we report the detection or tentative detection of deuterated complex organic molecules toward Sgr B2(N2). Column density upper limits are also reported for several non-detections. Each subsection first presents the LTE model derived for the main isotopologue and its ^{13}C and/or ^{15}N isotopologues. This model is then used to obtain constraints on the column density of the deuterated species. The rotational temperatures derived from fits to the population diagrams are reported in Table 3 and the parameters of the LTE model used to fit the spectra are listed in Table 4. The analysis toward Sgr B2(N2) was performed at the offset position $(\Delta\alpha, \Delta\delta) = (-0.1'', 2.6'')$, i.e. $(\alpha, \delta)_{\text{J2000}} = (17^{\text{h}}47^{\text{m}}19.86^{\text{s}}, -28^{\circ}22'13.4'')$.

5.1. Deuterated ethyl cyanide $\text{CH}_2\text{DCH}_2\text{CN}$ and CH_3CHDCN

About 154, 54, 38, and 37 lines of ethyl cyanide and its singly-substituted ^{13}C isotopologues, $^{13}\text{CH}_3\text{CH}_2\text{CN}$, $\text{CH}_3^{13}\text{CH}_2\text{CN}$, and $\text{CH}_3\text{CH}_2^{13}\text{CN}$, respectively, are detected toward Sgr B2(N2) (Figs. 1, 2, 3, and 4). The ^{15}N isotopologue is also detected unambiguously, with 9 detected lines (Fig. 5). The best-fit LTE model fits very well all detected transitions, except the very optically thick lines of the main isotopologue which it underes-

⁵ See <http://spec.jpl.nasa.gov>.

Table 3. Rotational temperatures derived from population diagrams of selected (complex) organic molecules toward Sgr B2(N2).

Molecule	States ^a	T_{fit}^b (K)
CH ₃ CN	$v_8 = 1, v_8 = 2, v_4 = 1$	253 (15)
¹³ CH ₃ CN	$v = 0, v_8 = 1$	168 (13)
CH ₃ ¹³ CN	$v = 0, v_8 = 1$	165.5 (3.3)
CH ₂ DCN	$v = 0$	136 (14)
C ₂ H ₅ CN	$v = 0$	137.3 (1.6)
¹³ CH ₃ CH ₂ CN	$v = 0$	138.3 (7.5)
CH ₃ ¹³ CH ₂ CN	$v = 0$	112 (11)
CH ₃ CH ₂ ¹³ CN	$v = 0$	150 (40)
C ₂ H ₃ CN	$v = 0, v_{11} = 1, v_{15} = 1, v_{11} = 2$	199.5 (3.4)
¹³ CH ₂ CHCN	$v = 0$	255 (101)
CH ₂ ¹³ CHCN	$v = 0$	140 (31)
CH ₂ CH ¹³ CN	$v = 0$	278 (126)
H ¹³ CCCN	$v = 0, v_7 = 1$	171.1 (3.2)
HC ¹³ CCN	$v = 0, v_7 = 1$	167.7 (5.5)
HCC ¹³ CN	$v = 0, v_7 = 1$	177 (18)
CH ₃ OCHO	$v_t = 0, v_t = 1$	142.4 (4.4)

Notes. ^(a) Vibrational states that were taken into account to fit the population diagram. ^(b) The standard deviation of the fit is given in parentheses. As explained in Sect. 3, these uncertainties should be viewed with caution. They may be underestimated.

timates significantly. We ignored the lines with optical depth higher than ~ 2.5 to construct the population diagram of this species (Fig. 6), while all lines of the ¹³C isotopologues that matched the criteria defined in Sect. 3 were used for their population diagrams (Figs. 7, 8, and 9). The results of the linear fit to the population diagrams of all four isotopologues are given in Table 3. The rotational temperature is well constrained to ~ 140 K for both C₂H₅CN and ¹³CH₃CH₂CN. This value is consistent with the result of the fit for the two other isotopologues within the uncertainties. Note that the temperature derived in this way depends on the model used to make the opacity correction. With an earlier best-fit model that assumed a temperature of 170 K (instead of 150 K here), the fit to the population diagrams of both C₂H₅CN and ¹³CH₃CH₂CN yielded a temperature of ~ 150 K. This is the reason why we decided to assume a rotational temperature of 150 K for ethyl cyanide and all its isotopologues.

The median source size derived for the selected lines of C₂H₅CN is about 1.15'', but there seems to be a trend of decreasing size with increasing upper level energy, from $\sim 1.3''$ at low energy to $\sim 0.8''$ at $E_u \sim 700$ K (Fig. 10). Similar results are obtained for ¹³CH₃CH₂CN, with a median size of $\sim 1.25''$ and a hint of a decrease down to $\sim 1.0''$ at $E_u \sim 120$ K. Our model does not treat such gradients. As a compromise, we used a source size of 1.2''.

With this source size and a rotational temperature of 150 K, we obtain an excellent fit to all emission lines of the four isotopologues, except for the very optically thick lines of C₂H₅CN ($\tau_{\text{max}} \sim 60$), as mentioned above. A better fit to these lines would be obtained by increasing the temperature and/or assuming a larger source size. Increasing the size to 1.4'' turns out to be insufficient. A larger size would be inconsistent with the measured sizes. Increasing the temperature to 200 K and the size to 1.3'' yields peak temperatures of the optically thick lines similar to those observed, but the synthetic lines look too saturated compared to the observed ones, and the fit to the optically thin lines

becomes worse, lines with high upper level energies becoming overpredicted. A more complex model with non-uniform physical parameters would probably be needed to reproduce the intensity and shape of the very optically thick lines.

Using the source size, rotational temperature, linewidth, and velocity offset derived for C₂H₅CN and its ¹³C and ¹⁵N isotopologues, we looked for emission of the singly-deuterated isotopologues, CH₃CHDCN and CH₂DCH₂CN. The former is a chiral molecule because the carbon atom in the middle of the chain is linked to four different atoms or functional groups. Both isotopologues are tentatively detected toward Sgr B2(N2) with 1 and 2 line(s), respectively (Figs. 11 and 12), the latter in its out-of-plane conformation only. For the in-plane conformer of CH₂DCH₂CN, we derive an upper limit only. This upper limit is uncertain because the apparent inconsistency between the synthetic spectrum and the observed one around ~ 101190 MHz may result from a slight overestimate of the baseline, at the 3σ level (Fig.13). Due to the limited signal-to-noise ratios, the source size derived from the integrated intensity maps of the uncontaminated lines assigned to CH₃CHDCN and CH₂DCH₂CN is uncertain, varying between unresolved and $\sim 2''$. The emission looks compact in the maps. Assuming the same source size as the other isotopologues looks thus reasonable.

5.2. Deuterated methyl cyanide CH₂DCN

Methyl cyanide is clearly detected in its vibrational ground state toward Sgr B2(N2) but its transitions are very optically thick ($\tau_{\text{max}} \sim 50$) and cannot be properly fitted in the framework of our simple model (Fig. 14). Transitions from within its vibrationally excited states $v_8 = 1$ and $v_8 = 2$ are also clearly detected, with $\tau_{\text{max}} \sim 2.7$ and 0.3, respectively (Figs. 15 and 16). We also find four transitions from within $v_4 = 1$ around 91520 MHz and 109820 MHz ($\tau_{\text{max}} \sim 0.06$), but they partially suffer from blends with other species (Fig. 17). The assignment looks reasonable, but the detection should be considered as tentative.

The singly-substituted ¹³C isotopologues are very well detected, both in their vibrational ground state and in their first vibrationally excited state $v_8 = 1$ (Figs. 18, 19, 20, and 21). The fit to their population diagrams yields rotational temperatures of about 170 K (see Table 3 and Figs. 22 and 23). The analysis of the integrated intensity maps of the ¹³C isotopologues delivers a source size of $\sim 1.4''$. For the main isotopologue, it seems that the source size decreases with the vibrational energy ($\sim 1.2''$ for $v_8 = 1$ and $\sim 0.8''$ for $v_8 = 2$).

Assuming a source size of 1.4'' and a temperature of 170 K, our LTE modeling yields excellent and consistent fits to the ¹³C isotopologues (both $v = 0$ and $v_8 = 1$) and to the $v_8 = 1$ transitions of the main isotopologue. However, it was necessary to increase the column density and linewidth in order to fit the transitions of the $v_8 = 2$ and $v_4 = 1$ states. The fit to the population diagram of the main isotopologue including the three vibrationally excited states suggests a temperature of ~ 250 K (Fig. 24), which explains why our 170 K model needs higher column densities to reproduce the intensities of the $v_8 = 2$ and $v_4 = 1$ transitions. Here again, a more complex model with a non-uniform physical structure would be necessary to fit all transitions in a consistent way. However, given that our simple LTE model yields a good fit to the $v_8 = 1$ transitions of the main isotopologue and all transitions of the ¹³C ones with a single set of parameters, we consider that the derived ¹²C/¹³C column density ratios are reliable.

On the basis of the LTE model obtained above, we were able to identify emission from the doubly-substituted ¹³C isotopologue of methyl cyanide, ¹³CH₃¹³CN. One transition at

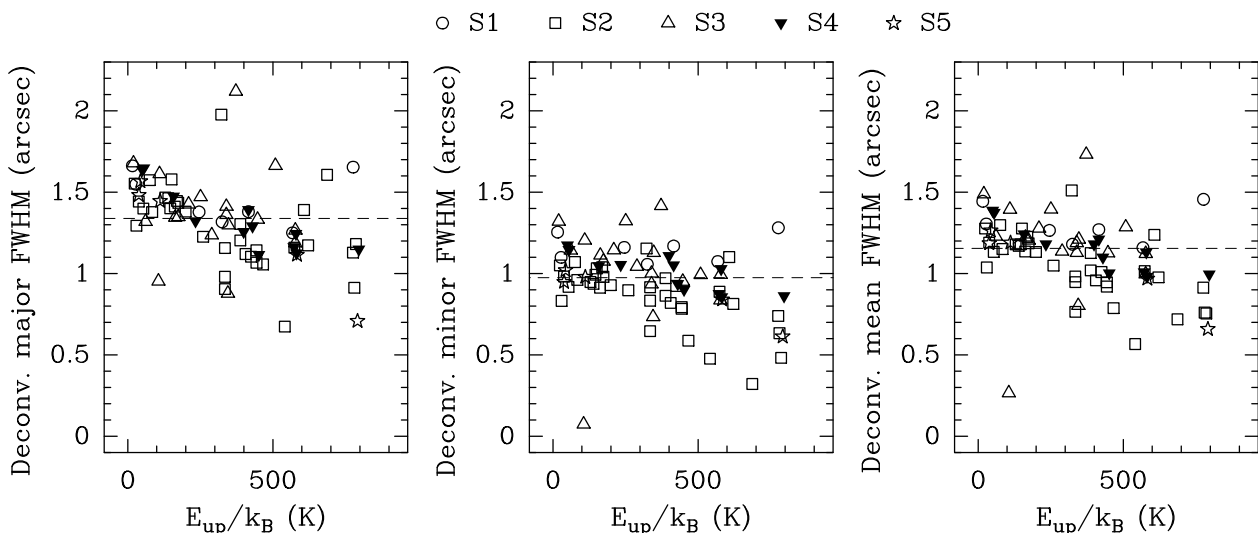


Fig. 10. Deconvolved major, minor, and mean sizes (FWHM) derived for uncontaminated C_2H_5CN transitions detected toward Sgr B2(N2), plotted as a function of upper level energy. The symbols code for the spectral setup (S1 to S5, like in Table 2). In each panel, the dashed line indicates the median value.

107108 MHz is well detected, and a group of transitions at 89270 MHz is relatively well detected (Fig. 25). Given that the column density ratio of the singly- to doubly-substituted isotopologues is very close to the ratio between the main isotopologue and the singly-substituted ones, we consider the identification of $^{13}CH_3^{13}CN$ as secure.

Our LTE modeling indicates that the ^{15}N isotopologue contributes significantly to the emission detected at 107054 MHz and 107060 MHz (Fig. 26). However, since there is no clearly detected line, we do not consider this identification as secure. The derived column density is therefore relatively uncertain and should rather be considered as an upper limit.

Finally, using the same parameters as for the other isotopologues, we obtain a secure identification of singly-deuterated methyl cyanide, CH_2DCN , with about six transitions clearly detected (Fig. 27). The rotation temperature derived from the population diagram is consistent with the assumed temperature within 2.4σ (Table 3 and Fig. 28). The source size can be measured for three of the detected transitions and is found to be consistent with the size derived from the ^{13}C isotopologues.

5.3. Deuterated cyanoacetylene DC_3N

Cyanoacetylene is detected toward Sgr B2(N2) in its vibrational ground state (Fig. 29) but also in many vibrationally excited states: $v_7 = 1$ (Fig. 30), $v_7 = 2$ (Fig. 31), $v_6 = 1$ (Fig. 32), $v_5 = 1$ and $v_7 = 3$ (Fig. 33), and $v_6 = v_7 = 1$ (Fig. 34). In addition, emission from within the following excited states is tentatively detected: $v_4 = 1$ (one detected line, Fig. 35), $v_7 = 4$ and $v_5 = v_7 = 1$ (significantly contributes to detected signal, but no line individually detected, Fig. 36)⁶, and $v_6 = 2$ (one detected line, Fig. 37).

The three singly-substituted ^{13}C isotopologues of cyanoacetylene are also clearly detected in their vibrational

ground state (Figs. 38, 39, and 40) and in $v_7 = 1$ (Figs. 41, 42, and 43). $HC^{13}CCN$ is also detected in $v_7 = 2$ (Fig. 44) while the two other isotopologues are only tentatively detected in this state (Figs. 45 and 46). $HC^{13}CCN$ and $HCC^{13}CN$ are tentatively detected in $v_6 = 1$ with one detected line each (Figs. 47 and 48). Emission of $H^{13}CCCN$ in $v_6 = 1$ significantly contributes to the detected signal, but this state cannot be unambiguously identified (Fig. 49).

Two doubly-substituted ^{13}C isotopologues of cyanoacetylene, $H^{13}C^{13}CCN$ and $HC^{13}C^{13}CN$ are tentatively detected in their vibrational ground state with one line each (Figs. 50 and 51). The third one, $H^{13}CC^{13}CN$ has no clearly detected line, but the model using the same parameters as the former two isotopologues is fully consistent with the signal detected around 105328 MHz (Fig. 52). Therefore we consider this species as tentatively detected too.

The ^{15}N isotopologue $HC_3^{15}N$ is not unambiguously detected in its vibrational ground state but, if we assume a $^{14}N/^{15}N$ isotopic ratio of 300, it contributes significantly to the detected signal at 88334 MHz and 105999 MHz and was therefore included in our model (Fig. 53). Its column density should be rather considered as an upper limit.

The fits to the integrated intensity maps suggest that the size of the emission decreases with increasing energy of the vibrational state from within which the lines are emitted. Since our model cannot account for a non-uniform physical structure, we defined two groups of vibrational states: $v = 0$ and $v_7 = 1$ were modeled with a source size of $1.3''$ while the higher excited states were modeled assuming $0.9''$.

The fits to the population diagrams of the singly-substituted ^{13}C isotopologues including both $v = 0$ and $v_7 = 1$ yield rotational temperatures of ~ 170 – 180 K (Table 3, Figs. 54, 55, and 56). With a temperature of 170 K and a source size of $1.3''$, the emission of all isotopologues reported above is well fitted up to $v_7 = 1$, except for the vibrational ground state of HC_3N : its transitions are very optically thick ($\tau_{\max} \sim 30$) and cannot be reproduced with our simple model. For the vibrationally excited states of the main and singly-substituted ^{13}C isotopologues above $v_7 = 1$, we assume a source size of $0.9''$ and obtain a very good fit to the observed spectra with a temperature of 200 K

⁶ The current model is somewhat inconsistent with the observed spectrum at 92129 MHz (blend of $v_7 = 4$ $10_{-2} - 9_2$ and $10_4 - 9_4$) and 100431 MHz ($v_5 = v_7 = 1$ $l = 0^- - 11_0 - 10_0$) but this is most likely due to resonant interactions between $v_7 = 4$ and $v_5 = v_7 = 1$ which are not well accounted for in the spectroscopic predictions. The frequencies of these transitions may well be off by a few MHz (see CDMS documentation and Sect. 4.4.33 of Belloche et al. 2013)

and a unique column density (divided by 20 for the ^{13}C isotopologues), 1.5 times higher than for the model of the lower states.

Using the parameters derived above for the vibrational ground state, we looked for emission of deuterated cyanoacetylene DC_3N . The molecule seems to contribute at a level of $\sim 70\%$ to the signal detected at 101315 MHz (Fig. 57). The rest of the emission comes from a transition of CH_2CO in its vibrationally excited state $v_9 = 1$. The detection of DC_3N is only tentative, and its column density should be rather considered as an upper limit.

5.4. Deuterated methanol CH_2DOH

Methanol and its ^{13}C and ^{18}O isotopologues are well detected toward Sgr B2(N2). The detected lines and detailed modeling of these species is presented in a companion paper (Müller et al. 2015c). We report in Table 4 the parameters derived in that paper for the main isotopologue based on the analysis of all isotopologues.

Assuming the same source size and rotational temperature, we obtain a tentative detection of CH_2DOH , with two lines detected at 91587 MHz ($4_{1,3} e_0 - 4_{0,4} e_0$) and 99672 MHz ($6_{1,5} e_0 - 6_{0,6} e_0$), two lines tentatively detected at 85600 MHz ($6_{2,4} e_1 - 6_{1,6} o_1$) and 94563 MHz ($1_{1,0} o_1 - 1_{0,1} o_1$), and a few other lines contributing significantly to the detected signal (Fig. 58). The line appearing at 91589 MHz in the full synthetic model with no counterpart in the observed spectrum corresponds to two transitions of acetone ($23_{18,6} - 23_{17,7}$ of the EE state and $23_{18,6} - 23_{17,7}$ of the AE state). While acetone is unambiguously detected in our ALMA spectrum of Sgr B2(N2), a significant number of predicted lines of acetone do not match the observed spectrum. The spectroscopic predictions are not accurate enough for this set of problematic lines, the line at 91589 MHz being one of those. The ALMA spectrum suggests that the true frequency could be 91592 MHz for this acetone line. The source size derived from the maps of the two detected CH_2DOH lines is uncertain but the emission looks compact in the integrated intensity maps and is consistent with the source size assumed for the modeling.

5.5. Upper limits

5.5.1. Deuterated methanol CH_3OD

CH_3OD is not unambiguously detected toward Sgr B2(N2). It may significantly contribute to the emission detected at 90743 MHz (blend of $10_{1,1} - 9_{2,1}$ and $2_{1,0} - 1_{1,0}$), 110951 MHz ($4_{1,0} - 4_{0,0}$), 111846 MHz ($5_{1,0} - 5_{0,0}$), and 113352 MHz ($6_{1,0} - 6_{0,0}$), but there is no clearly detected line (Fig. 59). Using the same parameters as for methanol (Sect. 5.4), we derive a column density upper limit a factor 1.8 times lower than the column density tentatively derived for CH_2DOH (Table 4). This upper limit corresponds to the synthetic spectrum shown in red in Fig. 59.

5.5.2. Deuterated vinyl cyanide CHDCHCN and CH_2CDCN

Many lines of vinyl cyanide are detected in its ground state and vibrationally excited states $v_{11} = 1$, $v_{15} = 1$, and $v_{11} = 2$ (Figs. 60, 61, 62, 63). The sizes derived from the corresponding integrated intensity maps tend to decrease with increasing energy, from $\sim 1.2''$ for $E_{\text{up}} < 100$ K to $\sim 0.8''$ for higher-energy transitions. As a compromise we adopt a source size of $1.1''$. With this source size, the analysis of the population diagram yields a temperature of ~ 200 K (Table 3 and Fig. 64). Transitions from within even higher vibrationally excited states

are also detected toward Sgr B2(N2), but we do not report about these states in this work.

Transitions of all three singly-substituted ^{13}C isotopologues of vinyl cyanide are also clearly detected (Figs. 65, 66, and 67; see also Müller et al. 2008 for a previous single-dish detection). Only a few lines are sufficiently free of contamination to allow for a size measurement in the corresponding integrated intensity maps. The outcome is more uncertain than for the main isotopologue, but is consistent with the source size adopted above. Due to the smaller number of detected lines, the population diagrams have a higher dispersion than for the main isotopologue and the rotational temperature is less well constrained but the fits to all three diagrams are consistent with a temperature of about 200 K (Figs. 68, 69, and 70).

As a result of this analysis, we adopt a source size of $1.1''$ and a temperature of 200 K for vinyl cyanide and its isotopologues. With these parameters, we do not detect the ^{15}N isotopologue. We also looked for the singly-deuterated species *cis*- CHDCHCN , *trans*- CHDCHCN , and CH_2CDCN , but did not detect them. Column density upper limits are reported in Table 4.

5.5.3. Deuterated ethanol $\text{CH}_3\text{CH}_2\text{OD}$, CH_3CHDOH , and $\text{CH}_2\text{DCH}_2\text{OH}$

Ethanol and its ^{13}C isotopologues are well detected toward Sgr B2(N2). The detected lines and detailed modeling of these species is presented in a companion paper (Müller et al. 2015c). We report in Table 4 the parameters derived in that paper for the main isotopologue based on the analysis of all isotopologues.

Assuming the same LTE parameters as for the main isotopologue, we searched for all singly deuterated isotopologues of ethanol. None is detected. Upper limits to their column densities are reported in Table 4.

5.5.4. Deuterated methyl formate CH_2DOCHO

Methyl formate is clearly seen toward Sgr B2(N2), with dozens of transitions detected in both its ground and first torsional states (Figs. 71 and 72). We derive a median source size of $1.5''$ from fits to the integrated intensity maps of its numerous uncontaminated lines. The formal fit to its population diagram including both states yields a rotational temperature of ~ 140 K (Fig. 73 and Table 3). We used a temperature of 150 K in our model, which fits very well the ALMA spectrum, apart from a few discrepancies that we describe now. The reason why the synthetic spectrum of the ground state poorly fits the ALMA spectrum at 100080 MHz is unclear. It may be due to the nearby HC_3N 11–10 transition at 100076 MHz that is probably affected by self-absorption and/or spatial filtering and is by far overestimated by our simple LTE model. The discrepancy around 110226 MHz is due to contamination by diffuse cloud absorption in ^{13}CO 1–0 that is not yet included in our full model. Similar contamination by $c\text{-C}_3\text{H}_2$ absorption features not yet implemented in our full model likely explains the small discrepancies for the $v_t = 1$ transitions around 85370 MHz.

Assuming the same LTE parameters as for the main isotopologue, we searched for the in-plane and out-of-plane conformers of CH_2DOCHO toward Sgr B2(N2) but none of them is detected. Upper limits to their individual column densities are reported in Table 4.

Table 5. Deuterium fractionation of selected (complex) organic molecules toward Sgr B2(N2) compared to predictions of astrochemical models.

Molecule	Status ^a	[XD]/[XH]		
		N2 ^b %	T14 ^c %	A12 ^d %
CH ₂ DCN	d	0.38	3.6 – 0.15	2.3 – 6.3
CH ₂ DCH ₂ CN (oop)	t	0.05	—	—
CH ₂ DCH ₂ CN (ip)	n	< 0.024	—	—
CH ₃ CHDCN	t	0.05	—	—
<i>cis</i> -CHDCHCN	n	< 0.8	—	—
<i>trans</i> -CHDCHCN	n	< 0.8	—	—
CH ₂ CDCN	n	< 0.5	—	—
DC ₃ N	t	0.09	—	5.4 – 1.1
CH ₂ DOH	t	0.12	5.5 – 0.51	2.4 – 2.4 ^e
CH ₃ OD	n	< 0.07	3.5 – 0.3	— ^e
CH ₃ CH ₂ OD	n	< 1.5	—	—
CH ₃ CHDOH	n	< 1.5	—	—
CH ₂ DCH ₂ OH (oop)	n	< 1.5	—	—
CH ₂ DCH ₂ OH (ip)	n	< 1.0	—	—
CH ₂ DOCHO (oop)	n	< 2.0	14–0.43 ^f	—
CH ₂ DOCHO (ip)	n	< 0.6	7 – 0.22 ^f	—

Notes. ‘oop’ and ‘ip’ describe the position of the deuterium and stand for ‘out of plane’ and ‘in plane’, respectively. ^(a) d: detection, t: tentative detection, n: non-detection. ^(b) Deuterium fractionation measured toward Sgr B2(N2). ^(c) Deuterium fractionation predicted by the model of Taquet et al. (2014) in the hot corino at the beginning and end of the Class 0 phase. ^(d) Deuterium fractionation predicted by the model of Aikawa et al. (2012) in the hot corino at the beginning and end of the Class 0 phase. ^(e) The model of Aikawa et al. (2012) was not designed to predict the abundance ratios of deuterated isomers: it assumes statistical branching ratios. ^(f) The model of Taquet et al. (2014) does not distinguish between the in-plane and out-of-plane conformers. The values listed here assume a statistical distribution (2:1).

6. Discussion

6.1. Comparison to other observations

The levels of deuterium fractionation derived in Sect. 5 for (complex) organic molecules toward Sgr B2(N2) are summarized in Table 5 and displayed in Fig. 74.

6.1.1. Deuterated methyl cyanide

The detection of CH₂DCN toward Sgr B2(N2) is the most secure among the deuterated species reported here (Sect. 5.2 and Fig. 27). On the basis of the LTE modeling of methyl cyanide and its various isotopologues, we derive a deuterium fractionation of 0.4% for this molecule. This is a factor 2.6 lower than the fractionation reported by Gerin et al. (1992) toward Orion KL (1%). Along with this first interstellar detection, these authors also reported a tentative detection toward the hot core G34.26+0.15 that, if true, would indicate a similar level of deuterium fractionation as toward Orion KL. The difference with the level measured in Sgr B2(N2) is probably not significant because the Orion KL and G34.26+0.15 values may suffer, as mentioned by these authors, from a lack of knowledge of the source size and opacity of the lines of the main isotopologue.

A detection of deuterated methyl cyanide toward the Class 0 (low-mass) protostar IRAS 16293–2422 was also reported in Taquet et al. (2014) based on an unpublished analysis. They

quote a deuterium fractionation of 1.3%, a factor 3.4 higher than the one obtained for Sgr B2(N2).

6.1.2. Deuterated ethyl cyanide

Both deuterated isotopologues of ethyl cyanide are tentatively detected toward Sgr B2(N2) (Sect. 5.1 and Figs. 11 and 12). We derive a deuterium fractionation of $\sim 0.05\%$ for both CH₂DCH₂CN (in its out-of-plane conformation) and the chiral molecule CH₃CHDCN. The upper limit obtained for the in-plane conformer of CH₂DCH₂CN (Fig. 13) is still consistent with the expectation that it should be twice less abundant than the out-of-plane one. If we assume such a ratio, then the total deuterium fractionation for CH₂DCH₂CN would be $\sim 0.075\%$, a factor 1.5 times higher than for CH₃CHDCN. This would be consistent with the statistical expectation because the methyl group at the end of the carbon chain has three equivalent hydrogen atoms while the middle-chain one has only two.

The deuterium fractionation derived for ethyl cyanide toward Sgr B2(N2) is nearly one order of magnitude lower than for methyl cyanide (0.4%), but similar within a factor two to methanol (0.12%) and cyanoacetylene (0.09%).

Margulès et al. (2009) reported a detection of the ¹⁵N isotopologue of ethyl cyanide toward Orion KL but obtained only an upper limit for CH₂DCH₂CN. They derived a column density ratio [CH₂DCH₂CN (oop)]/[C₂H₅C¹⁵N] < 0.33, which translates into [CH₂DCH₂CN (oop)]/[C₂H₅CN] < 0.2% using the ¹⁴N/¹⁵N isotopic ratio of 148 ± 74 derived by Daly et al. (2013). We note that Daly et al. (2013) claimed tentative detections of both deuterated isotopologues of ethyl cyanide with a deuterium fractionation of 2%, based on the same survey of Orion KL. No detected transitions are shown in that study, though, and their Table 3 actually reports upper limits for the deuterated species. Given the lower deuterium fractionation obtained by Gerin et al. (1992) for methyl cyanide toward Orion KL (1%) and the order of magnitude difference in deuterium fractionation between methyl cyanide and ethyl cyanide obtained here toward Sgr B2(N2), a deuterium fractionation of 2% for ethyl cyanide in Orion KL sounds unlikely and questions the tentative detection of Daly et al. (2013).

6.1.3. Deuterated methanol

CH₂DOH is tentatively detected toward Sgr B2(N2) (Sect. 5.4 and Fig. 58). The deuterium fractionation we derive for this isotopologue is 0.12%, a factor ~ 3 lower than the value we obtain for methyl cyanide, the deuterated species of which is securely identified in our ALMA spectrum of Sgr B2(N2) (Sect. 6.1.1). Therefore, even if the difference in deuterium fractionation between methanol and methyl cyanide is a priori surprising, the fact that it is lower for the former gives us more confidence in the detection of CH₂DOH. The deuterium fractionation derived for CH₂DOH is a factor five lower than toward the Compact Ridge in Orion KL (0.58%, Neill et al. 2013), about one order of magnitude lower than toward the high-mass protostellar objects surveyed by Fontani et al. (2015) and the intermediate-mass protostar NGC 7129 FIRS 2 (2%, Fuente et al. 2014), and more than two orders of magnitude lower than toward Class 0 protostars which have values between 19% and 33% (Parise et al. 2006)⁷.

⁷ There was an issue with the spectroscopic predictions used in the early studies reporting CH₂DOH column densities (B. Parise, priv. comm.). We compared the $S\mu^2$ values listed in Table 1 of Parise et al. (2002), which were also used in Parise et al. (2006), with the current

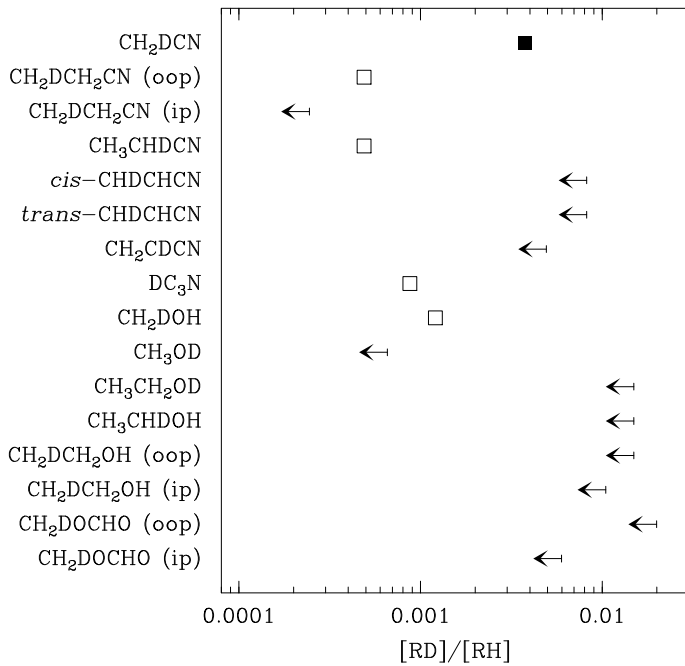


Fig. 74. Deuterium fractionation of (complex) organic molecules toward Sgr B2(N2). Secure detections are indicated with a filled square, tentative detections with an empty square, and upper limits with an arrow pointing to the left. 'oop' and 'ip' describe the position of the deuterium and stand for 'out of plane' and 'in plane', respectively.

Evidence for the presence of CH₃OD is too tenuous in our ALMA spectrum of Sgr B2(N2) to claim a detection, even a tentative one (Sect. 5.5.1). Still, we cannot completely exclude that CH₃OD is present at the level indicated by our upper limit. The synthetic spectrum shown in Fig. 59 indicates that a large fraction (> 50%) of the flux density detected at 90744, 99964, 110951, and 113352 MHz may well be emitted by this molecule. If this is true, the deuterium fractionation of methanol would then be ~ 0.07% for CH₃OD. This would be nearly one order of magnitude lower than toward the Compact Ridge in Orion KL (0.5%, Neill et al. 2013) and about 50 times lower than toward Class 0 protostars (1.6%–4.7%, Parise et al. 2006).

A detection of CH₃OD toward Sgr B2 was reported by Gottlieb et al. (1979) with the 36 foot radio telescope of the National Radio Astronomy Observatory at Kitt Peak (*HPBW* ~ 74"). They detected a line at the frequency expected for the pair of partially blended transitions 2₋₁–1₋₁ E (90703.6 MHz, E_u/k_B = 11.3 K) and 2₀–1₀ A (90705.8 MHz, E_u/k_B = 6.5 K), but they did not detect the nearby 2₁–1₁ E transition (90743.5 MHz, E_u/k_B = 15.6 K) that is in fact expected to be partially blended with the 10₁–9₂ A transition (90741.7 MHz, E_u/k_B = 124 K). The former two transitions are blended with deep HNC absorption features produced by diffuse clouds along the line of sight in our ALMA spectrum of Sgr B2(N2). This prevents their detection in our spectrum (see Fig. 59). Our LTE model shows that, for a temperature of 160 K, the latter two transitions are expected to be as strong as the former two. We conclude from this that either the assignment of the 90704 MHz line to CH₃OD in the Kitt Peak spectrum was not correct, or the line reported by Gottlieb et al. (1979) traces low-excitation emission

of CH₃OD. Given that the line detected in emission in the Kitt Peak spectrum dominates over the absorption features, opposite to what is seen in the ALMA spectrum, this emission line, if real, must come from a region more extended than the Sgr B2 continuum emission that is absorbed by the diffuse clouds along the line of sight. Such an extended emission would be filtered out in our ALMA spectrum.

Gottlieb et al. (1979) derived a ratio [CH₃OD]/[¹³CH₃OH] ~ 0.18 for Sgr B2. This translates into [CH₃OD]/[CH₃OH] ~ 0.7%, assuming a ¹²C/¹³C isotopic ratio of 25 as derived for methanol toward Sgr B2(N2) in the companion paper Müller et al. (2015c). This is an order of magnitude higher than our upper limit of 0.07% derived in Sect. 5.4. This discrepancy seriously questions the detection of CH₃OD reported by Gottlieb et al. (1979) toward Sgr B2, unless deuteration of methanol is more efficient by one order of magnitude on large scales in the Sgr B2 cloud compared to the embedded hot cores. We note that Comito et al. (2003) derived an abundance ratio [HDO]/[H₂O] ~ 0.06% toward the Sgr B2 hot cores and their $T < 100$ K envelope, and even lower values of ~ 0.013% and ~ 0.02% (uncertain within a factor two) were obtained for [DCN]/[HCN] and [DCO⁺]/[HCO⁺] in the molecular ridge close to Sgr B2(M) (Jacq et al. 1999). Deuterium fractionation thus does not appear to be generally more efficient on larger scales in Sgr B2, which again questions the detection of CH₃OD reported by Gottlieb et al. (1979).

6.1.4. Deuterated cyanoacetylene

The detection of DC₃N reported toward Sgr B2(N2) is only tentative (Sect. 5.3 and Fig. 57). We obtain a deuterium fractionation of 0.09%, similar to the values obtained for methanol and ethyl cyanide. DC₃N was first detected toward TMC 1 with a deuterium fractionation of 2–8% (Langer et al. 1980), revised to a lower value of 1.5% by Turner (2001). High values were reported with single dish telescopes for a number of other cold dense cores (5%–10%, Howe et al. 1994) as well as for a protostar in a stage of "Warm Carbon-Chain Chemistry" (~ 3%, Sakai et al. 2009). A tentative detection toward the Compact Ridge and the Hot Core of Orion KL was recently reported with a deuterium fractionation of 1.5% ± 0.9% (Esplugues et al. 2013). A tentative detection was also recently reported toward the high-mass protostar NGC 2264 CMM3 (1.8% ± 1.5%, Watanabe et al. 2015). The deuterium fractionation of cyanoacetylene tentatively derived toward Sgr B2(N2) is thus at least one order of magnitude lower than in Orion and NGC 2264 CMM3 (if confirmed) and even two orders of magnitude lower than in cold dense gas.

6.1.5. Deuterated vinyl cyanide

The column density upper limits reported in Sect. 5.5.2 yield deuterium fractionations < 0.8%, < 0.8%, and < 0.5% for *cis*-CHDCHCN, *trans*-CHDCHCN, and CH₂CDCN, respectively. We are not aware of any reliable detection of deuterated vinyl cyanide in the interstellar medium.

6.1.6. Deuterated ethanol

The column density upper limits reported in Sect. 5.5.3 yield deuterium fractionations < 1.5%, < 1.5%, < 1.5%, and < 1.0% for CH₃CH₂OD, CH₃CHDOH, and the out-of-plane and in-plane conformers of CH₂DCH₂OH, respectively. The latter

JPL catalog. The new values of the selected transitions are a factor 2.1 ± 0.4 times higher than the old ones on average. The partition function is the same in both cases. As a result, the column densities reported for CH₂DOH in both articles were overestimated by a factor of ~ 2.

two translate into a total deuterium fractionation $< 2.5\%$ for $\text{CH}_2\text{DCH}_2\text{OH}$. These upper limits are about one order of magnitude higher than the deuterium fractionation measured for methanol (Sect. 6.1.3). They are thus not very constraining. We are not aware of any detection of deuterated ethanol in the interstellar medium.

6.1.7. Deuterated methyl formate

The column density upper limits reported in Sect. 5.5.4 yield deuterium fractionations $< 2.0\%$ and $< 0.6\%$ for the out-of-plane and in-plane conformers of CH_2DOCHO , respectively. This implies an upper limit of 2.6% for the molecule as a whole, or even 1.8% if we assume a statistical distribution and use the most stringent constraint provided by the in-plane conformer. A detection of CH_2DOCHO toward the Compact Ridge of Orion KL was reported by Coudert et al. (2013). They derived a deuterium fractionation of $4\% \pm 2\%$. Fuente et al. (2014) reported a tentative detection of CH_3OCDO and both conformers of CH_2DOCHO at a deuteration level of 6% toward the intermediate-mass protostar NGC 7129 FIRS 2, but the value is uncertain due to blends with other species. Our upper limit for Sgr B2(N2) lies a factor two to three below these values.

6.2. Comparison to predictions of chemical models

We compare the deuterium fractionation derived for complex organic molecules toward Sgr B2(N2) to predictions of astrochemical models that investigated the deuteration of such species. The case of deuterated methanol is more specifically discussed in Sect. 6.3 below. The two models considered here follow the evolution of molecular abundances in a collapsing dense core that is heated up by the central protostar once it is formed (Taquet et al. 2012, 2014; Aikawa et al. 2012). These models were designed for Class 0 protostars, i.e. low-mass objects, so they are not optimum for a comparison to Sgr B2(N2). However they are the only models dealing with deuterated complex molecules that are presently available in the literature. No model following the deuteration of complex molecules in a high-mass star forming region like Sgr B2(N2) has been published so far. As we will see in Sect. 6.4 below, there is a clear need for that.

Both models couple the chemistry in the gas-phase and on the dust grains. The layering of the icy grain mantles and the presence of *ortho*- and *para*- H_2 are taken into account in Taquet et al. (2014, hereafter T14) but not in Aikawa et al. (2012, hereafter A12). Model A12 uses a one-dimensional radiation hydrodynamic model of gravitational collapse, preceded by a hydrostatic phase that lasts for one million years. Model T14 relies on a parametric description of the quasi-static formation of the dense core followed by a free-fall collapse phase during which the protostar quickly appears after one free-fall time. In both models, the gas and dust temperatures are kept equal. In model T14, the temperature decreases from 17 K at the external radius down to about 7 K in the inner parts of the core at the end of the prestellar phase. In model A12, the external temperature is about 10 K and drops to about 5 K at the end of the prestellar phase. In both models, the temperature increases once the protostar appears.

Table 5 lists the deuterium fractionations predicted by both astrochemical models in the hot corino central region at the beginning and end of the Class 0 phase. Nearly all predicted values are at least a factor four higher than the ones obtained toward Sgr B2(N2). The only exception is the deuterium fractionation

of CH_3CN : it is predicted to decline during the Class 0 phase in model T14 and the measured value lies close to (a factor 2.5 above) the lower end of the predicted range. The decrease of the deuterium fractionation of complex organic molecules during the hot corino phase in model T14 is due to the collapse of the envelope: as time goes by, the gas passing through the hot corino is originating from shells that were initially at larger radii, i.e. lower densities, and underwent lower deuteration, imposed by a lower level of CO depletion and a higher [*ortho*- H_2]/[*para*- H_2] ratio. However, model A12 predicts an increase of the deuterium fractionation of CH_3CN with time during the protostellar phase, with values a factor > 5 higher than measured toward Sgr B2(N2), i.e. in worse agreement with the observations than model T14. The fact that model A12 does not predict a decrease of the deuteration of complex organic molecules with time may be due to the model not taking the multi-layered structure of ice mantles into account.

The deuterium fractionation predicted by model T14 for methanol is 1.5–3.4 times higher than the one of methyl cyanide while model A12 finds the opposite, with methyl cyanide becoming 2.6 times more deuterated than methanol at the end of the Class 0 phase. The ratio measured toward Sgr B2(N2) is more in agreement with the latter model.

Model T14 predicts higher deuterium fractionations for methyl formate and dimethyl ether because these more complex molecules are formed from the photodissociation of highly deuterated formaldehyde and methanol at the surface of dust grains when they start to warm up. Both molecules are predicted to be even more deuterated than methanol. The upper limit we derive for the deuteration of methyl formate – an order of magnitude higher than that of methanol – is not stringent enough to test this prediction. The model predictions for these more complex molecules could let us expect a similar behaviour for ethyl cyanide compared to methyl cyanide. The tentative deuteration level we measured for ethyl cyanide is, however, not consistent with this naive expectation: ethyl cyanide is (at least) about a factor five less deuterated than methyl cyanide in Sgr B2(N2).

Unlike all other complex organic molecules, the formation of methyl cyanide is dominated by gas phase processes in our own models (e.g., Garrod et al. 2008; Garrod 2013). This occurs via the reaction $\text{CH}_3^+ + \text{HCN} \rightarrow \text{CH}_3\text{CNH}^+$, followed by dissociative recombination. In these models, the CH_3^+ ion is formed via $\text{H}_3^+ + \text{CH}_3\text{OH} \rightarrow \text{CH}_3^+ + \text{H}_2\text{O} + \text{H}_2$ and similar reactions of methanol with He^+ and C^+ . If equivalent gas phase reactions dominate the formation of deuterated methyl cyanide also, then the apparent discrepancy between the degrees of deuteration of methyl cyanide and ethyl cyanide may come from their different formation pathways, the former in the gas phase but the latter on the surface of dust grains. Numerical simulations should be performed to test this hypothesis.

The rotational temperature and source size derived for vinyl cyanide toward Sgr B2(N2) seem to indicate an origin in a somewhat warmer and more compact region than for ethyl cyanide. This is a priori consistent with the early model of Caselli et al. (1993) where the gas-phase abundance of vinyl cyanide is predicted to increase with time in the hot core where it is formed via protonation of ethyl cyanide followed by dissociative recombination. However, this channel has not been measured in the laboratory nor properly calculated. It is thus not clear whether this path dominates the formation of vinyl cyanide. If it does, we might expect a similar deuterium fractionation as for ethyl cyanide, but this is a simplistic assumption. The upper limit we derive for the deuteration of vinyl cyanide toward Sgr B2(N2) – more than one order of magnitude higher than the deuteration

measured for ethyl cyanide – is not low enough to test this hypothesis.

Finally, model A12 predicts a decrease of the deuterium fractionation of cyanoacetylene with time, but the value at the end of the Class 0 phase is still more than one order of magnitude higher than the one tentatively derived toward Sgr B2(N2).

6.3. The $[\text{CH}_2\text{DOH}]/[\text{CH}_3\text{OD}]$ abundance ratio

If the deuteration of methanol were purely statistical, then one would expect CH_2DOH to be three times more abundant than CH_3OD because the methyl group contains three equivalent hydrogen atoms while the hydroxyl group has only one. Early chemical models producing methanol (and its deuterated species) on the surface of dust grains predicted such a value (Charnley et al. 1997). However various chemical processes have been shown or suggested to lead potentially to different values. Osamura et al. (2004) found theoretically that it is difficult to exchange protons and deuterons between the methyl and hydroxyl parts of methanol in the gas phase. Therefore, CH_2DOH and CH_3OD are distinct species that can have different chemical timescales. In particular, protonation of methanol in the gas phase (after sublimation) followed by dissociative recombination is thought to lead to a more rapid destruction of CH_3OD compared to CH_2DOH (Charnley et al. 1997). This process would increase the $[\text{CH}_2\text{DOH}]/[\text{CH}_3\text{OD}]$ ratio after sublimation of methanol from the grain ices, on a timescale of 10^5 yr for a temperature of 50 K and an H_2 density of 10^6 cm^{-3} (Osamura et al. 2004). On the contrary, at high temperature (100 K), the gas phase model of Osamura et al. (2004) leads to a decrease of the $[\text{CH}_2\text{DOH}]/[\text{CH}_3\text{OD}]$ ratio because the release of water and its deuterated isotopologue into the gas phase opens a new channel for the production of CH_3OD via H_2DO^+ . However this model assumes a high initial $[\text{HDO}]/[\text{H}_2\text{O}]$ ratio of 0.1. The same study showed that, with an initial ratio of 0.01, $[\text{CH}_2\text{DOH}]/[\text{CH}_3\text{OD}]$ remains roughly constant.

A preferential decrease of the abundance of CH_3OD could also occur on the grains before desorption because hydrogenation of CH_3OD by D–H exchange with water was experimentally shown to occur (above 120 K) while no equivalent process exists for CH_2DOH (Ratajczak et al. 2009). Nagaoka et al. (2005) showed experimentally that the formation of deuterated methanol in interstellar ice analogs proceeds via H–D substitution of methanol with atomic D rather than successive addition of H and D on CO. The formation of CH_3OD was not found to occur during this process, which Nagaoka et al. justify by invoking the higher barrier of H abstraction from a hydroxyl group compared to the H abstraction from a methyl group. Further constraints on the H/D addition/abstraction reactions on formaldehyde and methanol were obtained by Hidaka et al. (2009). Gas-grain coupled astrochemical models incorporating these new substitution and abstraction reactions on the grain surfaces indeed predict that an enhancement of the $[\text{CH}_2\text{DOH}]/[\text{CH}_3\text{OD}]$ ratio beyond the statistical value can be reached at low temperature on a timescale depending on the density ($> 2 \times 10^4$ yr for a density of $\sim 5 \times 10^6 \text{ cm}^{-3}$, Taquet et al. 2012). However, at earlier times and/or lower densities, the $[\text{CH}_2\text{DOH}]/[\text{CH}_3\text{OD}]$ ratio is predicted to have a low value of ~ 1.4 . In a more recent version of this model that includes the spin of H_2 in the chemical network and follows the dynamical evolution and warming-up of a collapsing envelope, the $[\text{CH}_2\text{DOH}]/[\text{CH}_3\text{OD}]$ ratio in the gas phase after sublimation is predicted to be ~ 1.5 (Taquet et al. 2014).

Observationally, CH_3OD is found to be underabundant in the vicinity of low-mass protostars compared to the statistical expectation, with typical $[\text{CH}_2\text{DOH}]/[\text{CH}_3\text{OD}]$ ratios in the range 7–13 (Parise et al. 2006, see footnote 7). Similar high ratios (6 and 13) were reported for two intermediate-mass protostars (Ratajczak et al. 2011)⁸. However, this ratio was found to be close to unity in Orion KL: Jacq et al. (1993) reported a ratio of 1.1–1.5 on the basis of selected transitions observed with the IRAM 30 m telescope; Peng et al. (2012) obtained a ratio of 0.7 ± 0.3 in the central region based on a few transitions mapped at high-angular resolution with ALMA⁹; Neill et al. (2013) derived a ratio of 1.2 ± 0.3 toward the Compact Ridge based on the analysis of a complete line survey performed with *Herschel*. The upper limit of 0.6 obtained toward W3(H₂O) (Ratajczak et al. 2011, see footnote 8) adds another piece of evidence suggesting that the $[\text{CH}_2\text{DOH}]/[\text{CH}_3\text{OD}]$ ratio is significantly lower than the statistical value in high mass star forming regions.

Our analysis of the ALMA spectrum of Sgr B2(N2) leads to $[\text{CH}_2\text{DOH}]/[\text{CH}_3\text{OD}] > 1.8$. This lower limit is consistent with the ratio derived for Orion KL by Neill et al. (2013) within the uncertainties (2σ). If the actual value in Sgr B2(N2) is close to this lower limit, then it would be a further indication that this ratio is indeed lower than the statistical value in the hot portions of high-mass star forming regions, also in the Galactic Center region. However, taken at face value, our lower limit does not exclude a $[\text{CH}_2\text{DOH}]/[\text{CH}_3\text{OD}]$ ratio in Sgr B2(N2) closer to (or even higher than) the statistical value.

The low $[\text{CH}_2\text{DOH}]/[\text{CH}_3\text{OD}]$ ratio found in Orion KL and the lower limit obtained for Sgr B2(N2) are consistent with the value predicted by model T14. In this model, the ratio lies below the statistical value because of the abstraction reactions included in the chemical network following the experiments of Hidaka et al. (2009). These reactions occur only on the methyl group of methanol, and thus reduce the $[\text{CH}_2\text{DOH}]/[\text{CH}_3\text{OD}]$ ratio.

6.4. Deuterium in the Galactic Center region

With the only exception of methyl cyanide, the levels of deuterium fractionation derived for complex organic molecules in the Sgr B2(N2) hot core are all at least a factor four lower than those predicted by current gas-grain chemical models. Since deuteration is sensitive to temperature – a higher temperature implies a lower CO depletion and a higher ortho/para ratio of H_2 , both limiting the formation of H_2D^+ – the overall lower deuteration measured in Sgr B2(N2) may result from the somewhat higher temperatures measured in the Galactic Center region: gas kinetic temperatures of 30–50 K were reported in dense clumps interferometrically traced with ammonia (Ott et al. 2014) and dust temperatures derived from infrared measurements with the *Herschel* Space Observatory lie in the range 20–28 K toward Sgr B2 (Guzmán et al., submitted)¹⁰. The two numerical studies to which we compared our results were focused on (low-mass)

⁸ We have divided the ratios by 1.5 because the CH_2DOH column densities reported by Ratajczak et al. (2011) are affected by the same issue as described in footnote 7. We use the ratios reported by the authors based on the transition $3_{03}-2_{02}$ E0 that has a $S\mu^2$ value in their Table A.1 1.5 times lower than in the current JPL catalog.

⁹ Neill et al. (2013) pointed out that the use of more recent spectroscopic predictions for CH_2DOH would lead to a higher ratio of approximately 1.

¹⁰ We note, however, that high density material with lower dust temperatures may exist and be masked by warmer, outer layers traced with *Herschel*.

hot corinos that are embedded in colder regions: models T14 and A12 assume a dust temperature in the external layers of the protostellar envelope of 17 K and 10 K, respectively, and the temperature in the inner layers drops to 7 K and 5 K, respectively, just before the formation of the protostar. Changing the dust temperature has a significant impact on the deuteration in model T14: for instance, the degree of deuterium fractionation of methanol (CH_2DOH) in the ices at the end of the prestellar phase was found to be reduced by a factor 2.8 when the external temperature is set to 20 K instead of 17 K (Taquet et al. 2014). Dedicated numerical simulations are thus needed to evaluate the effect of the dust temperature in the prestellar phase on the deuterium composition of hot cores in the Galactic Center region.

Another explanation for the low deuteration level of complex organic molecules in Sgr B2(N2) could be the abundance of deuterium itself in the Galactic Center region. Several studies (Jacq et al. 1990, 1999; Lubowich et al. 2000; Polehampton et al. 2002) suggested that deuterium may be up to ~ 10 times less abundant in the Galactic Center region than in the local interstellar medium, due to stellar processing. The levels of COM deuteration found in Sgr B2(N2) are indeed systematically lower (by a factor of a few up to a factor ~ 10) than those reported in the Orion-KL Hot Core or Compact Ridge. While a chemical or evolutionary origin for this difference cannot be excluded without further modeling, the low deuteration level of complex organic molecules in Sgr B2(N2) tends to support the idea that deuterium is less abundant in the Galactic Center region by maybe up to a factor ten.

7. Conclusions

We searched for deuterated complex organic molecules in a complete 3 mm interferometric line survey performed toward the hot core Sgr B2(N2) with ALMA. We report the secure detection of CH_2DCN and tentative detections of CH_2DOH , $\text{CH}_2\text{DCH}_2\text{CN}$ in its out-of-plane conformation, the chiral molecule CH_3CHDCN , and DC_3N . We also derive column density upper limits for CH_3OD , $\text{CH}_2\text{DCH}_2\text{CN}$ in its in-plane conformation, the three deuterated isotopologues of vinyl cyanide, the four deuterated species of ethanol, and CH_2DOCHO in its in-plane and out-of-plane conformations. The detections are characterized by compact emission consistent with a hot-core origin. We obtain a deuterium fractionation level of 0.4% for CH_2DCN and values between 0.05% and 0.12% for the other (tentatively detected) species. Stringent upper limits are derived for the in-plane conformer of $\text{CH}_2\text{DCH}_2\text{CN}$ ($< 0.024\%$) and CH_3OD ($< 0.07\%$). The deuteration upper limits for the other non-detected deuterated species lie in the range 0.5–1.8%.

The following conclusions arise from this analysis:

1. Ethyl cyanide is less deuterated than methyl cyanide by at least a factor five. This may be due to their different formation pathways (grain surface versus gas phase).
2. The relative abundances of the three deuterated species of ethyl cyanide are most likely consistent with a statistical distribution.
3. The $[\text{CH}_2\text{DOH}]/[\text{CH}_3\text{OD}]$ abundance ratio in Sgr B2(N2) is higher than 1.8. It may still be consistent with the value obtained in Orion KL but a value closer to (or, like in low-mass Class 0 protostars, even higher than) the statistical value cannot be excluded.
4. Except for methyl cyanide, the levels of deuterium fractionation measured toward the hot core Sgr B2(N2) lie at least a factor four below the predictions of current astrochemical

models that were designed for lower mass objects (hot corinos in the Class 0 phase).

5. The levels of deuterium fractionation derived for complex organic molecules in Sgr B2(N2) are lower by a factor of a few up to a factor ten than in the Orion-KL Hot Core or Compact Ridge.

The discrepancy between the deuteration levels measured in Sgr B2(N2) and the predictions of current chemical models for complex organic molecules, and the difference between Sgr B2(N2) and Orion KL may both be due to the higher kinetic temperatures that prevail in the Galactic Center region compared to nearby star forming regions. Dedicated numerical simulations are needed to test this hypothesis. An alternative explanation for the low deuteration level of complex organic molecules in Sgr B2(N2) could be a lower abundance of deuterium itself in the Galactic Center region by up to a factor ten, as was also suggested by previous studies based on smaller molecules.

Acknowledgements. We thank Bérengère Parise for enlightening discussions about deuterium fractionation. This work has been supported in part by the Deutsche Forschungsgemeinschaft through the collaborative research grant SFB 956 “Conditions and Impact of Star Formation,” project area B3. R.T.G. acknowledges support from the NASA Astrophysics Theory Program through grant NNX11AC38G. This paper makes use of the following ALMA data: ADS/JAO.ALMA#2011.0.00017.S, ADS/JAO.ALMA#2012.1.00012.S. ALMA is a partnership of ESO (representing its member states), NSF (USA) and NINS (Japan), together with NRC (Canada), NSC and ASIAA (Taiwan), and KASI (Republic of Korea), in cooperation with the Republic of Chile. The Joint ALMA Observatory is operated by ESO, AUI/NRAO and NAOJ. The interferometric data are available in the ALMA archive at <https://almascience.eso.org/aq/>.

References

- Aikawa, Y., Wakelam, V., Hersant, F., Garrod, R. T., & Herbst, E. 2012, *ApJ*, 760, 40
- Anderson, T., Crownover, R. L., Herbst, E., & De Lucia, F. C. 1988, *ApJS*, 67, 135
- Baskakov, O. I., Dyubko, S. F., Ilyushin, V. V., et al. 1996, *J. Mol. Spectrosc.*, 179, 94
- Bauer, A. & Maes, S. 1969, *J. Phys. (Paris)*, 30, 169
- Bauer, A. 1971, *J. Mol. Spectrosc.*, 40, 183
- Belloche, A., Menten, K. M., Comito, C., et al. 2008, *A&A*, 482, 179
- Belloche, A., Garrod, R. T., Müller, H. S. P., et al. 2009, *A&A*, 499, 215
- Belloche, A., Müller, H. S. P., Menten, K. M., Schilke, P., & Comito, C. 2013, *A&A*, 559, A47
- Belloche, A., Garrod, R. T., Müller, H. S. P., & Menten, K. M. 2014, *Science*, 345, 1584
- Brauer, C. S., Pearson, J. C., Drouin, B. J., & Yu, S. 2009, *ApJS*, 184, 133
- Caselli, P., Hasegawa, T. I., & Herbst, E. 1993, *ApJ*, 408, 548
- Caselli, P., & Ceccarelli, C. 2012, *A&A Rev.*, 20, 56
- Cazzoli, G., & Kisiel, Z. 1988, *J. Mol. Spectrosc.*, 130, 303
- Ceccarelli, C., Caselli, P., Bockelée-Morvan, D., et al. 2014, *Protostars and Planets VI*, 859
- Charnley, S. B., Tielens, A. G. G. M., & Rodgers, S. D. 1997, *ApJ*, 482, L203
- Colmont, J. M., Wlodarczak, G., Priem, D., et al. 1997, *J. Mol. Spectrosc.*, 181, 330
- Comito, C., Schilke, P., Gerin, M., et al. 2003, *A&A*, 402, 635
- Coudert, L. H., Drouin, B. J., Tercero, B., et al. 2013, *ApJ*, 779, 119
- Creswell, R. A., Winnewisser, G., & Gerry, M. C. L. 1977, *J. Mol. Spectrosc.*, 65, 420

- Daly, A. M., Bermúdez, C., López, A., et al. 2013, *ApJ*, 768, 81
- Demaison, J., Dubrulle, A., Boucher, D., Burie, J., & Typke, V. 1979, *J. Mol. Spectrosc.*, 76, 1
- Duan, Y.-B., Ozier, I., Tsunekawa, S., & Takagi, K. 2003, *J. Mol. Spectrosc.*, 218, 95
- Esplugues, G. B., Cernicharo, J., Viti, S., et al. 2013, *A&A*, 559, A51
- Favre, C., Carvajal, M., Field, D., et al. 2014, *ApJS*, 215, 25
- Fayt, A., Vigouroux, C., Willaert, F., et al. 2004, *J. Mol. Struct.*, 695, 295
- Fontani, F., Busquet, G., Palau, A., et al. 2015, *A&A*, 575, A87
- Fuente, A., Cernicharo, J., Caselli, P., et al. 2014, *A&A*, 568, A65
- Fukuyama, Y., Odashima, H., Takagi, K., & Tsunekawa, S. 1996, *ApJS*, 104, 329
- Garrod, R. T., Weaver, S. L. W., & Herbst, E. 2008, *ApJ*, 682, 283
- Garrod, R. T. 2013, *ApJ*, 765, 60
- Gerin, M., Combes, F., Wlodarczak, G., et al. 1992, *A&A*, 259, L35
- Goldsmith, P. F., & Langer, W. D. 1999, *ApJ*, 517, 209
- Gottlieb, C. A., Ball, J. A., Gottlieb, E. W., & Dickinson, D. F. 1979, *ApJ*, 227, 422
- Heise, H. M., Winther, F., & Lutz, H. 1981, *J. Mol. Spectrosc.*, 90, 531
- Herbst, E., & van Dishoeck, E. F. 2009, *ARA&A*, 47, 427
- Hidaka, H., Watanabe, M., Kouchi, A., & Watanabe, N. 2009, *ApJ*, 702, 291
- Howe, D. A., Millar, T. J., Schilke, P., & Walmsley, C. M. 1994, *MNRAS*, 267, 59
- Ilyushin, V., Kryvda, A., & Alekseev, E. 2009, *J. Mol. Spectrosc.*, 255, 32
- Jacq, T., Walmsley, C. M., Henkel, C., et al. 1990, *A&A*, 228, 447
- Jacq, T., Walmsley, C. M., Mauersberger, R., et al. 1993, *A&A*, 271, 276
- Jacq, T., Baudry, A., Walmsley, C. M., & Caselli, P. 1999, *A&A*, 347, 957
- Kisiel, Z., Martin-Drumel, M. A., & Pirali, O. 2015, *J. Mol. Spectrosc.*, 315, 83
- Langer, W. D., Schloerb, F. P., Snell, R. L., & Young, J. S. 1980, *ApJ*, 239, L125
- Lauvergnat, D., Coudert, L. H., Klee, S., & Smirnov, M. 2009, *J. Mol. Spectrosc.*, 256, 204
- Linsky, J. L. 2003, *Space Sci. Rev.*, 106, 49
- Lubowich, D. A., Pasachoff, J. M., Balonek, T. J., et al. 2000, *Nature*, 405, 1025
- Maret, S., Hily-Blant, P., Pety, J., Bardeau, S., & Reynier, E. 2011, *A&A*, 526, A47
- Margulès, L., Motiyenko, R., Demyk, K., et al. 2009, *A&A*, 493, 565
- Müller, H. S. P., Thorwirth, S., Roth, D. A., & Winnewisser, G. 2001, *A&A*, 370, L49
- Müller, H. S. P., Schlöder, F., Stutzki, J., & Winnewisser, G. 2005, *J. Mol. Struct.*, 742, 215
- Müller, H. S. P., Belloche, A., Menten, K. M., Comito, C., & Schilke, P. 2008, *J. Mol. Spectrosc.*, 251, 319
- Müller, H. S. P., Drouin, B. J., & Pearson, J. C. 2009, *A&A*, 506, 1487
- Müller, H. S. P., Brown, L. R., Drouin, B. J., et al. 2015a, *J. Mol. Spectrosc.*, 312, 22
- Müller, H. S. P., Drouin, B. J., & Pearson, J. C., et al. 2015b, *A&A*, submitted
- Müller, H. S. P., Belloche, A., Xu, L.-H., et al. 2015c, *A&A*, submitted
- Nagaoka, A., Watanabe, N., & Kouchi, A. 2005, *ApJ*, 624, L29
- Neill, J. L., Crockett, N. R., Bergin, E. A., Pearson, J. C., & Xu, L.-H. 2013, *ApJ*, 777, 85
- Nguyen, L., Walters, A., Margulès, L., et al. 2013, *A&A*, 553, A84
- Osamura, Y., Roberts, H., & Herbst, E. 2004, *A&A*, 421, 1101
- Ott, J., Weiß, A., Staveley-Smith, L., Henkel, C., & Meier, D. S. 2014, *ApJ*, 785, 55
- Parise, B., Ceccarelli, C., Tielens, A. G. G. M., et al. 2002, *A&A*, 393, L49
- Parise, B., Castets, A., Herbst, E., et al. 2004, *A&A*, 416, 159
- Parise, B., Ceccarelli, C., Tielens, A. G. G. M., et al. 2006, *A&A*, 453, 949
- Parise, B., Leurini, S., Schilke, P., et al. 2009, *A&A*, 508, 737
- Pearson, J. C., Yu, S., & Drouin, B. J. 2012, *J. Mol. Spectrosc.*, 280, 119
- Peng, T.-C., Despois, D., Brouillet, N., Parise, B., & Baudry, A. 2012, *A&A*, 543, A152
- Pickett, H. M., Poynter, R. L., Cohen, E. A., Delitsky, M. L., Pearson, J. C., & Müller, H. S. P. 1998, *J. Quant. Spectr. Rad. Transf.*, 60, 883
- Pillai, T., Wyrowski, F., Hatchell, J., Gibb, A. G., & Thompson, M. A. 2007, *A&A*, 467, 207
- Polehampton, E. T., Baluteau, J.-P., Ceccarelli, C., Swinyard, B. M., & Caux, E. 2002, *A&A*, 388, L44
- Qin, S.-L., Schilke, P., Rolfs, R., et al. 2011, *A&A*, 530, L9
- Ratajczak, A., Quirico, E., Faure, A., Schmitt, B., & Ceccarelli, C. 2009, *A&A*, 496, L21
- Ratajczak, A., Taquet, V., Kahane, C., et al. 2011, *A&A*, 528, L13
- Reid, M. J., Menten, K. M., Brunthaler, A., et al. 2014, *ApJ*, 783, 130
- Remijan, A., et al. 2015, *ALMA Cycle 3 Technical Handbook Version 1.0*, ALMA, ISBN 978-3-923524-66-2
- Richard, C., Margulès, L., Motiyenko, R. A., & Guillemin, J.-C. 2012, *A&A*, 543, A135
- Rolfs, R., Schilke, P., Wyrowski, F., et al. 2011, *A&A*, 527, A68
- Sakai, N., Sakai, T., Hirota, T., & Yamamoto, S. 2009, *ApJ*, 702, 1025
- Spahn, H., Müller, H. S. P., Giesen, T. F., et al. 2008, *Chem. Phys.*, 346, 132
- Taquet, V., Ceccarelli, C., & Kahane, C. 2012, *ApJ*, 748, L3
- Taquet, V., Charnley, S. B., & Sipilä, O. 2014, *ApJ*, 791, 1
- Thorwirth, S., Müller, H. S. P., & Winnewisser, G. 2000, *J. Mol. Spectrosc.*, 204, 133
- Thorwirth, S., Müller, H. S. P., & Winnewisser, G. 2001, *Phys. Chem. Chem. Phys.*, 3, 1236
- Turner, B. E. 2001, *ApJS*, 136, 579
- Uyemura, M., Deguchi, S., Nakada, Y., & Onaka, T. 1982, *Bull. Chem. Soc. Jpn.*, 55, 384
- Walters, A., Schäfer, M., Ordu, M. H., et al. 2015, *J. Mol. Spectrosc.*, 314, 6
- Watanabe, Y., Sakai, N., López-Sepulcre, A., et al. 2015, *ApJ*, 809, 162
- Yamada, K. M. T., & Creswell, R. A. 1986, *J. Mol. Spectrosc.*, 116, 384

Table 4. Parameters of our best-fit LTE model (or upper limit) of selected (complex) organic molecules toward Sgr B2(N2).

Molecule	Status ^a	N_{det}^b	Size ^c ($''$)	T_{rot}^d (K)	N^e (cm^{-2})	C^f	ΔV^g (km s^{-1})	V_{off}^h (km s^{-1})	$\frac{N_{\text{ref}}^i}{N}$	30 m ^j
CH_3CN , $v_8 = 1^*$	d	20	1.40	170	2.2 (18)	1.00	5.4	-0.5	1	y
$v_8 = 2$	d	8	1.40	170	7.5 (18)	1.00	6.5	-0.5	0.29	y
$v_4 = 1$	t	1	1.40	170	2.0 (19)	1.00	6.5	-0.5	0.11	y
$^{13}\text{CH}_3\text{CN}$, $v = 0$	d	8	1.40	170	1.1 (17)	1.18	5.4	-0.5	21	y
$v_8 = 1$	d	3	1.40	170	1.1 (17)	1.18	5.4	-0.5	21	y
$\text{CH}_3^{13}\text{CN}$, $v = 0$	d	7	1.40	170	1.1 (17)	1.18	5.4	-0.5	21	y
$v_8 = 1$	d	9	1.40	170	1.1 (17)	1.18	5.4	-0.5	21	y
$^{13}\text{CH}_3^{13}\text{CN}$	d	1	1.40	170	4.7 (15)	1.18	5.4	-0.5	466	n
$\text{CH}_3\text{C}^{15}\text{N}$	t	0	1.40	170	8.3 (15)	1.18	5.4	-0.5	266	n
CH_2DCN	d	6	1.40	170	8.3 (15)	1.18	5.4	-0.6	266	n
$\text{C}_2\text{H}_5\text{CN}^*$	d	154	1.20	150	6.9 (18)	1.53	5.0	-0.8	1	y
$^{13}\text{CH}_3\text{CH}_2\text{CN}$	d	54	1.20	150	2.1 (17)	1.53	5.0	-0.8	32	y
$\text{CH}_3^{13}\text{CH}_2\text{CN}$	d	38	1.20	150	2.1 (17)	1.53	5.0	-0.8	32	y
$\text{CH}_3\text{CH}_2^{13}\text{CN}$	d	37	1.20	150	2.1 (17)	1.53	5.0	-0.8	32	y
$\text{C}_2\text{H}_5\text{C}^{15}\text{N}$	d	9	1.20	150	1.4 (16)	1.53	5.0	-0.8	500	n
$\text{CH}_2\text{DCH}_2\text{CN}$ (out of plane)	t	2	1.20	150	3.4 (15)	1.53	5.0	-0.8	2045	n
$\text{CH}_2\text{DCH}_2\text{CN}$ (in plane)	n	0	1.20	150	< 1.7 (15)	1.53	5.0	-0.8	> 4091	n
CH_3CHDCN	t	1	1.20	150	3.4 (15)	1.53	5.0	-0.8	2045	n
$\text{C}_2\text{H}_3\text{CN}$, $v = 0^*$	d	44	1.10	200	4.2 (17)	1.00	6.0	-0.6	1	y
$v_{11} = 1$	d	30	1.10	200	4.2 (17)	1.00	6.0	-0.5	1	y
$v_{15} = 1$	d	20	1.10	200	4.2 (17)	1.00	6.0	-0.5	1	y
$v_{11} = 2$	d	6	1.10	200	4.2 (17)	1.00	6.0	-0.5	1	y
$^{13}\text{CH}_2\text{CHCN}$	d	10	1.10	200	2.1 (16)	1.38	6.0	-0.6	20	y
$\text{CH}_2^{13}\text{CHCN}$	d	9	1.10	200	2.1 (16)	1.38	6.0	-0.6	20	y
$\text{CH}_2\text{CH}^{13}\text{CN}$	d	8	1.10	200	2.1 (16)	1.38	6.0	-0.6	20	y
$\text{C}_2\text{H}_3\text{C}^{15}\text{N}$	n	0	1.10	200	< 3.4 (15)	1.38	6.0	-0.6	> 122	n
<i>cis</i> -CHDCHCN	n	0	1.10	200	< 3.4 (15)	1.38	6.0	-0.6	> 122	n
<i>trans</i> -CHDCHCN	n	0	1.10	200	< 3.4 (15)	1.38	6.0	-0.6	> 122	n
CH_2CDCN	n	0	1.10	200	< 2.1 (15)	1.38	6.0	-0.6	> 203	n
HC_3N , $v_7 = 1^*$	d	6	1.30	170	3.5 (17)	1.44	5.0	-0.7	1	y
H^{13}CCCN , $v = 0$	d	2	1.30	170	1.7 (16)	1.44	5.0	-0.7	20	y
$v_7 = 1$	d	4	1.30	170	1.7 (16)	1.44	5.0	-1.0	20	y
HC^{13}CCN , $v = 0$	d	3	1.30	170	1.7 (16)	1.44	5.0	-0.7	20	y
$v_7 = 1$	d	3	1.30	170	1.7 (16)	1.44	5.0	-1.0	20	y
HCC^{13}CN , $v = 0$	d	3	1.30	170	1.7 (16)	1.44	5.0	-0.7	20	y
$v_7 = 1$	d	3	1.30	170	1.7 (16)	1.44	5.0	-1.0	20	y
$\text{H}^{13}\text{C}^{13}\text{CCN}$	t	1	1.30	170	7.2 (14)	1.44	5.0	-0.7	480	n
$\text{H}^{13}\text{CC}^{13}\text{CN}$	t	0	1.30	170	7.2 (14)	1.44	5.0	-0.7	480	y
$\text{HC}^{13}\text{C}^{13}\text{CN}$	t	1	1.30	170	7.2 (14)	1.44	5.0	-0.7	480	n
HC_3^{15}N	t	0	1.30	170	1.2 (15)	1.44	5.0	-0.7	300	y
DC_3N	t	0	1.30	170	3.0 (14)	1.51	5.0	-0.5	1144	n
CH_3OH , $v_t = 1^*$	d	16	1.40	160	4.0 (19)	1.00	5.4	-0.2	1	y
CH_2DOH	t	2	1.40	160	4.8 (16)	1.15	5.4	-0.5	828	n
CH_3OD	n	0	1.40	160	< 2.6 (16)	1.05	5.4	-0.5	> 1524	n
$\text{C}_2\text{H}_5\text{OH}^*$	d	168	1.25	150	2.0 (18)	1.24	5.4	0.0	1	y
$\text{CH}_3\text{CH}_2\text{OD}$	n	0	1.25	150	< 3.0 (16)	2.96	5.4	0.0	> 67	n
CH_3CHDOH	n	0	1.25	150	< 3.0 (16)	2.96	5.4	0.0	> 67	n
$\text{CH}_2\text{DCH}_2\text{OH}$ (out of plane)	n	0	1.25	150	< 3.0 (16)	2.96	5.4	0.0	> 67	n
$\text{CH}_2\text{DCH}_2\text{OH}$ (in plane)	n	0	1.25	150	< 2.1 (16)	2.96	5.4	0.0	> 96	n
CH_3OCHO , $v_t = 0^*$	d	90	1.50	150	1.2 (18)	1.23	4.7	-0.4	1	y
$v_t = 1$	d	35	1.50	150	1.2 (18)	1.23	4.7	-0.4	1	y
CH_2DOCHO (out of plane)	n	0	1.50	150	< 2.5 (16)	1.07	4.7	-0.4	> 50	n
CH_2DOCHO (in plane)	n	0	1.50	150	< 7.3 (15)	0.52	4.7	-0.4	> 167	n

Notes. ^(a) d: detection, t: tentative detection, n: non-detection. ^(b) Number of detected lines (conservative estimate, see Sect. 3). One line of a given species may mean a group of transitions of that species that are blended together. ^(c) Source diameter (*FWHM*). ^(d) Rotational temperature. ^(e) Total column density of the molecule. $X(Y)$ means $X \times 10^Y$. ^(f) Correction factor that was applied to the column density to account for the contribution of vibrationally or torsionally excited states or other conformers (e.g., *gauche* for ethanol), in the cases where this contribution was not included in the partition function of the spectroscopic predictions. For deuterated methyl formate, it is the scaling factor used to compute the column density of each conformer as if it were an independent species. ^(g) Linewidth (*FWHM*). ^(h) Velocity offset with respect to the assumed systemic velocity of Sgr B2(N2), $V_{\text{lsr}} = 74 \text{ km s}^{-1}$. ⁽ⁱ⁾ Column density ratio, with N_{ref} the column density of the previous reference species marked with a \star . ^(j) Detected (y) or not detected (n) toward Sgr B2(N) (N1 and/or N2) with the IRAM 30 m telescope (Belloche et al. 2013).

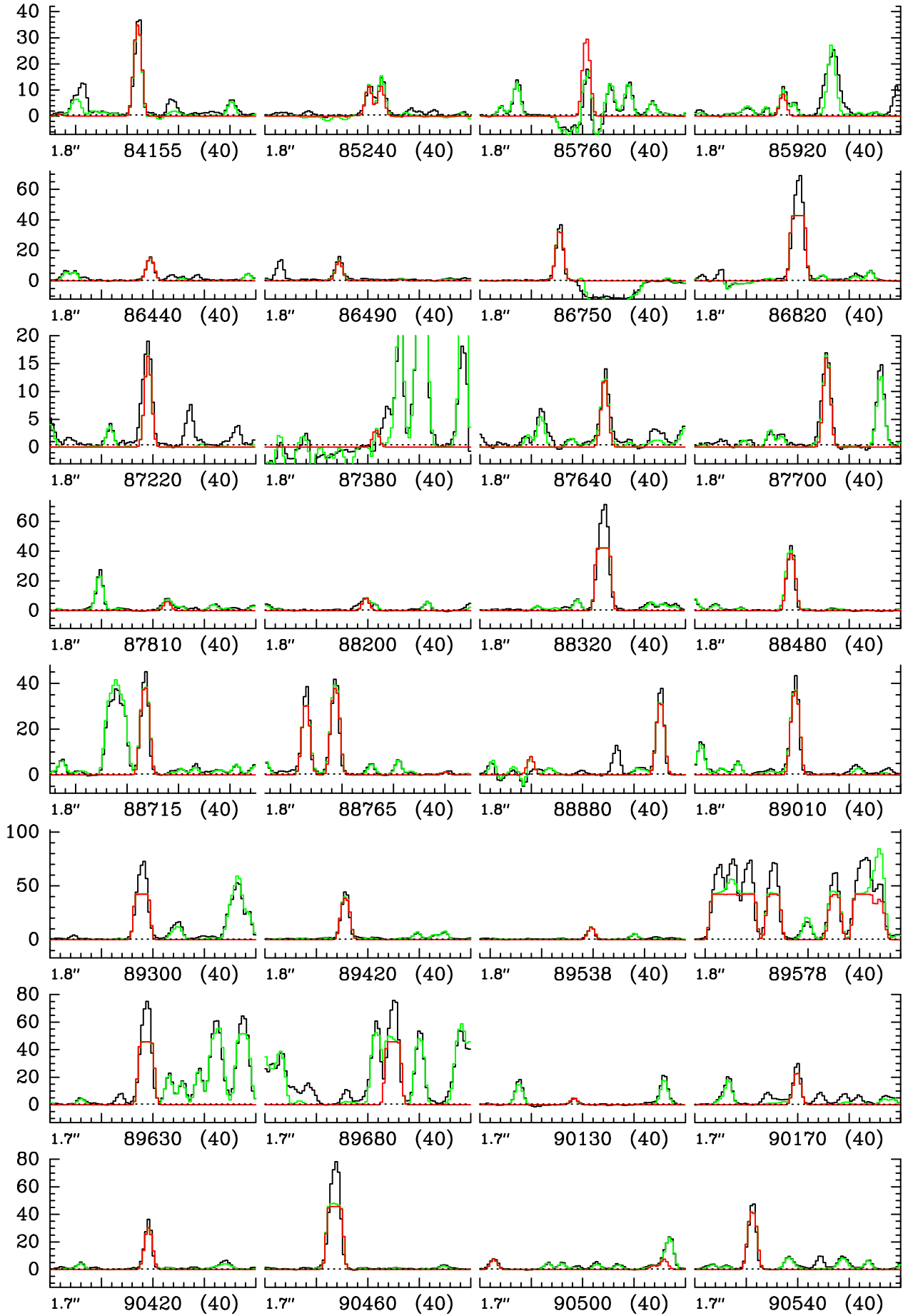


Fig. 1. Transitions of $\text{C}_2\text{H}_5\text{CN}$, $v = 0$ covered by our ALMA survey. The best-fit LTE synthetic spectrum of $\text{C}_2\text{H}_5\text{CN}$ is displayed in red and overlaid on the observed spectrum of Sgr B2(N2) shown in black. The green synthetic spectrum contains the contributions of all molecules identified in our survey so far, including the one shown in red. The central frequency and width are indicated in MHz below each panel. The angular resolution (HPBW) is also indicated. The y-axis is labeled in brightness temperature units (K). The dotted line indicates the 3σ noise level.

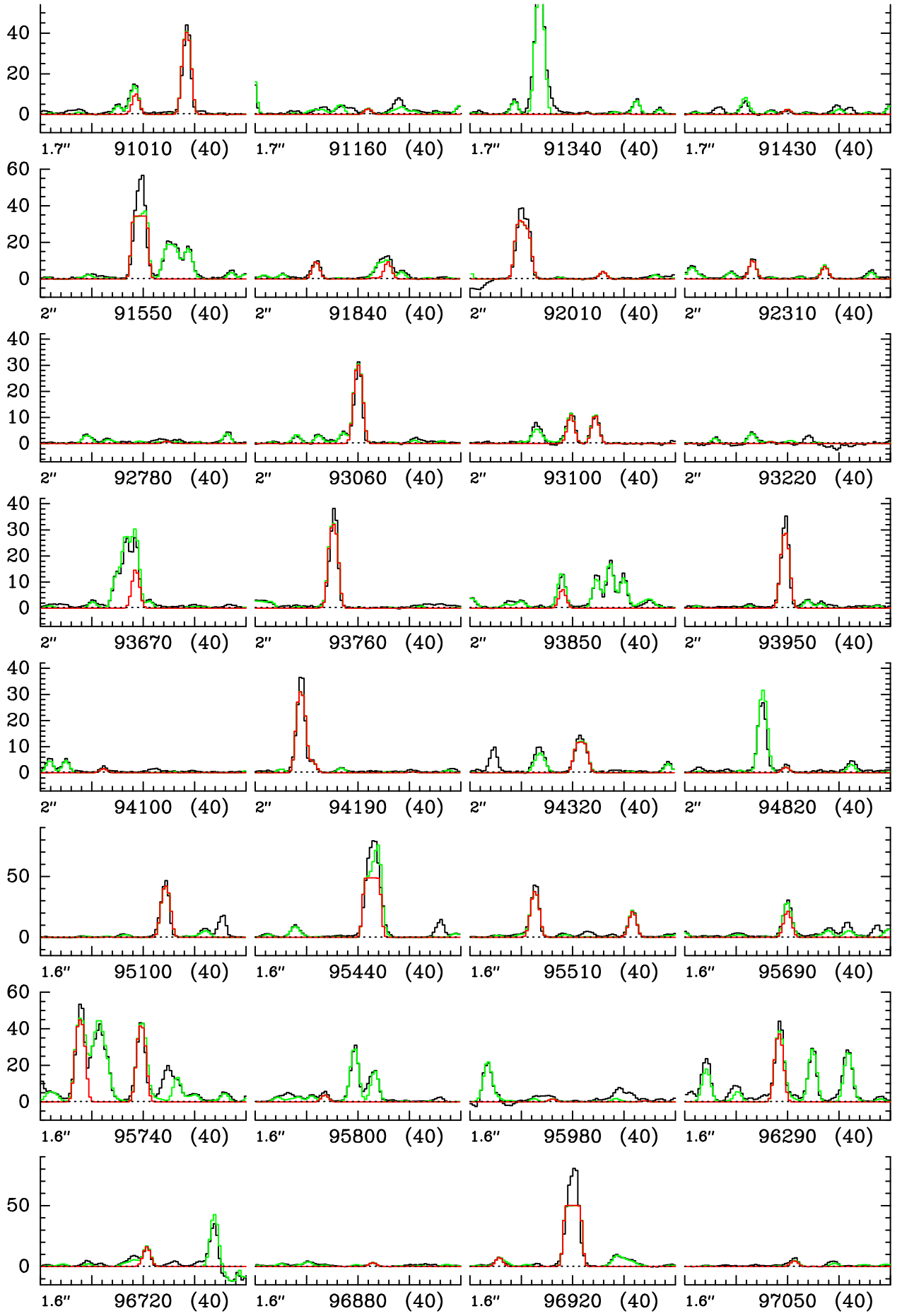


Fig. 1. continued.

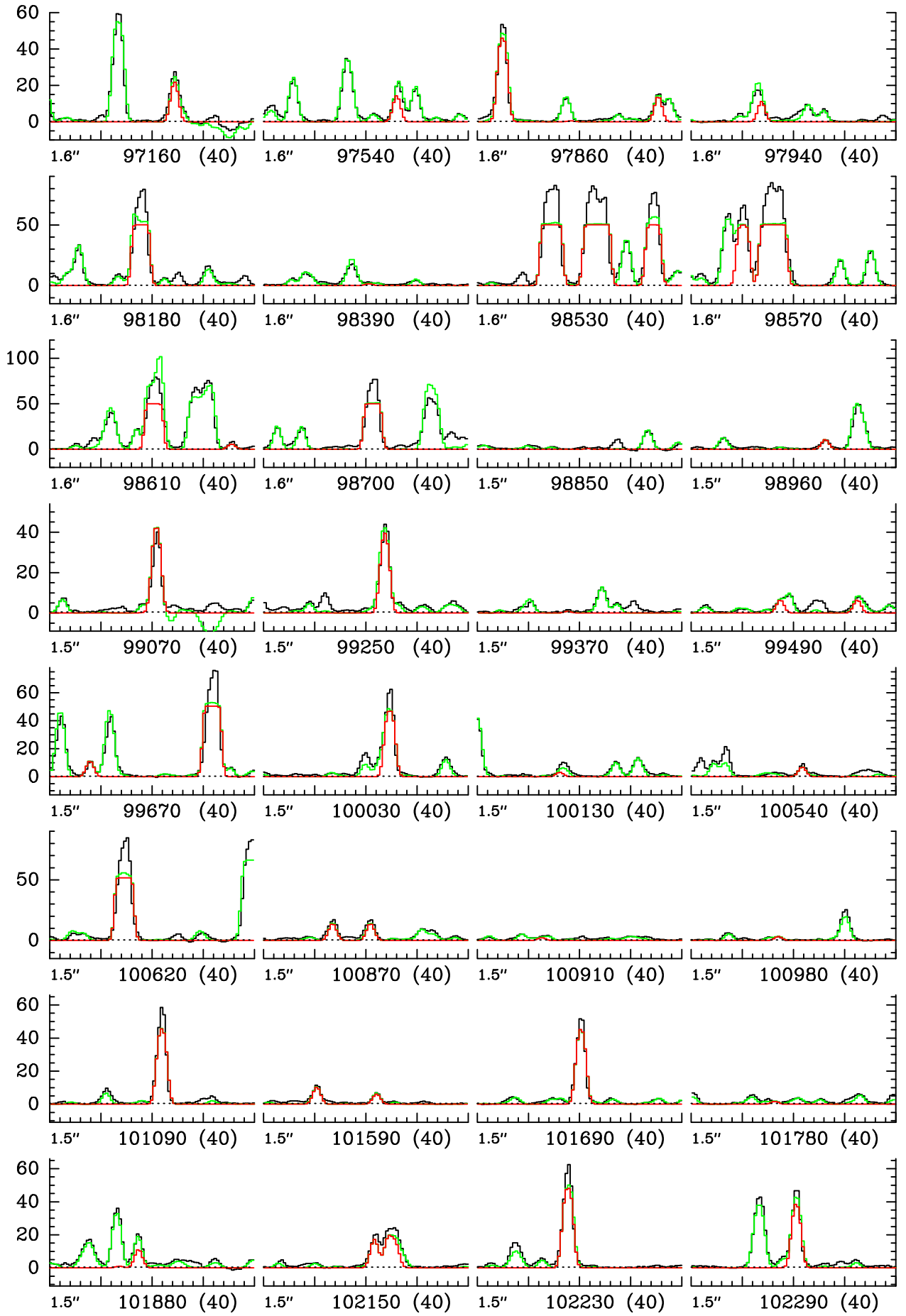


Fig. 1. continued.

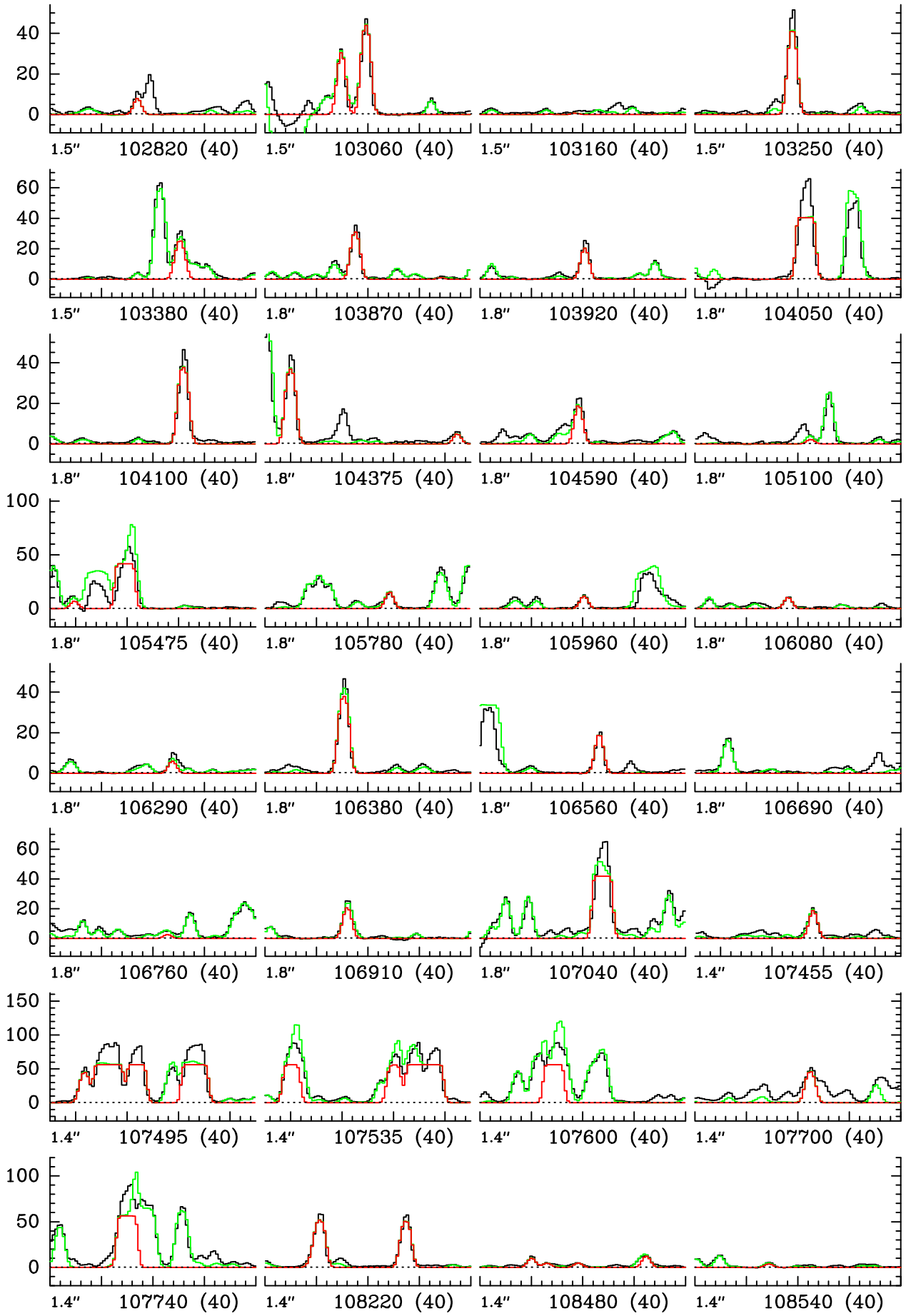


Fig. 1. continued.

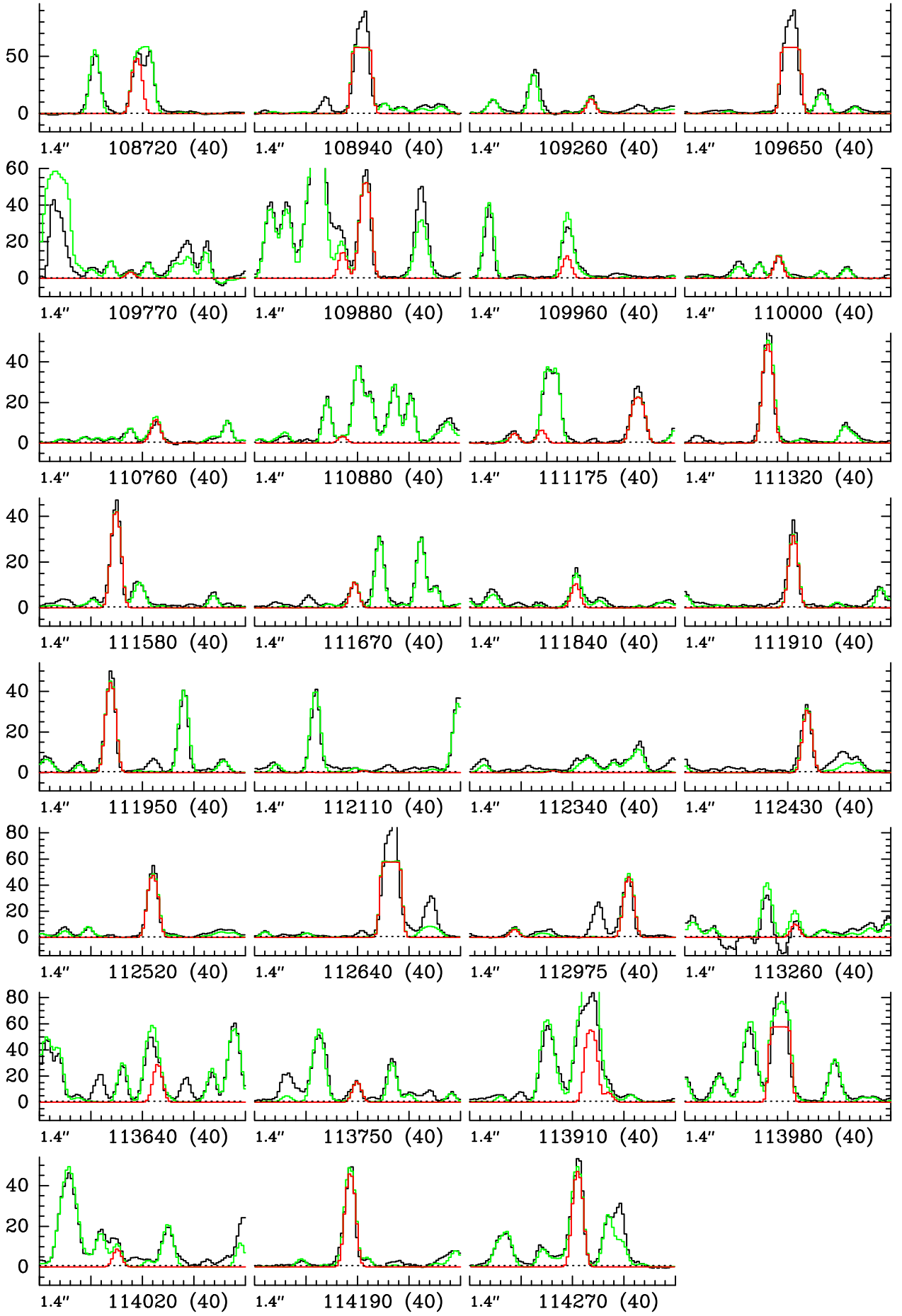


Fig. 1. continued.

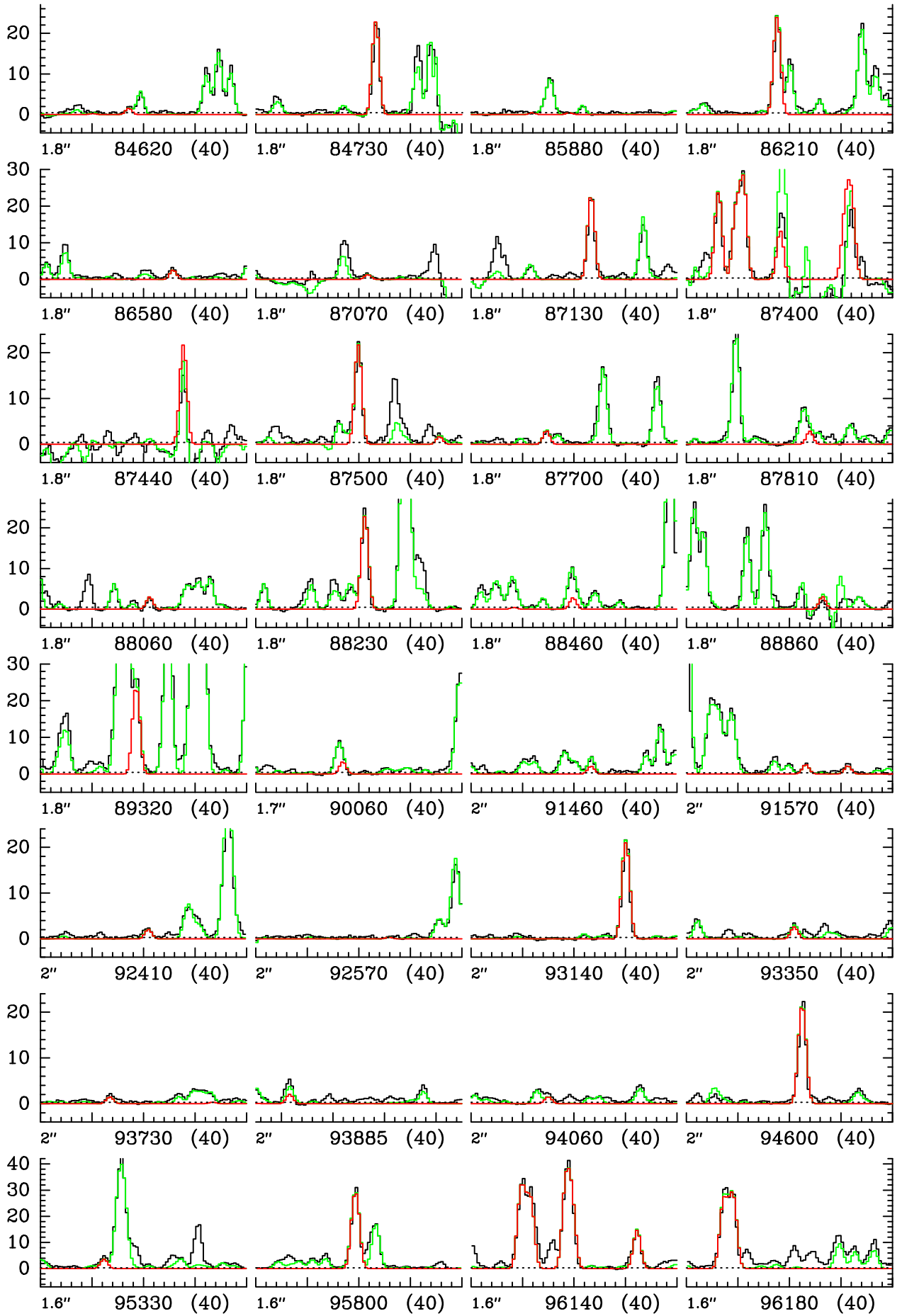


Fig. 2. Same as Fig. 1 for $^{13}\text{CH}_3\text{CH}_2\text{CN}$, $v = 0$.

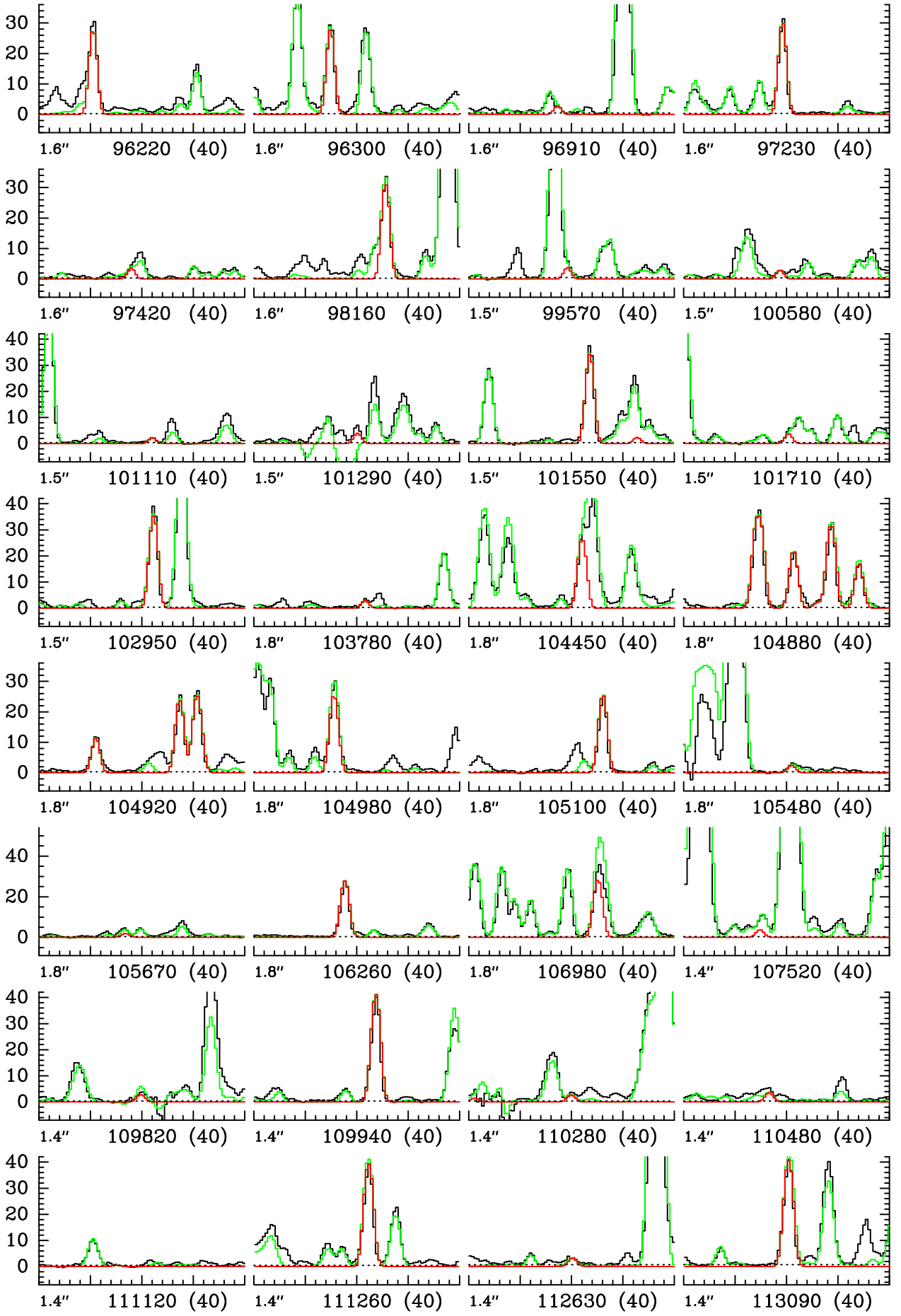


Fig. 2. continued.

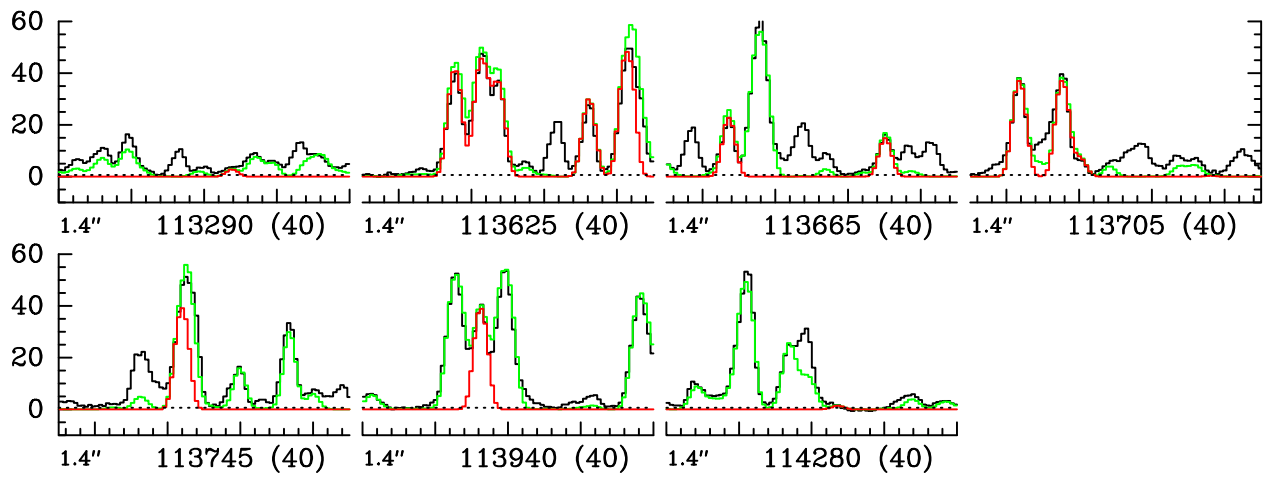


Fig. 2. continued.

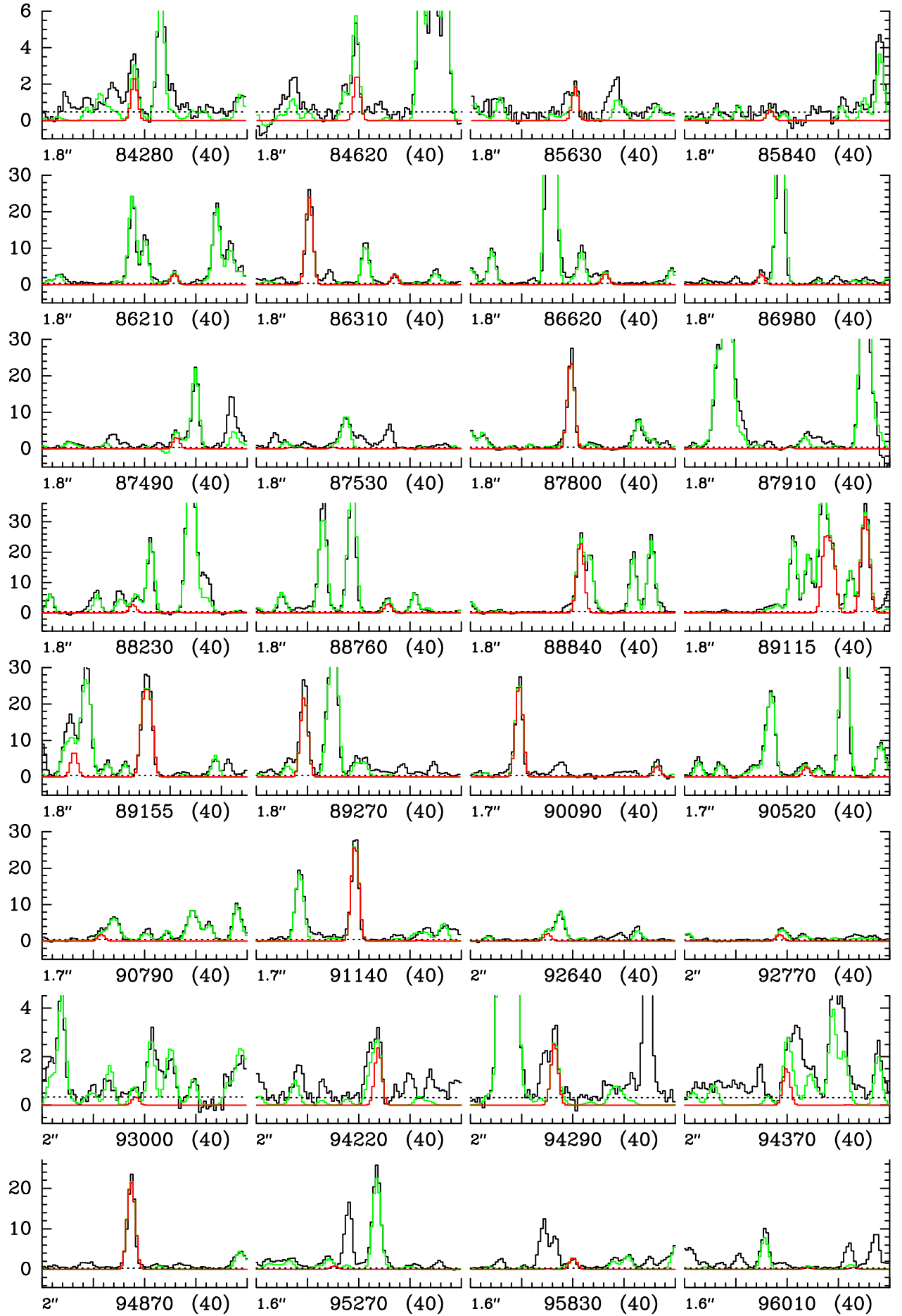


Fig. 3. Same as Fig. 1 for $\text{CH}_3\text{-}^{13}\text{CH}_2\text{CN}$, $v=0$.

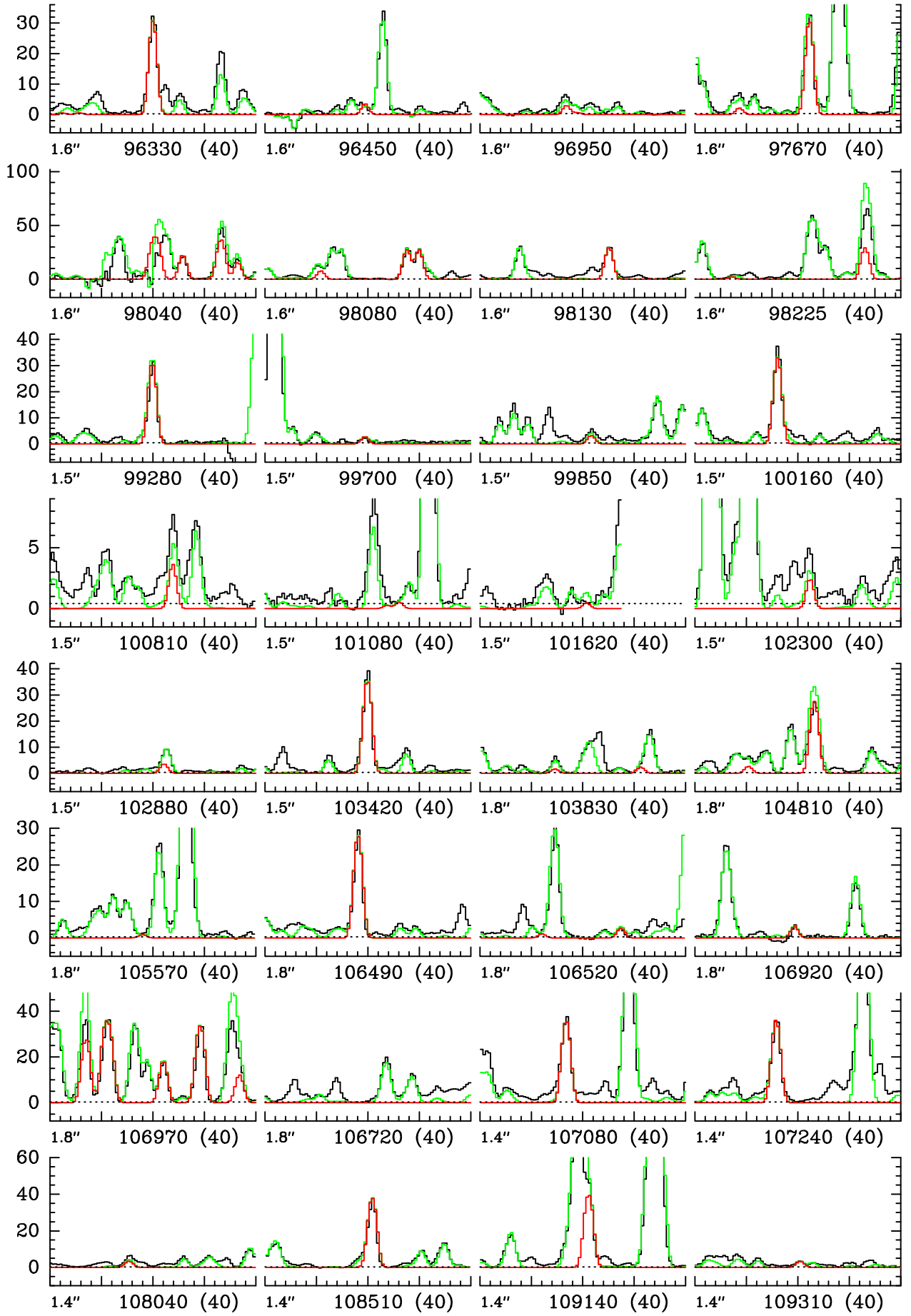


Fig. 3. continued.

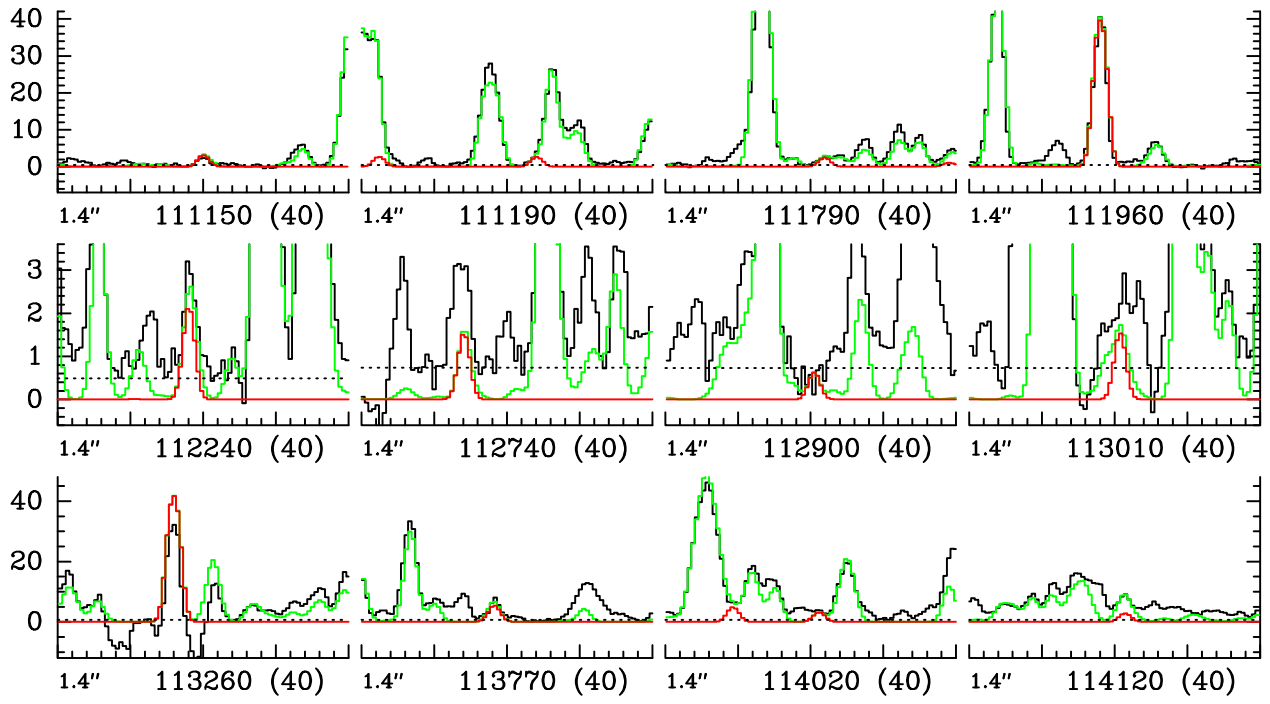


Fig. 3. continued.

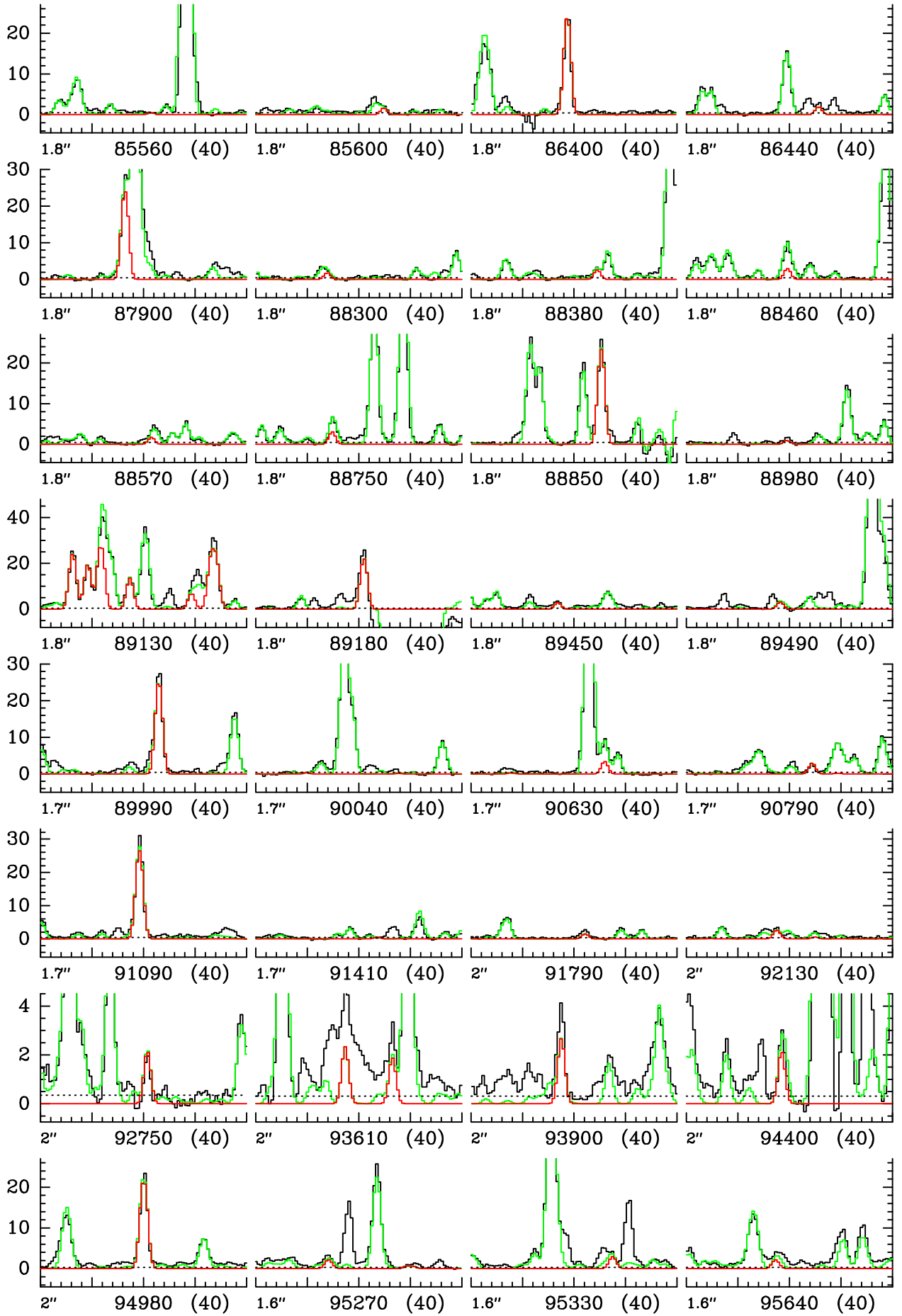


Fig. 4. Same as Fig. 1 for $\text{CH}_3\text{CH}_2^{13}\text{CN}$, $v = 0$.

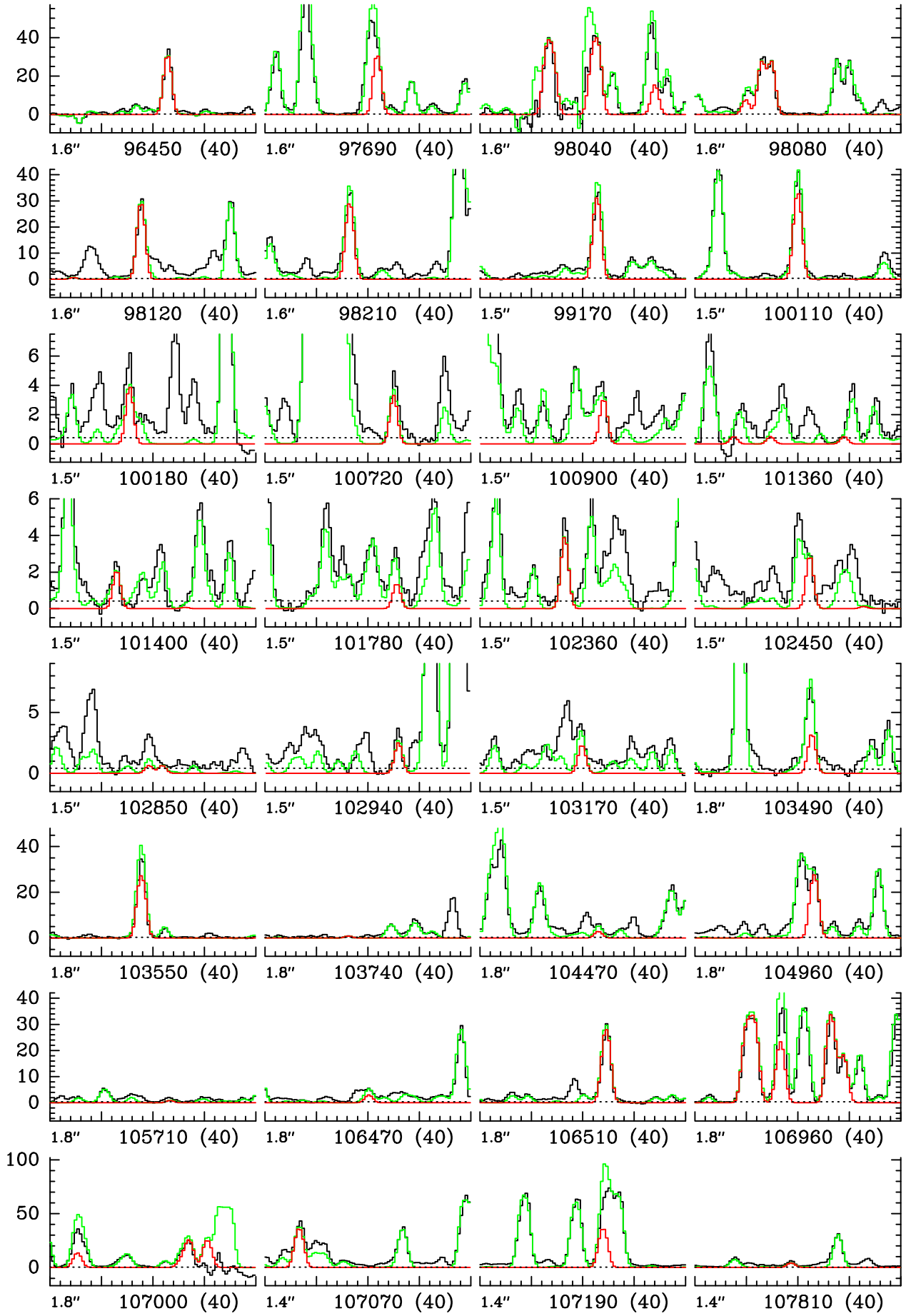


Fig. 4. continued.

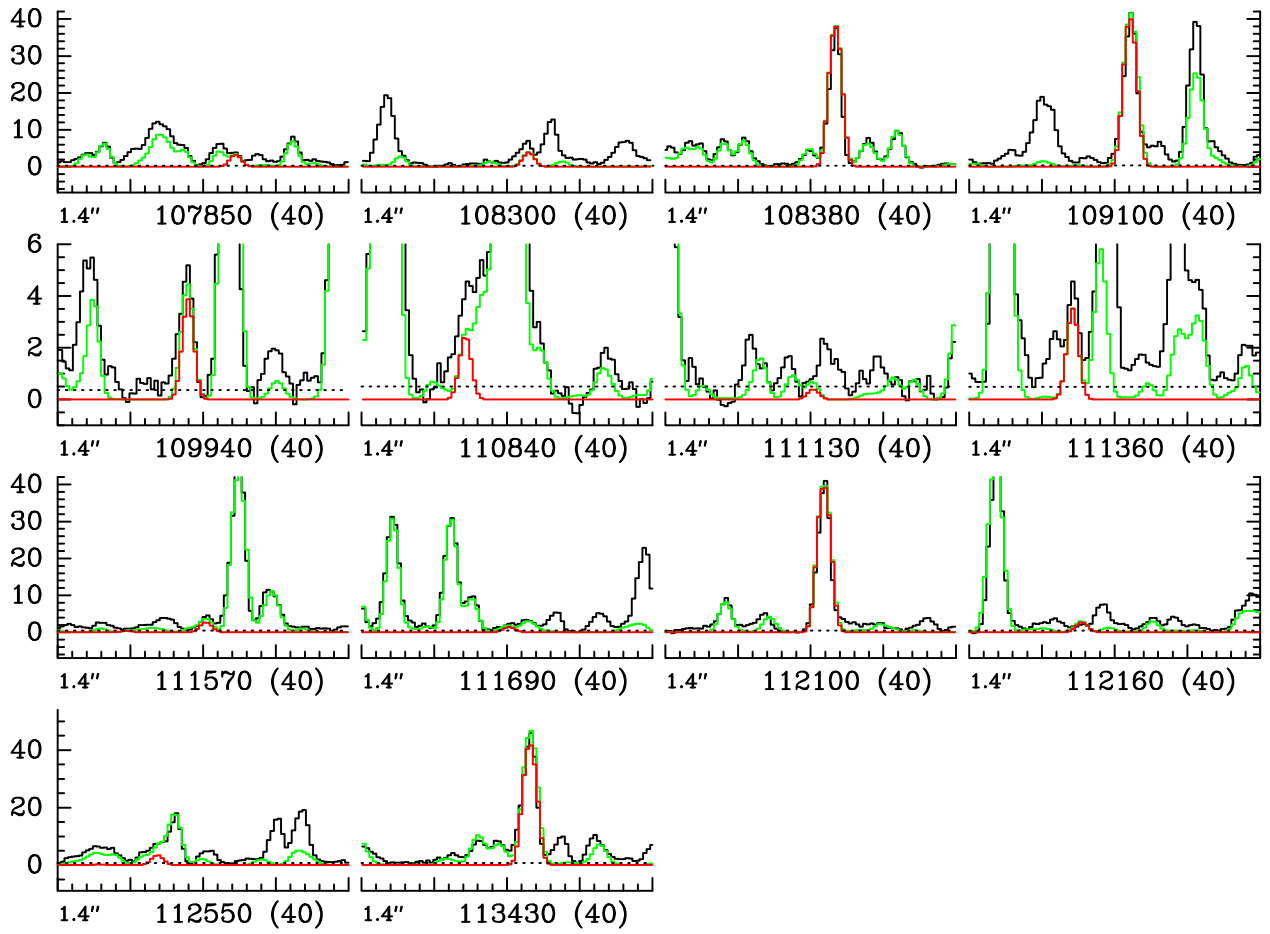


Fig. 4. continued.

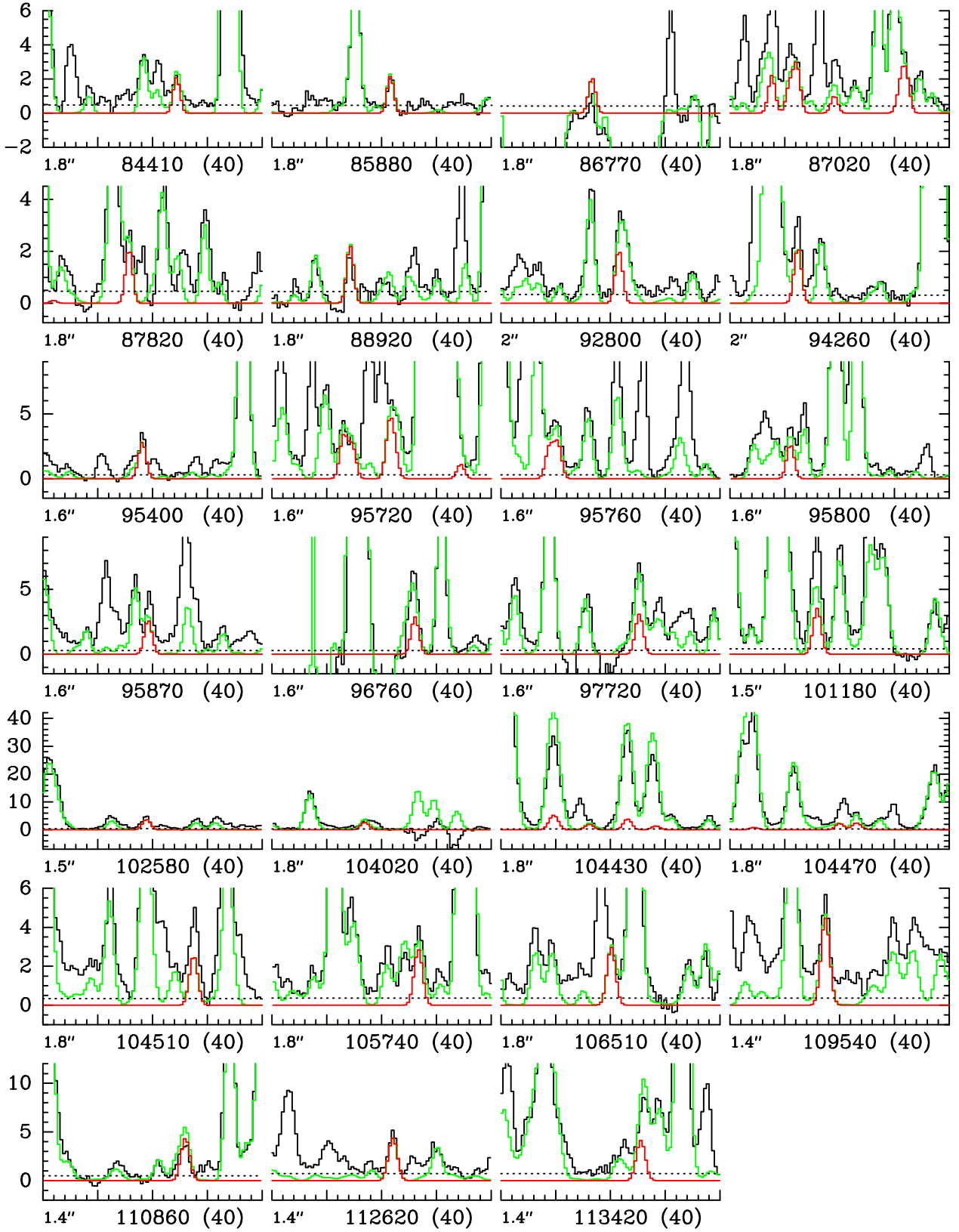


Fig. 5. Same as Fig. 1 for $\text{C}_2\text{H}_5\text{C}^{15}\text{N}$, $v = 0$.

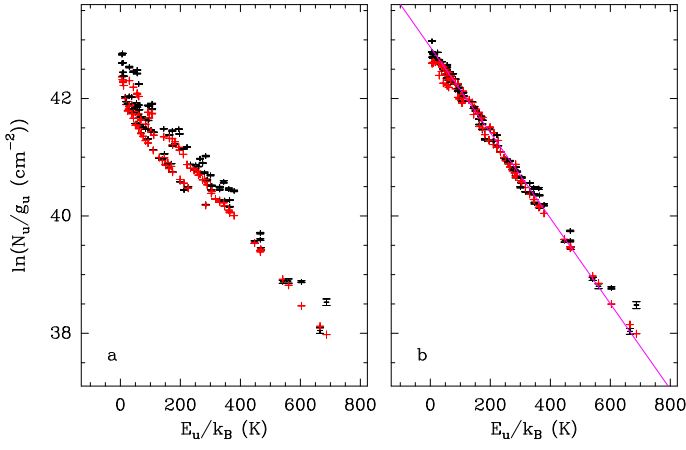


Fig. 6. Population diagram of $\text{C}_2\text{H}_5\text{CN}$, $v = 0$ toward Sgr B2(N2). Only the lines that are clearly detected, do not suffer too much from contamination from other species, and have an opacity below 2.5 are displayed. The observed datapoints are shown in black while the synthetic populations are shown in red. No correction is applied in panel **a**. In panel **b**, the optical depth correction has been applied to both the observed and synthetic populations and the contamination from all other species included in the full model has been removed from the observed datapoints. The purple line is a linear fit to the observed populations (in linear-logarithmic space).

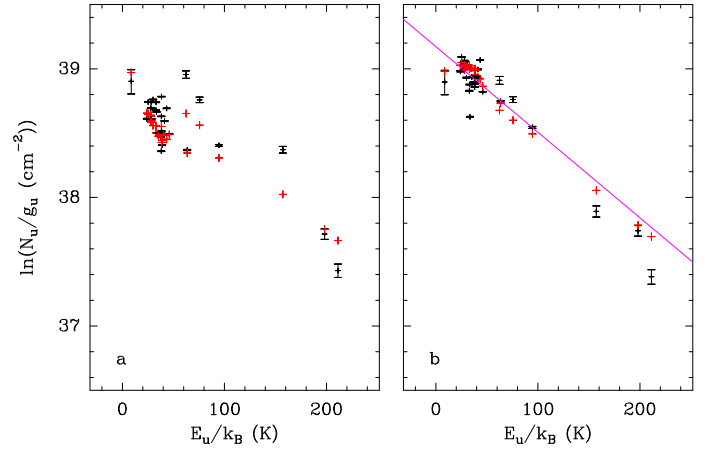


Fig. 9. Same as Fig. 6 for $\text{CH}_3\text{CH}_2^{13}\text{CN}$, $v = 0$.

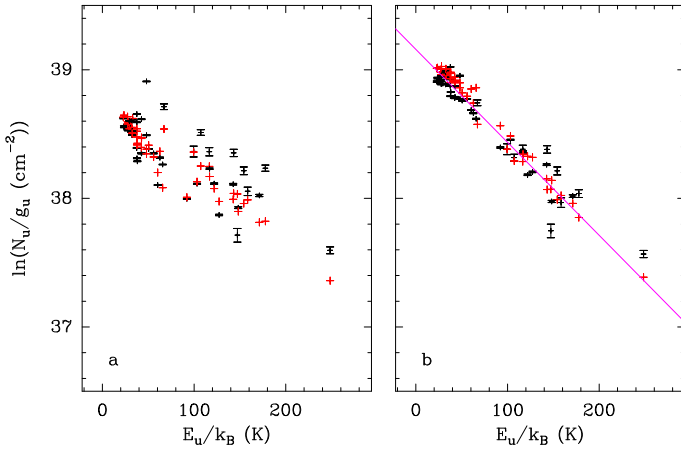


Fig. 7. Same as Fig. 6 for $^{13}\text{CH}_3\text{CH}_2\text{CN}$, $v = 0$.

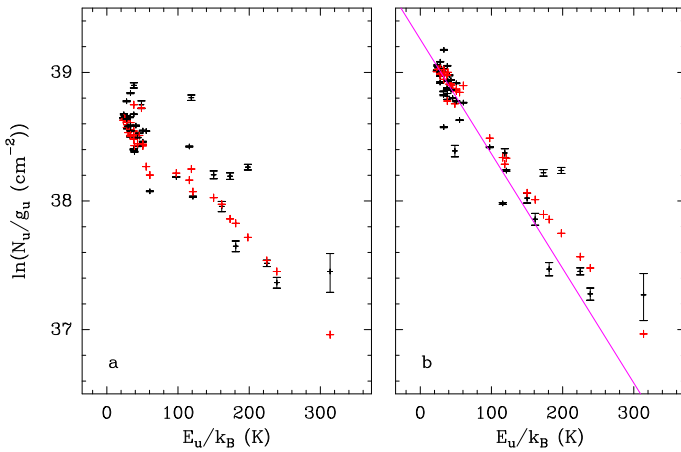


Fig. 8. Same as Fig. 6 for $\text{CH}_3^{13}\text{CH}_2\text{CN}$, $v = 0$.

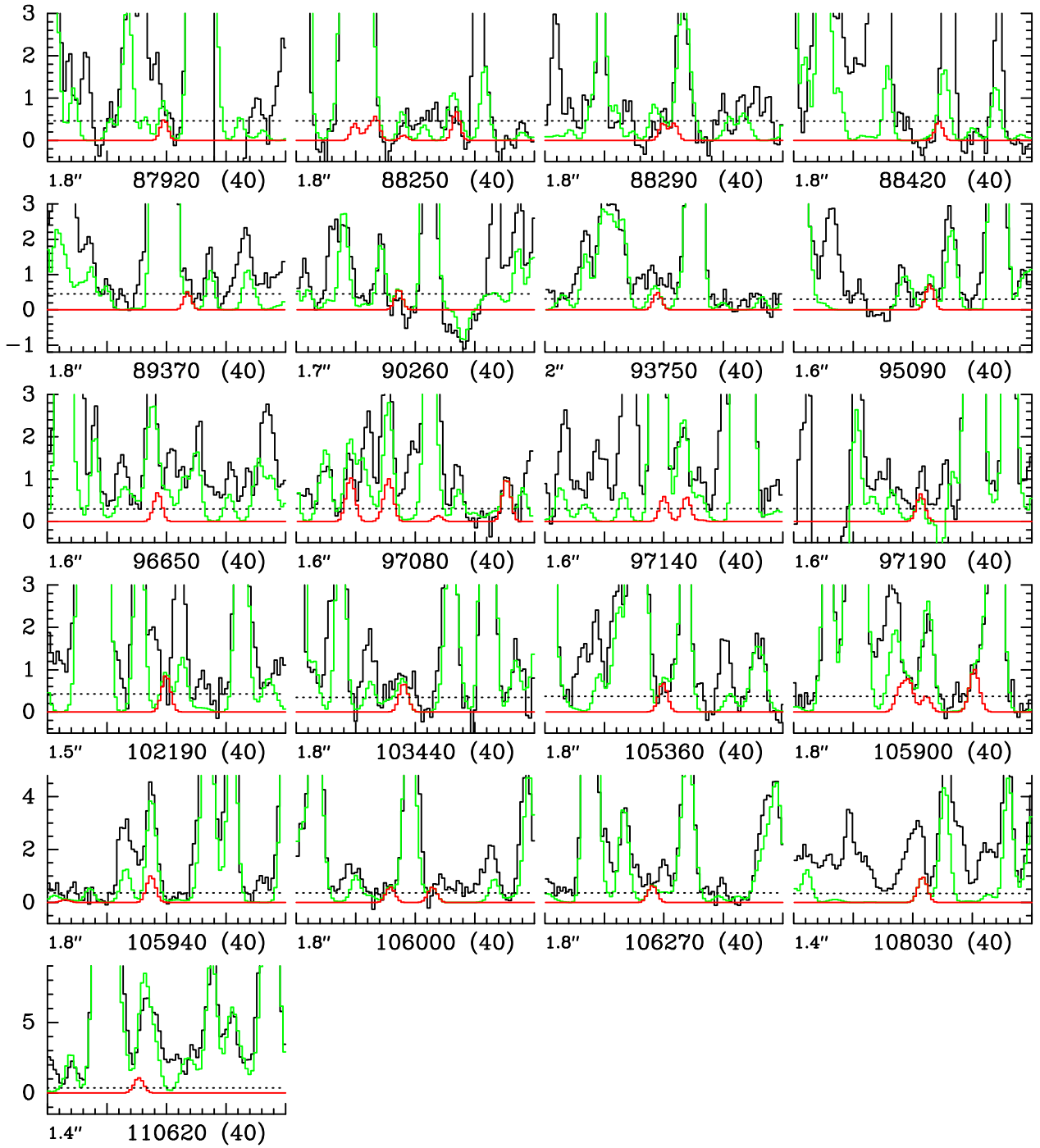


Fig. 11. Same as Fig. 1 for CH_3CHDCN .

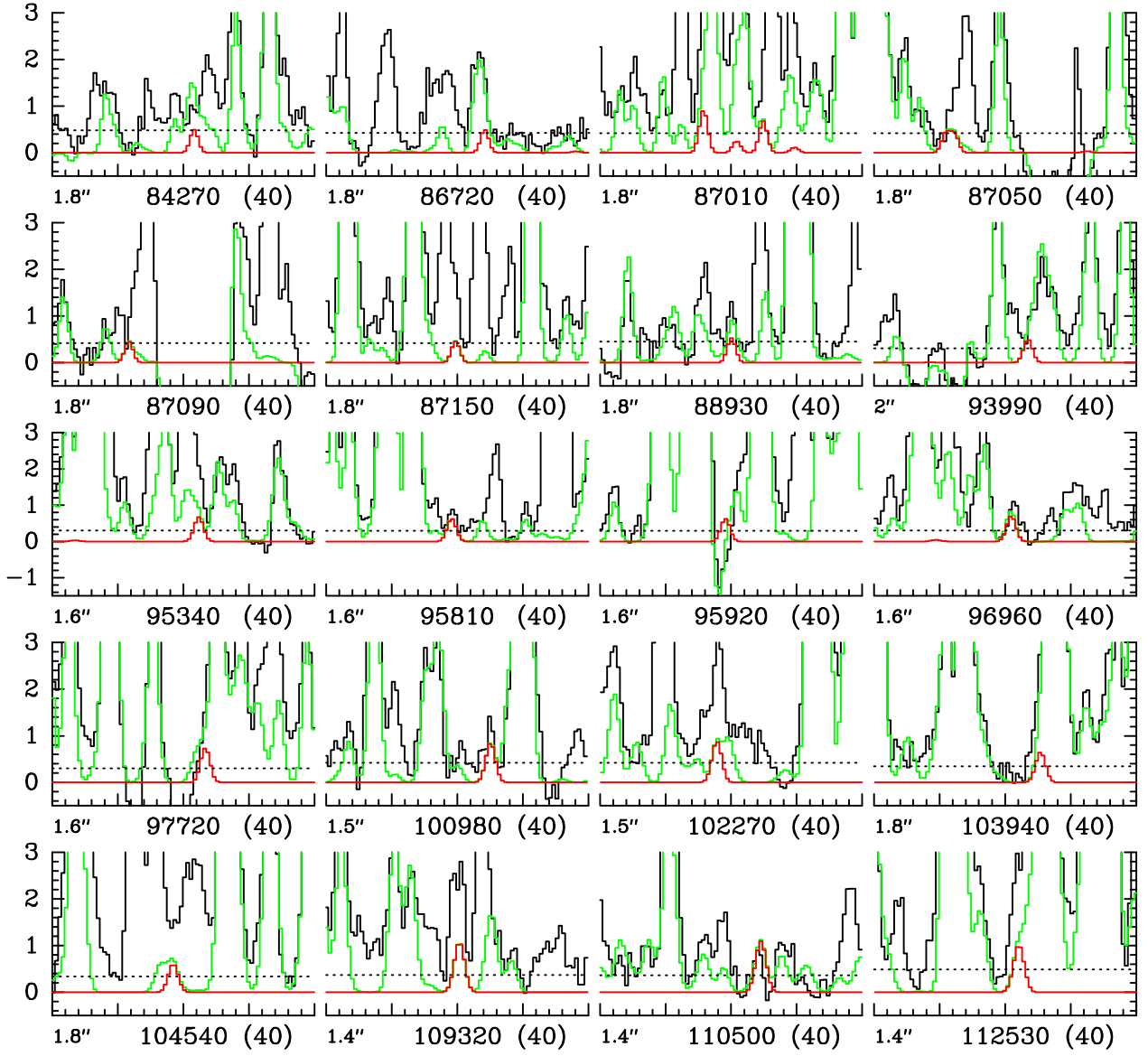


Fig. 12. Same as Fig. 1 for $\text{CH}_2\text{DCH}_2\text{CN}$ in its out-of-plane conformation.

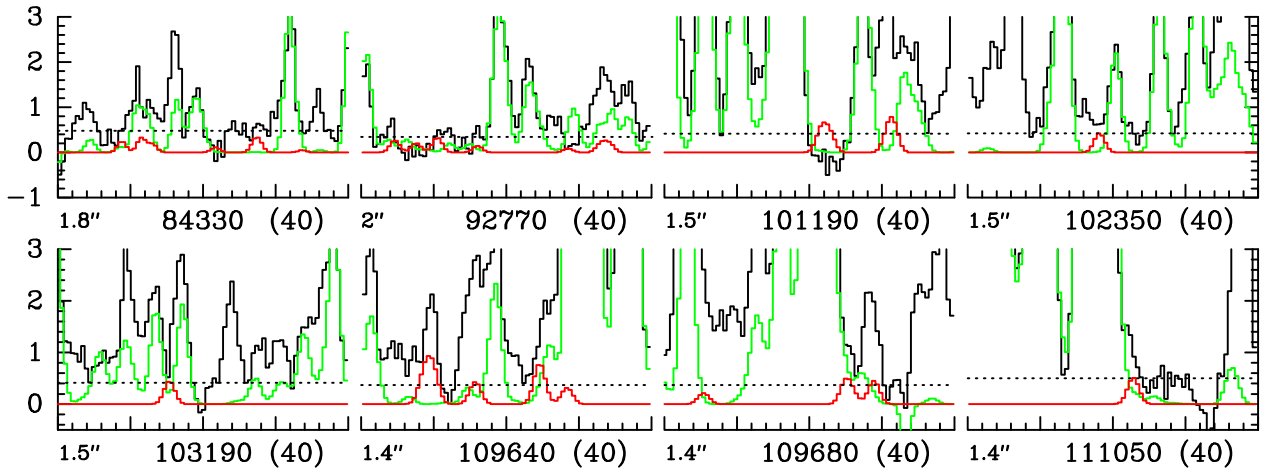


Fig. 13. Same as Fig. 1 for $\text{CH}_2\text{DCH}_2\text{CN}$ in its in-plane conformation. The full synthetic model (in green) does *not* contain any contribution of $\text{CH}_2\text{DCH}_2\text{CN}$ in its in-plane conformation (in red).

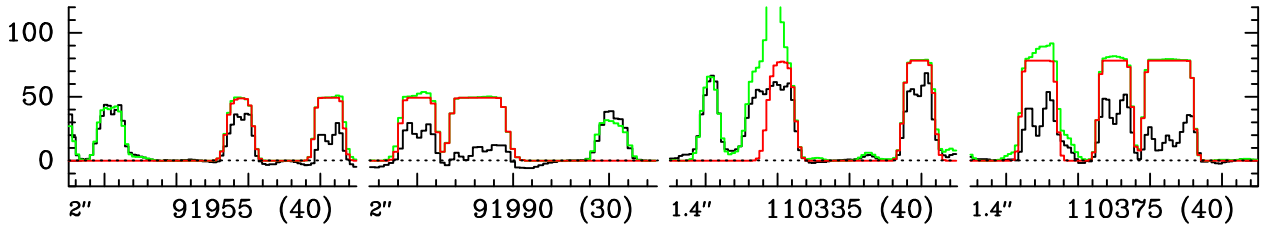


Fig. 14. Same as Fig. 1 for CH_3CN , $v = 0$.

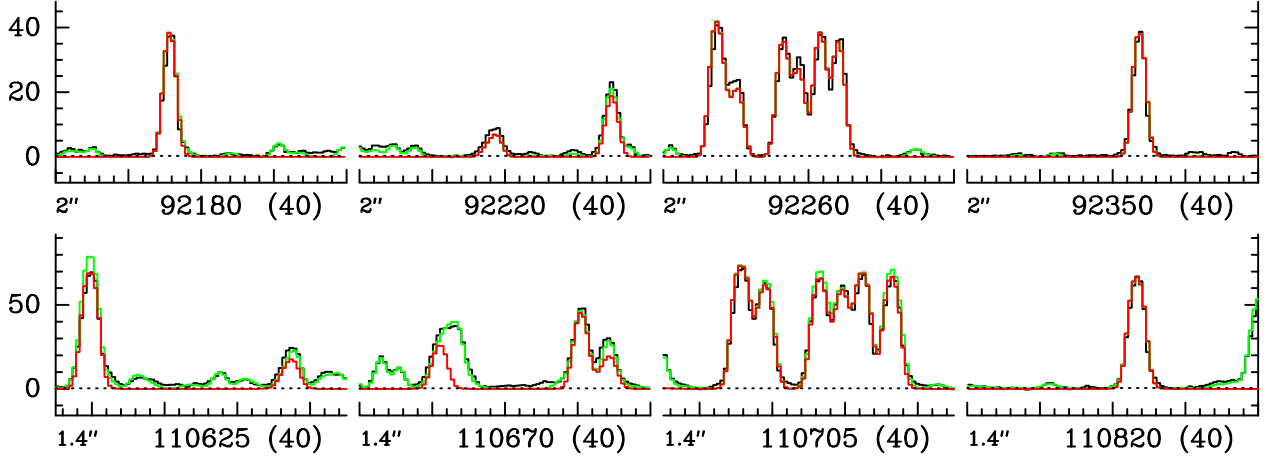


Fig. 15. Same as Fig. 1 for CH_3CN , $v_8 = 1$.

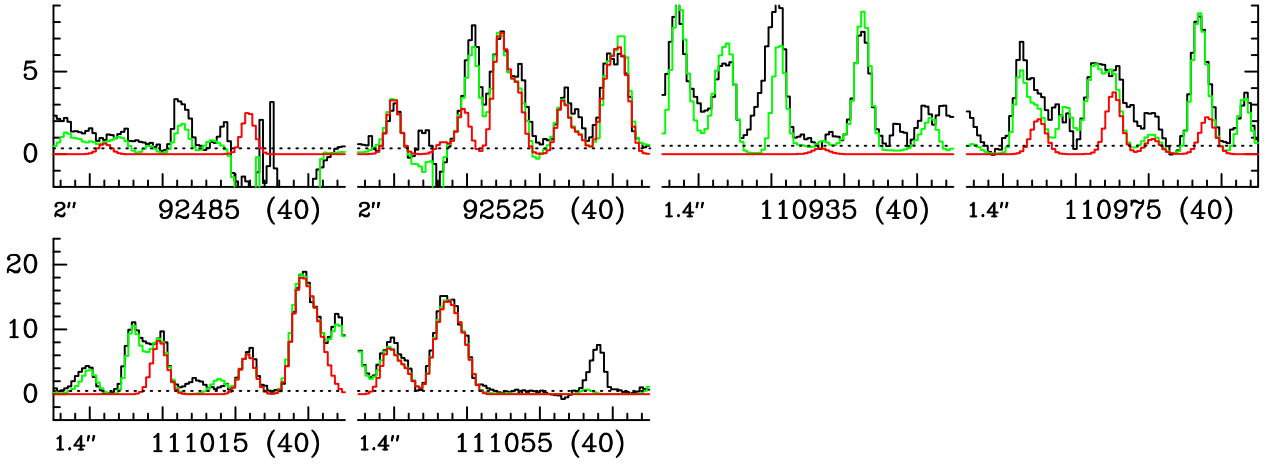


Fig. 16. Same as Fig. 1 for CH_3CN , $v_8 = 2$.

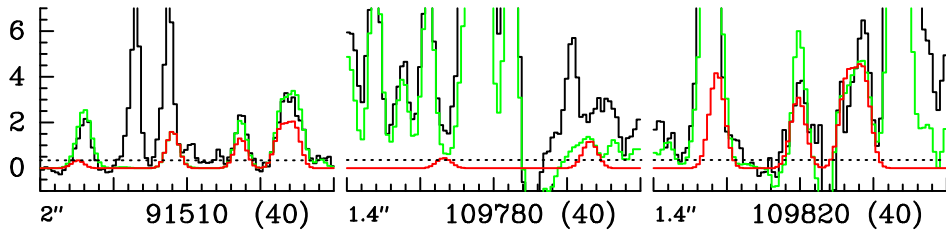


Fig. 17. Same as Fig. 1 for CH_3CN , $v_4 = 1$.

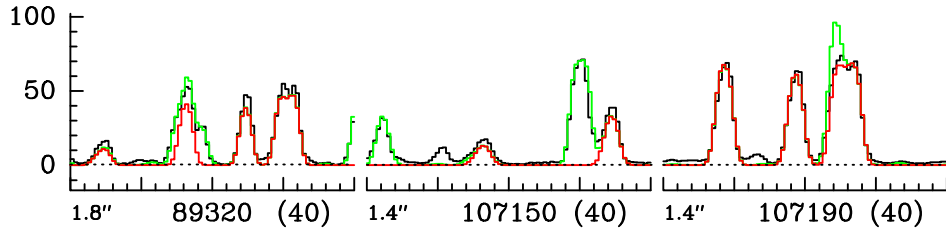


Fig. 18. Same as Fig. 1 for $^{13}\text{CH}_3\text{CN}$, $v = 0$.

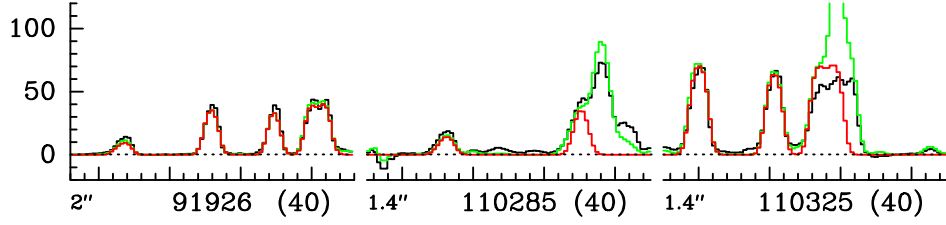


Fig. 19. Same as Fig. 1 for $\text{CH}_3^{13}\text{CN}$, $v = 0$.

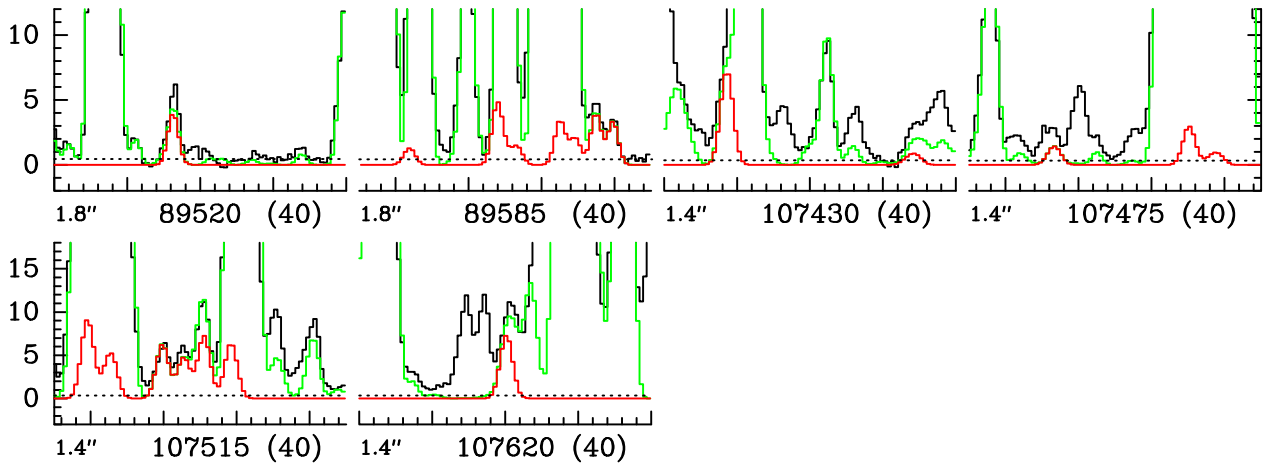


Fig. 20. Same as Fig. 1 for $^{13}\text{CH}_3\text{CN}$, $v_8 = 1$.

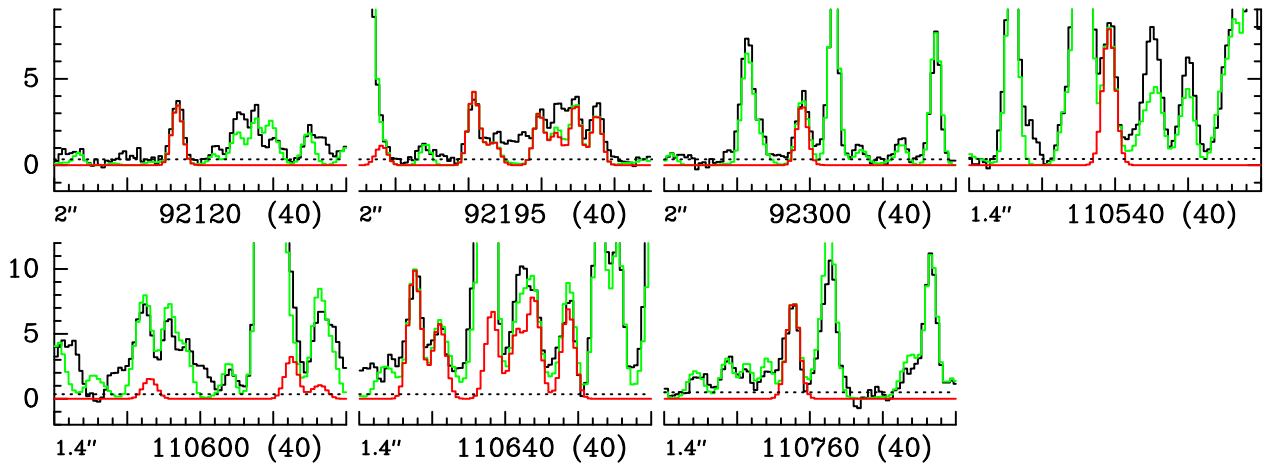


Fig. 21. Same as Fig. 1 for $\text{CH}_3^{13}\text{CN}$, $v_8 = 1$.

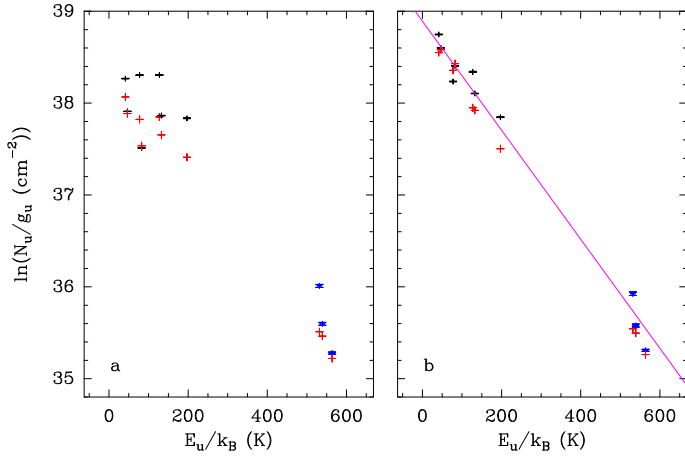


Fig. 22. Same as Fig. 6 for $^{13}\text{CH}_3\text{CN}$, $v = 0$ and $v_8 = 1$.

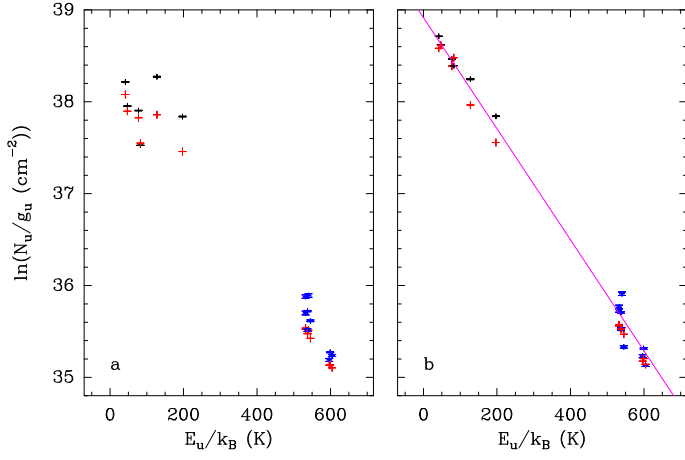


Fig. 23. Same as Fig. 6 for $\text{CH}_3^{13}\text{CN}$, $v = 0$ and $v_8 = 1$.

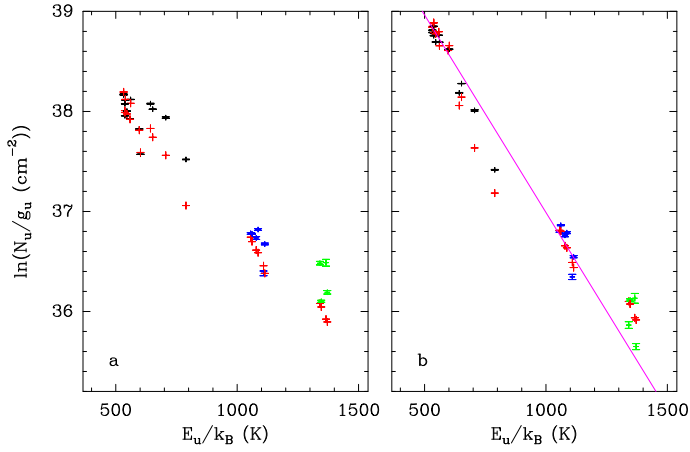


Fig. 24. Same as Fig. 6 for CH_3CN , $v_8 = 1$, $v_8 = 2$, and $v_4 = 1$.

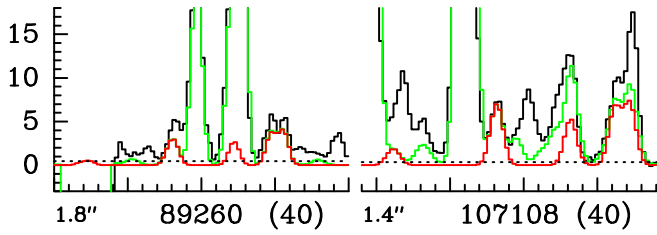


Fig. 25. Same as Fig. 1 for $^{13}\text{CH}_3^{13}\text{CN}$, $v = 0$.

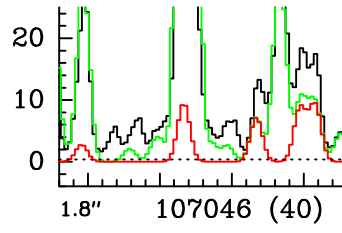


Fig. 26. Same as Fig. 1 for $\text{CH}_3\text{C}^{15}\text{N}$, $v = 0$.

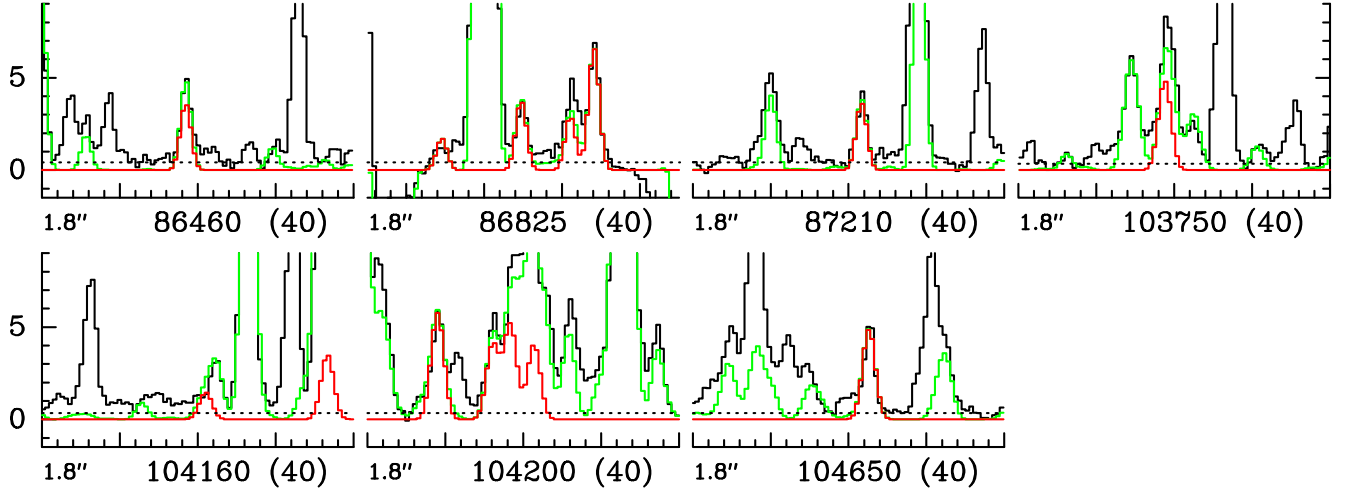


Fig. 27. Same as Fig. 1 for CH_2DCN , $v = 0$.

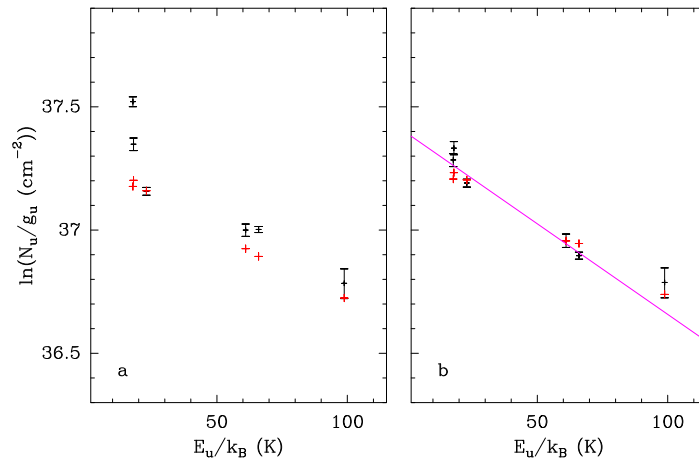


Fig. 28. Same as Fig. 6 for CH_2DCN .

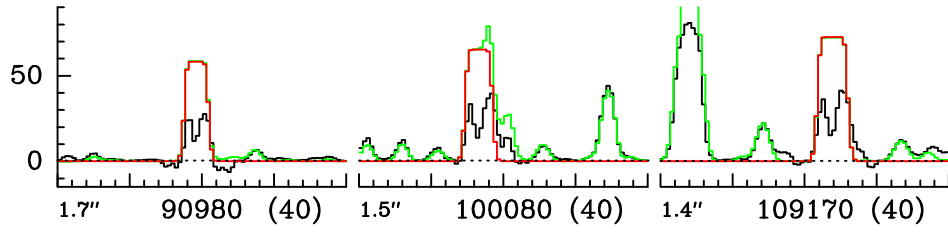


Fig. 29. Same as Fig. 1 for HC_3N , $v = 0$.

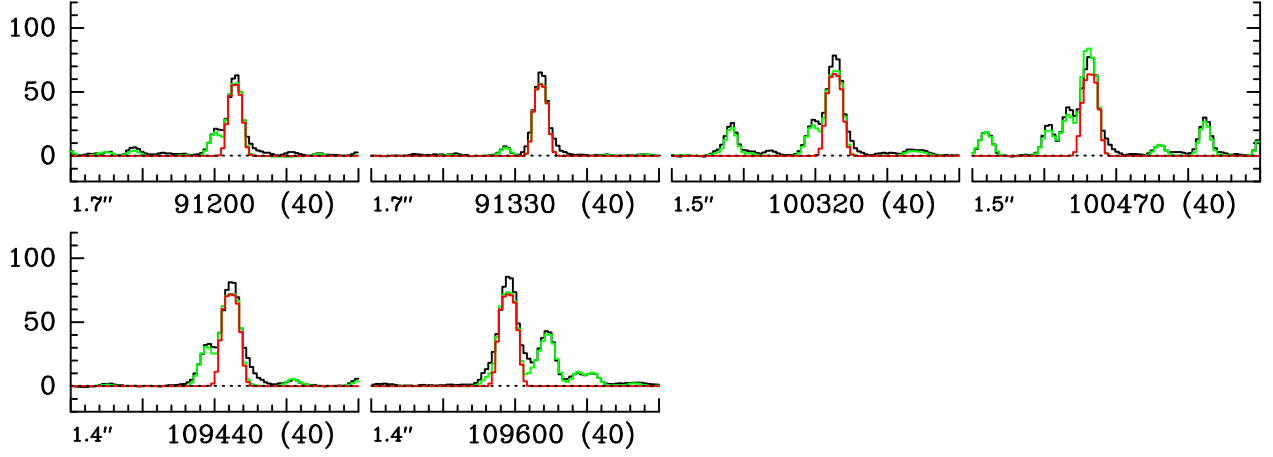


Fig. 30. Same as Fig. 1 for HC_3N , $v_7 = 1$.

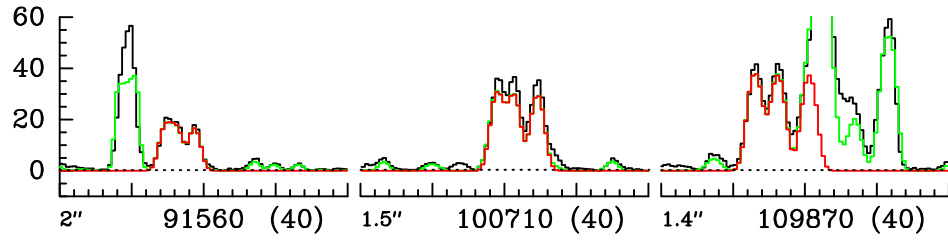


Fig. 31. Same as Fig. 1 for HC_3N , $v_7 = 2$.

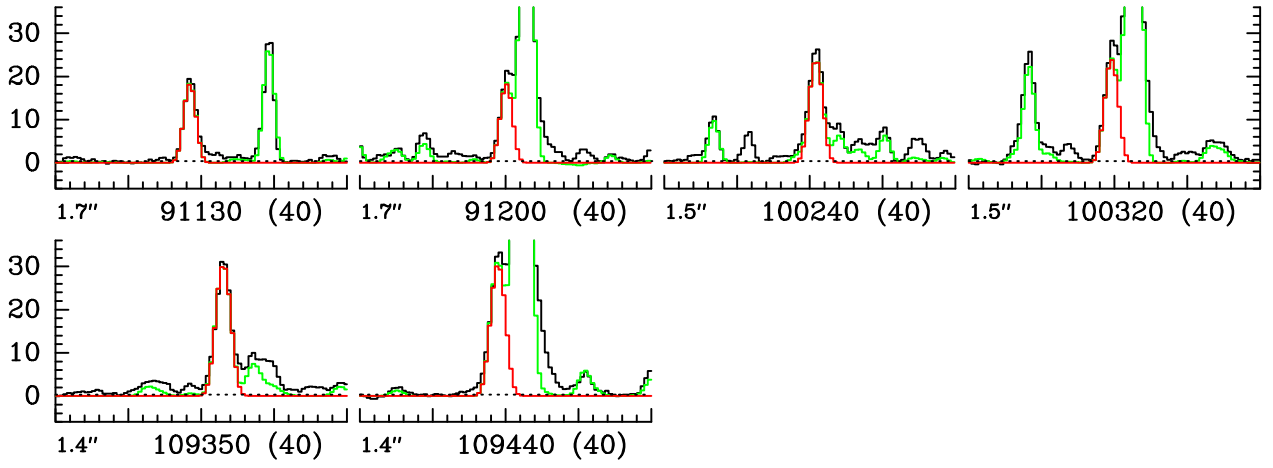


Fig. 32. Same as Fig. 1 for HC_3N , $v_6 = 1$.

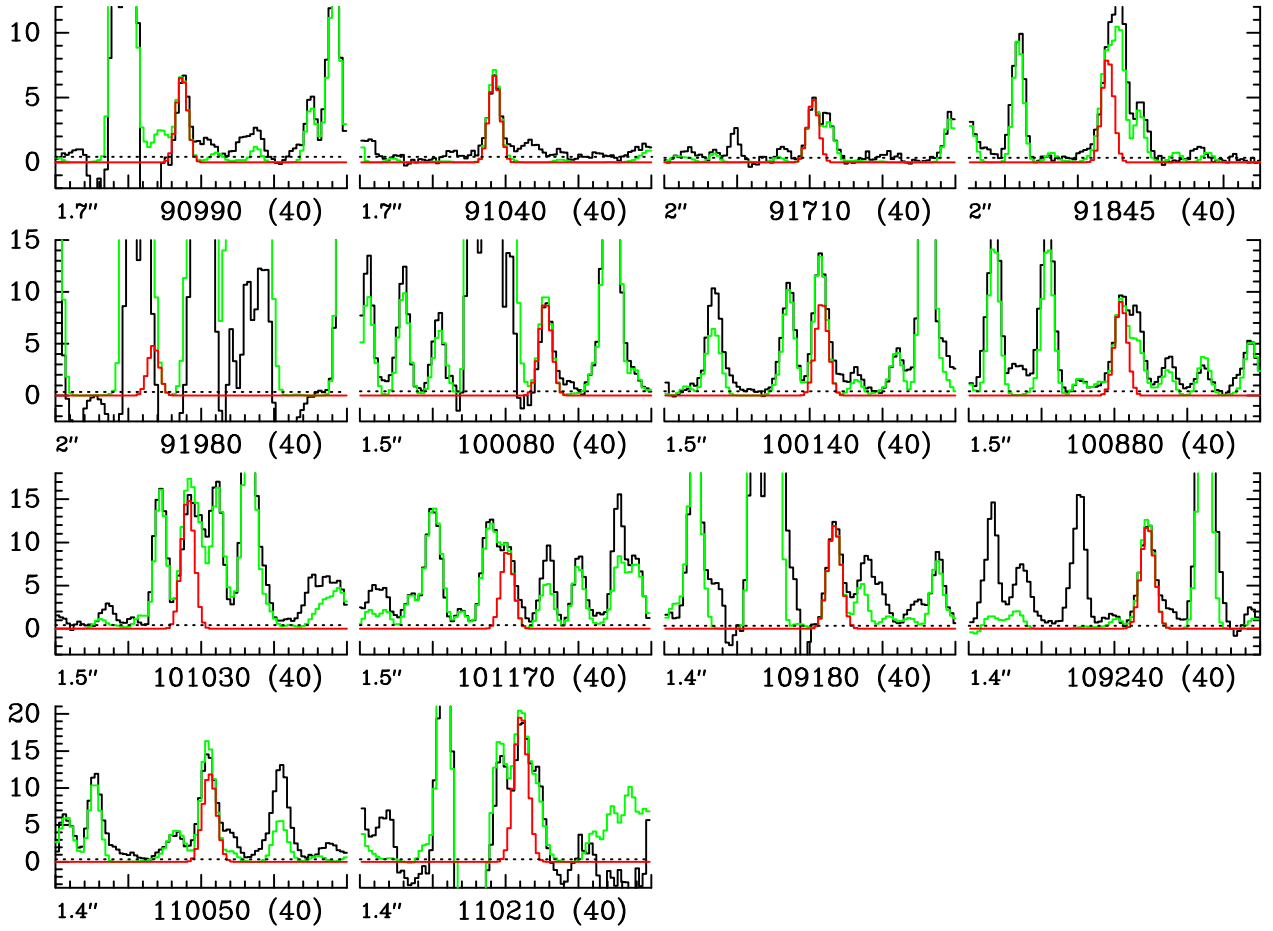


Fig. 33. Same as Fig. 1 for HC_3N , $v_5 = 1$ and $v_7 = 3$.

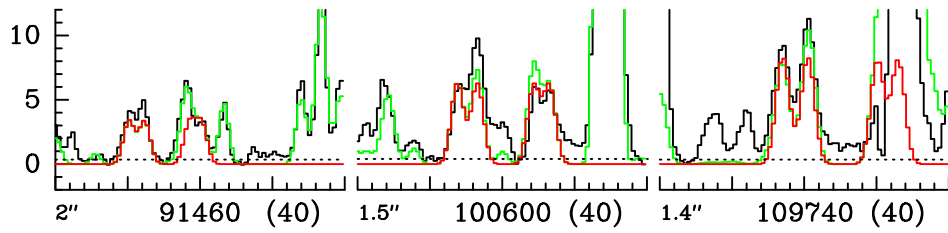


Fig. 34. Same as Fig. 1 for HC_3N , $v_6 = v_7 = 1$.

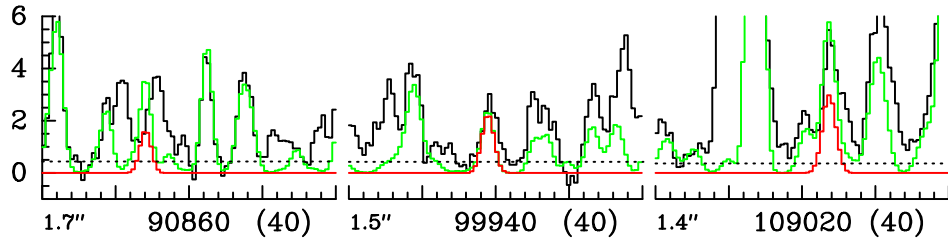


Fig. 35. Same as Fig. 1 for HC_3N , $v_4 = 1$.

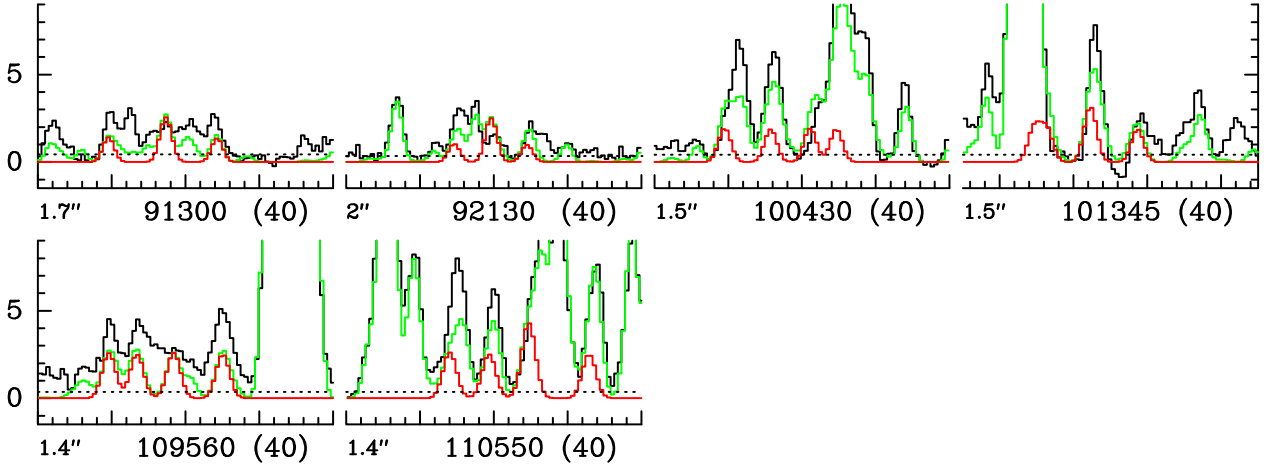


Fig. 36. Same as Fig. 1 for HC_3N , $v_7 = 4$ and $v_5 = v_7 = 1$.

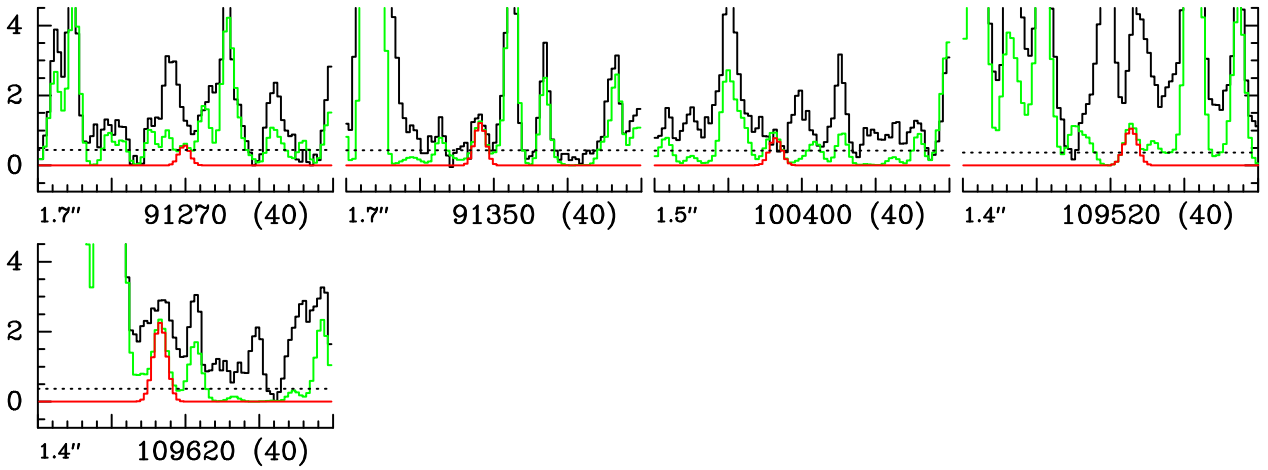


Fig. 37. Same as Fig. 1 for HC_3N , $v_6 = 2$.

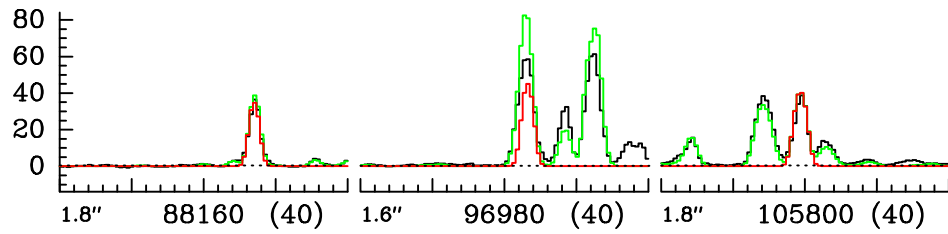


Fig. 38. Same as Fig. 1 for H^{13}CCCN , $v = 0$.

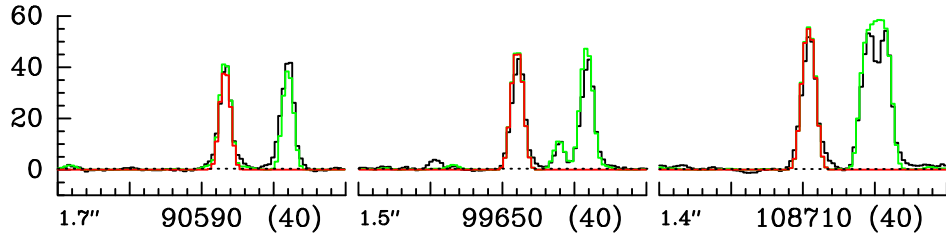


Fig. 39. Same as Fig. 1 for HC^{13}CCN , $v = 0$.

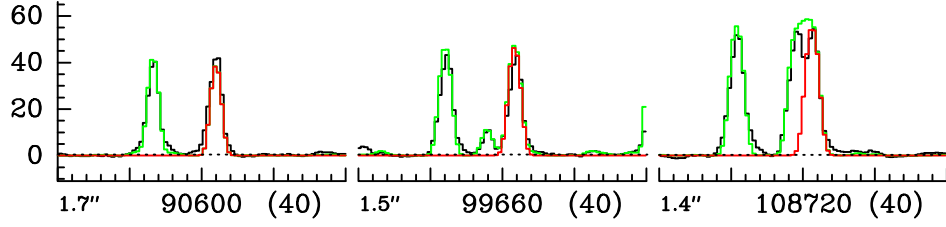


Fig. 40. Same as Fig. 1 for HCC^{13}CN , $v = 0$.

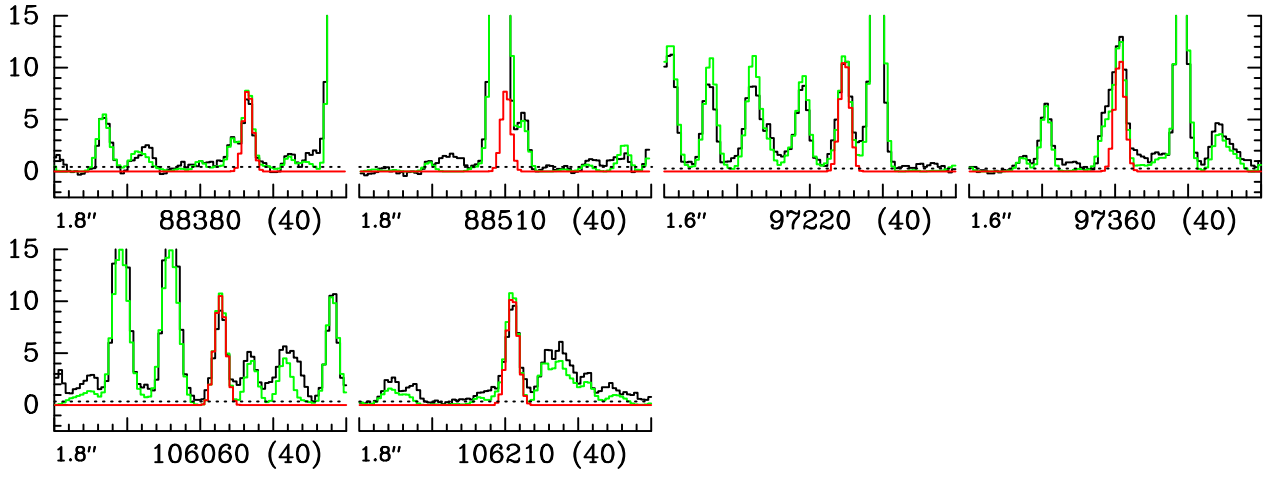


Fig. 41. Same as Fig. 1 for H^{13}CCCN , $v_7 = 1$.

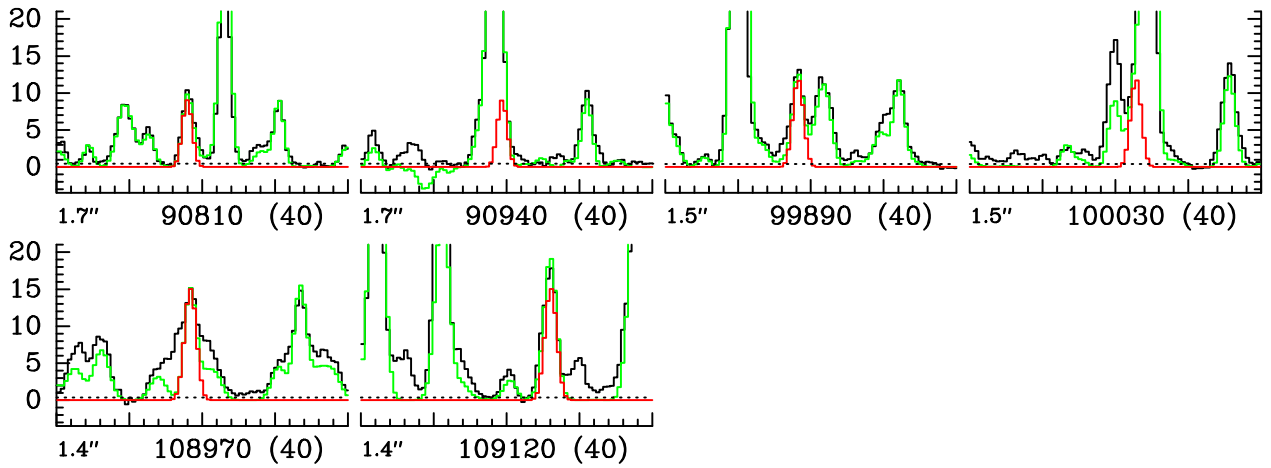


Fig. 42. Same as Fig. 1 for HC^{13}CCN , $v_7 = 1$.

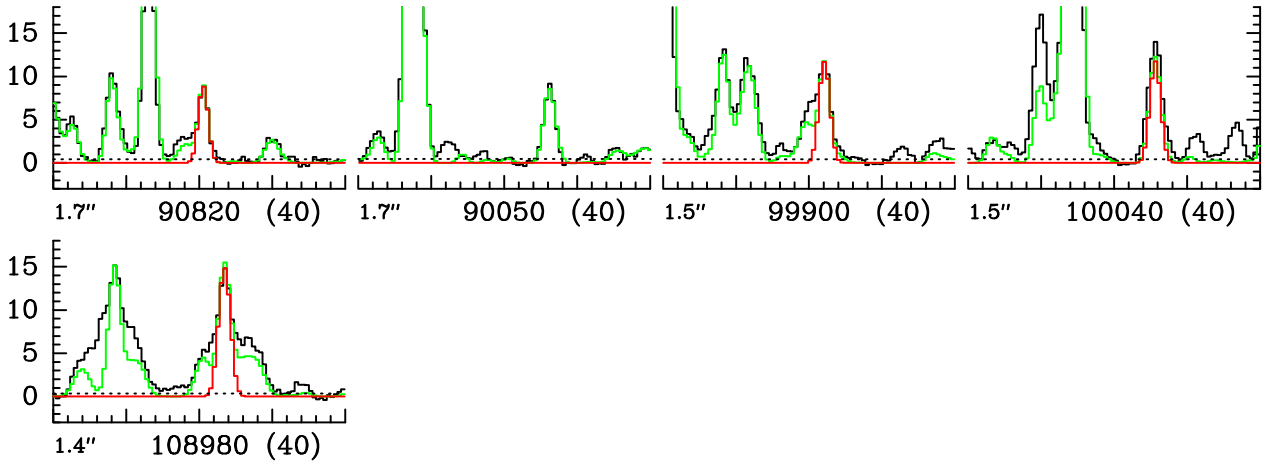


Fig. 43. Same as Fig. 1 for HCC^{13}CN , $v_7 = 1$.

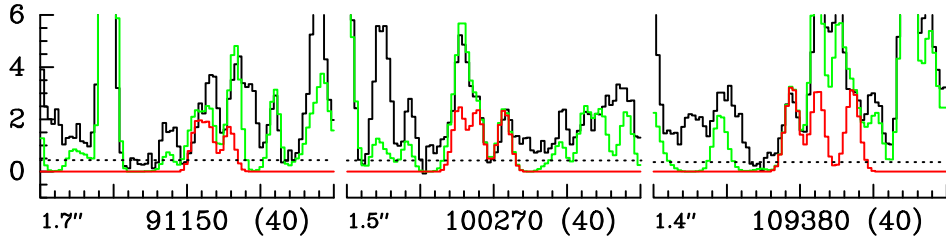


Fig. 44. Same as Fig. 1 for HC^{13}CCN , $v_7 = 2$.

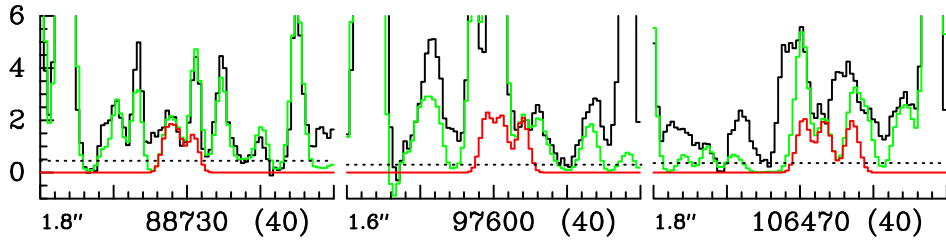


Fig. 45. Same as Fig. 1 for H^{13}CCCN , $v_7 = 2$.

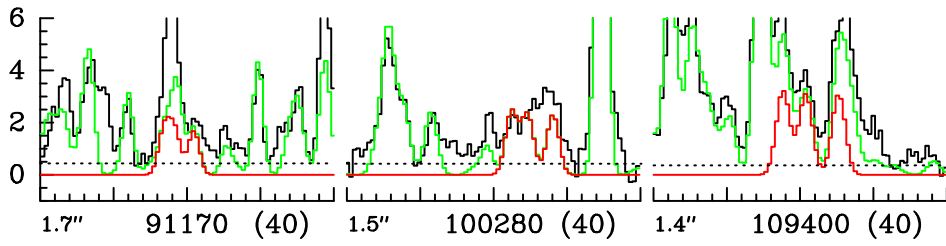


Fig. 46. Same as Fig. 1 for HCC^{13}CN , $v_7 = 2$.

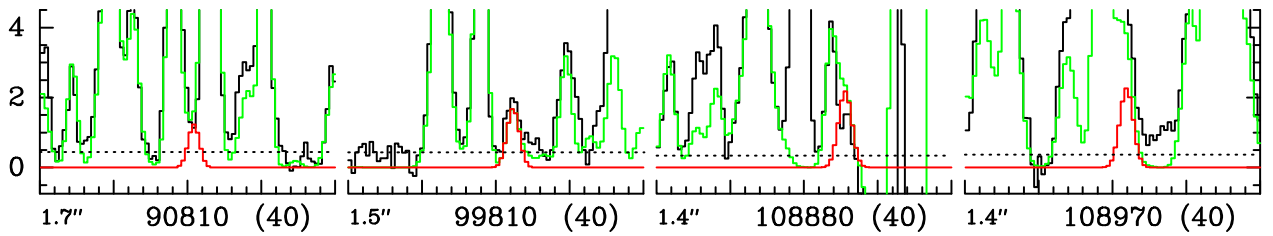


Fig. 47. Same as Fig. 1 for HC^{13}CCN , $v_6 = 1$.

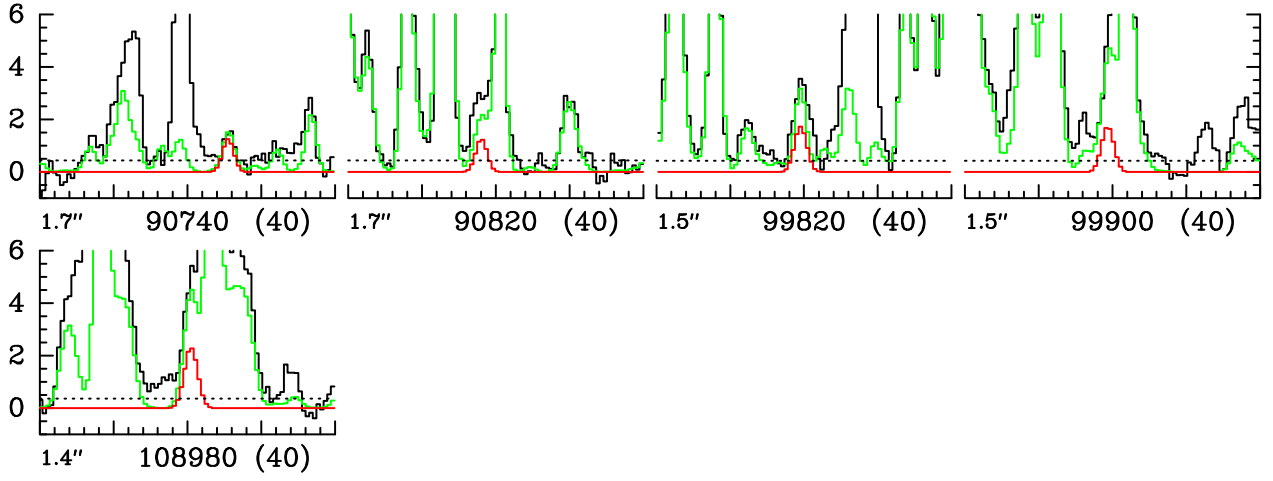


Fig. 48. Same as Fig. 1 for HCC^{13}CN , $v_6 = 1$.

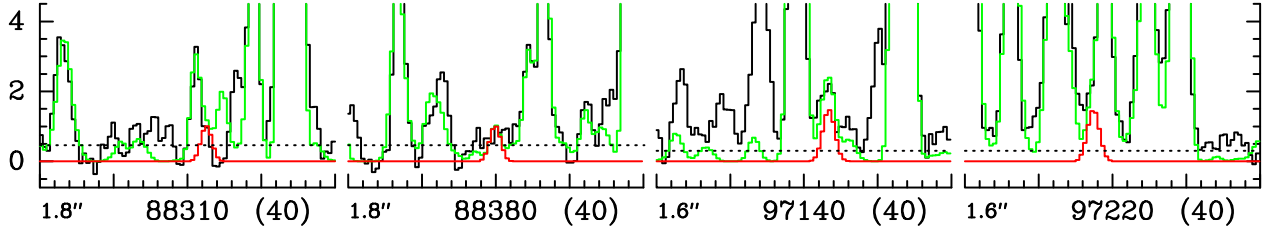


Fig. 49. Same as Fig. 1 for H^{13}CCCN , $v_6 = 1$.

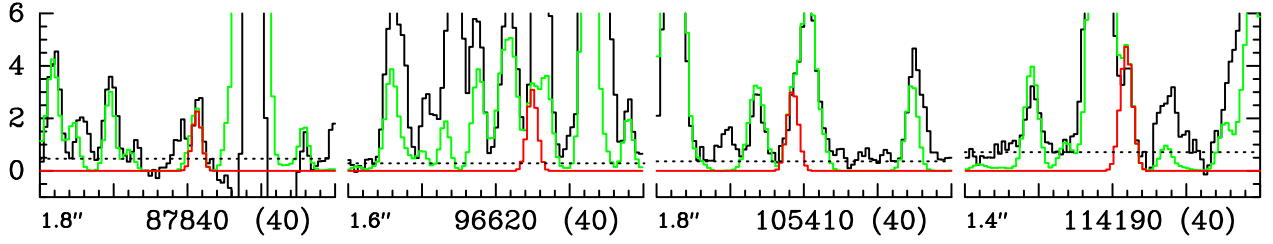


Fig. 50. Same as Fig. 1 for $\text{H}^{13}\text{C}^{13}\text{CN}$, $v = 0$.

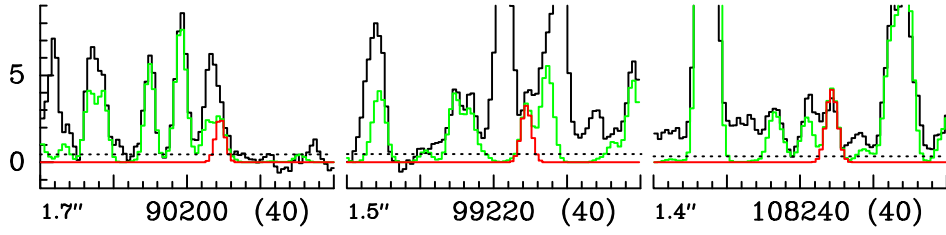


Fig. 51. Same as Fig. 1 for $\text{HC}^{13}\text{C}^{13}\text{CN}$, $v = 0$.

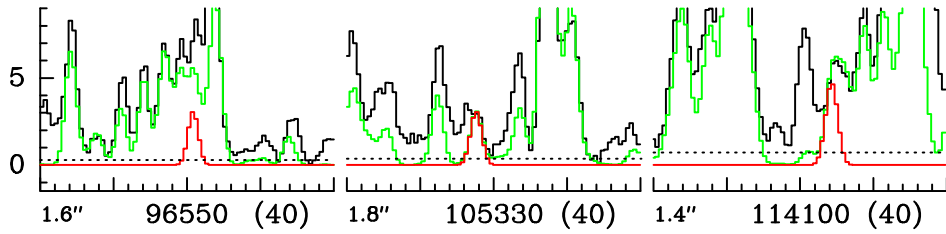


Fig. 52. Same as Fig. 1 for $\text{H}^{13}\text{CC}^{13}\text{CN}$, $v = 0$.

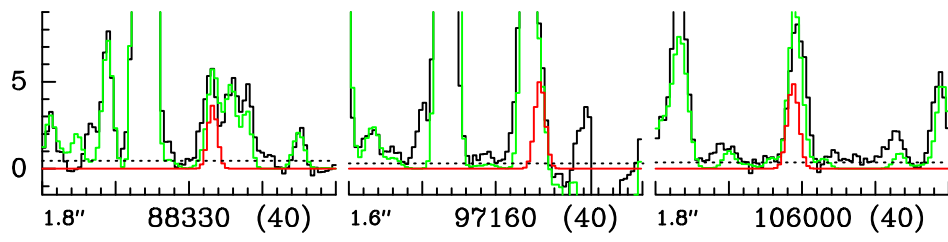


Fig. 53. Same as Fig. 1 for HC_3^{15}N , $v = 0$.

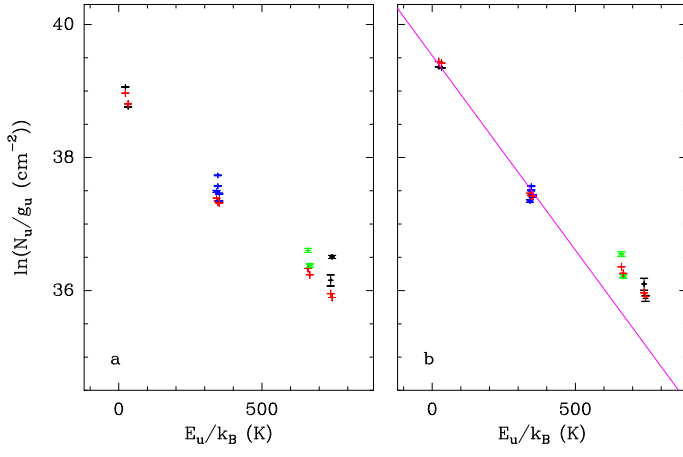


Fig. 54. Same as Fig. 6 for H^{13}CCCN , $v=0$, $v_7=1$, $v_7=2$, and $v_6=1$.

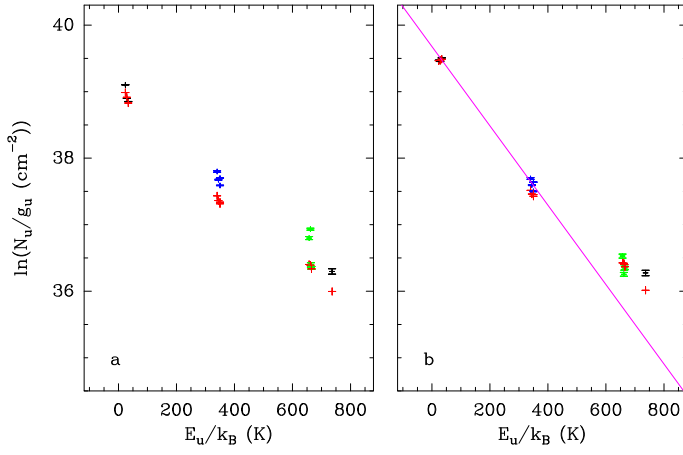


Fig. 55. Same as Fig. 6 for HC^{13}CCN , $v=0$, $v_7=1$, $v_7=2$, and $v_6=1$.

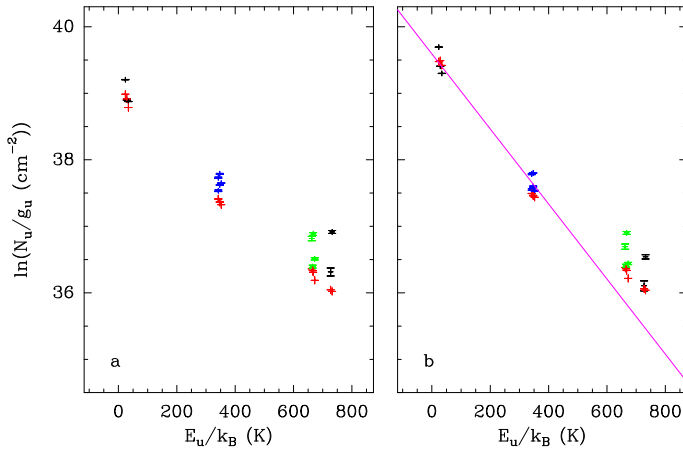


Fig. 56. Same as Fig. 6 for HCC^{13}CN , $v=0$, $v_7=1$, $v_7=2$, and $v_6=1$.

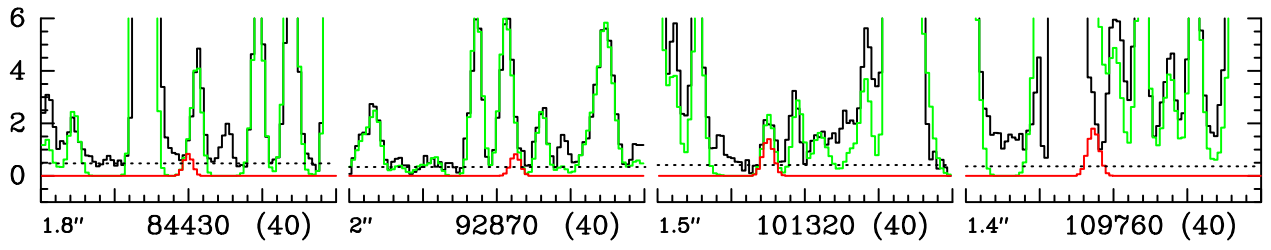


Fig. 57. Same as Fig. 1 for DC_3N , $v = 0$.

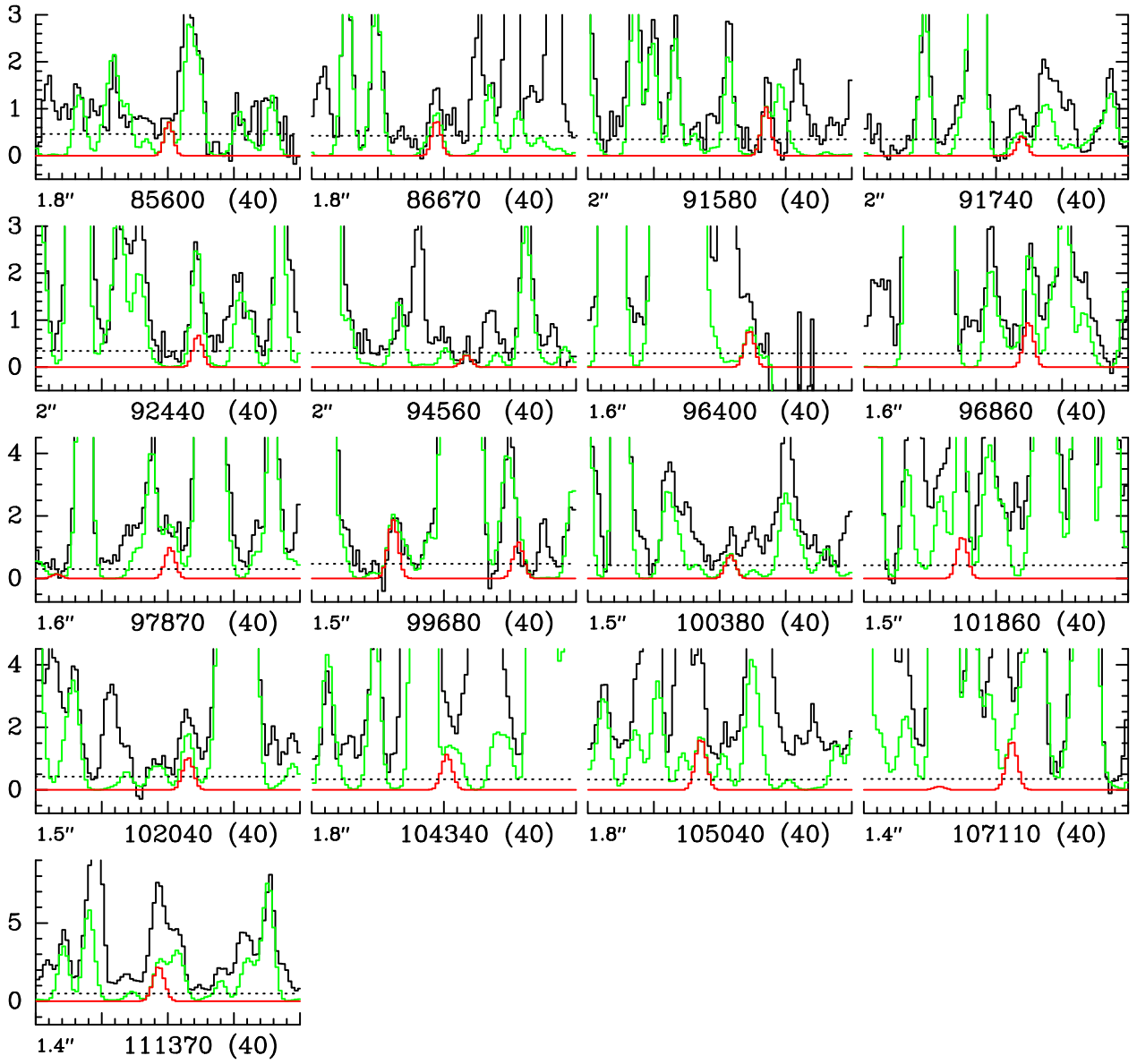


Fig. 58. Same as Fig. 1 for CH_2DOH , $v = 0$.

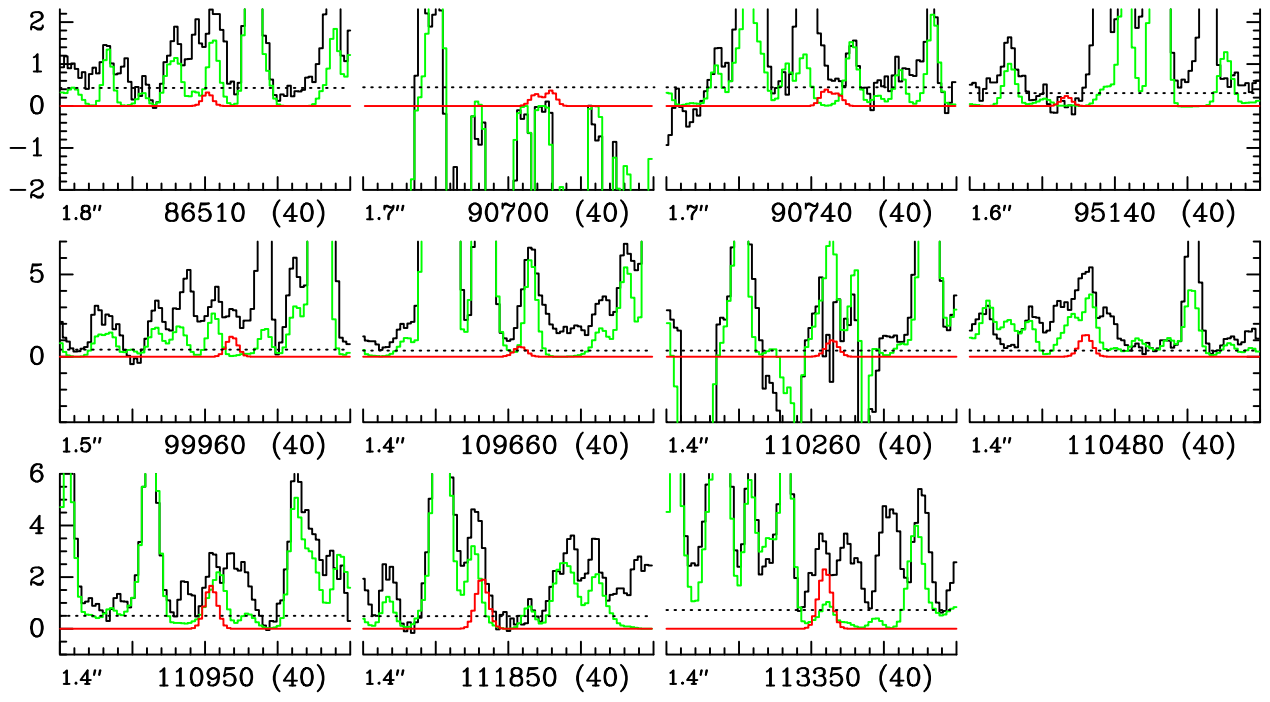


Fig. 59. Same as Fig. 1 for CH_3OD , $v = 0$. The full synthetic model (in green) does *not* contain any contribution of CH_3OD (in red).

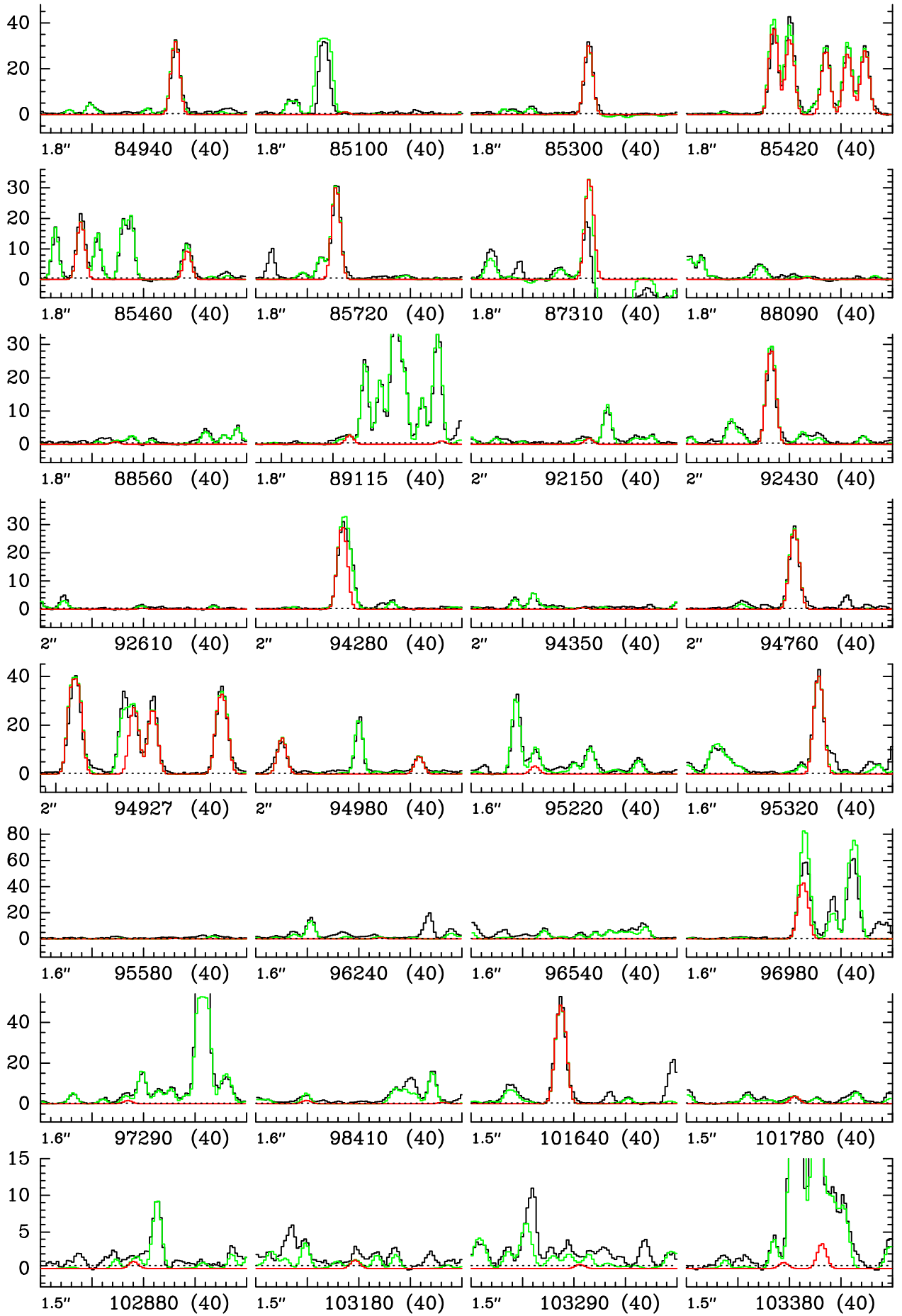


Fig. 60. Same as Fig. 1 for $\text{C}_2\text{H}_3\text{CN}$, $v = 0$.

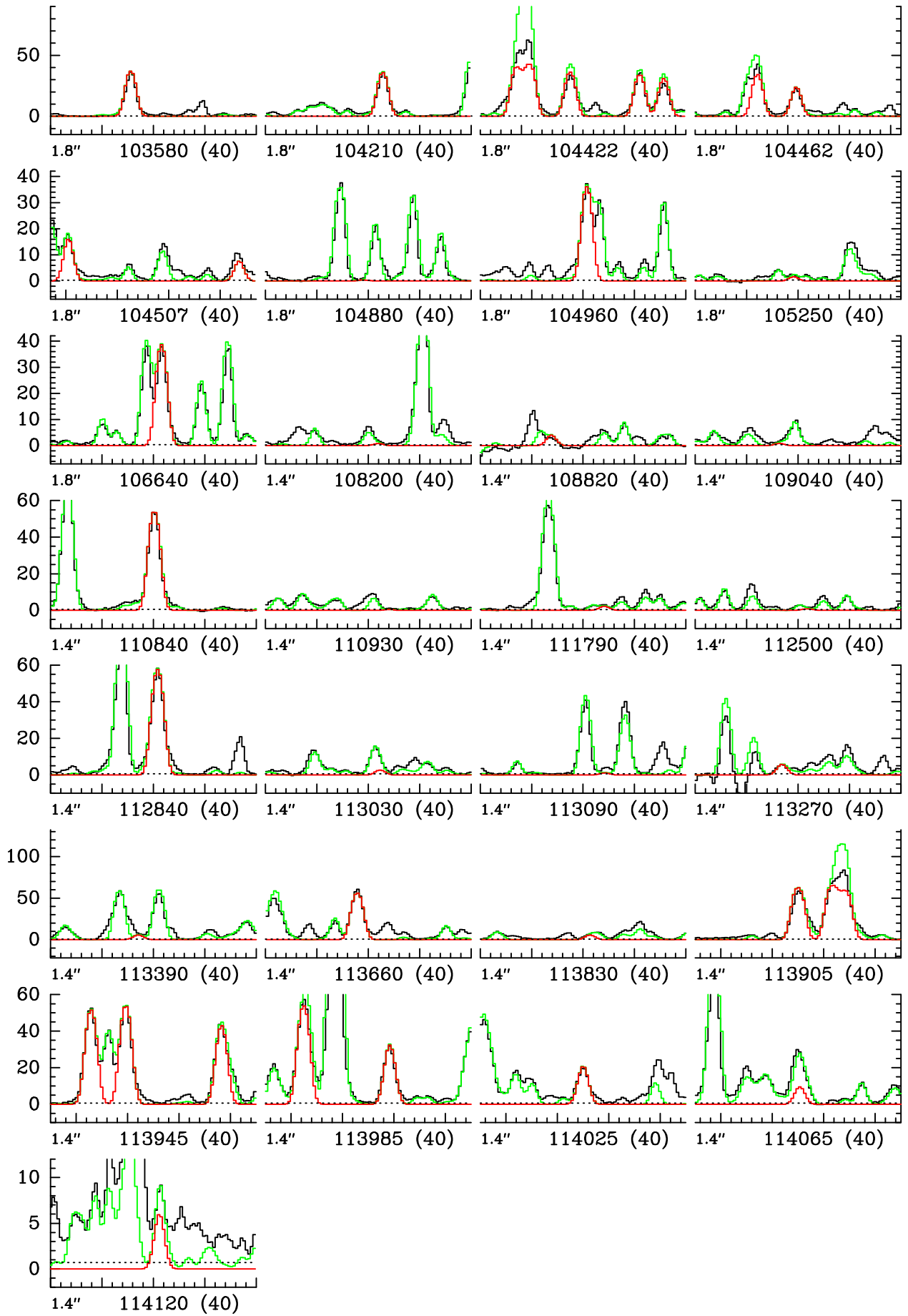


Fig. 60. continued.

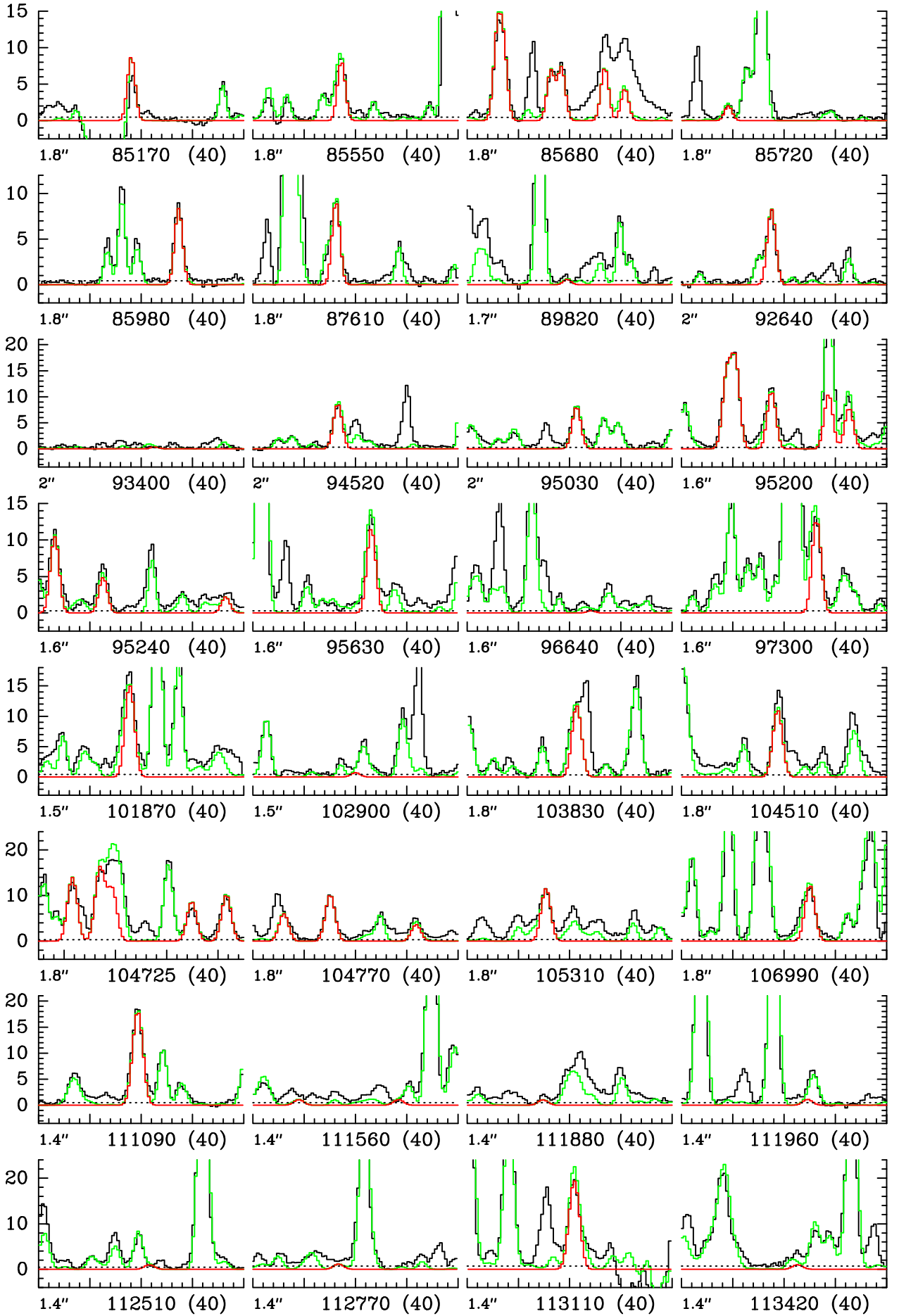


Fig. 61. Same as Fig. 1 for $\text{C}_2\text{H}_3\text{CN}$, $v_{11} = 1$.

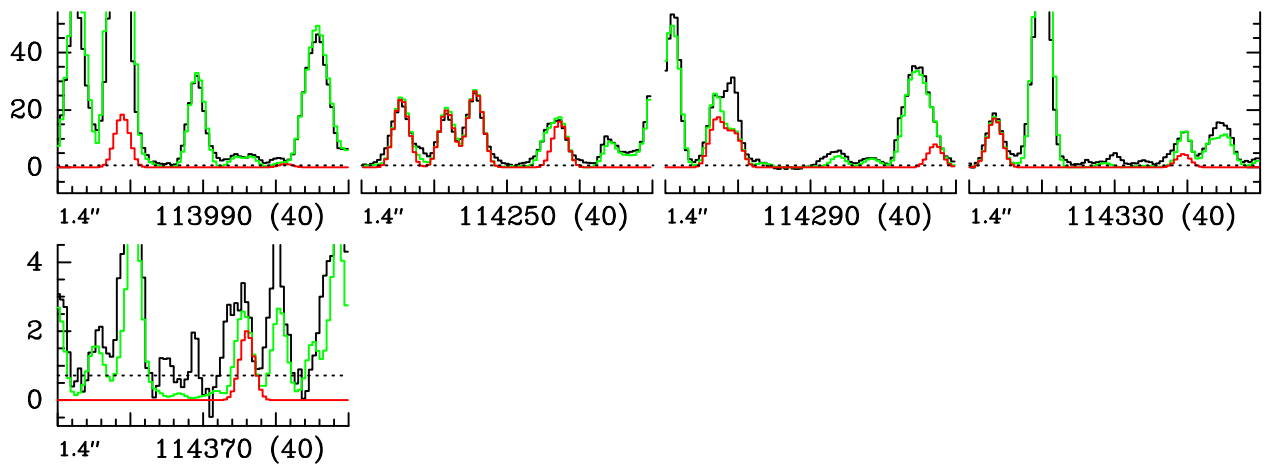


Fig. 61. continued.

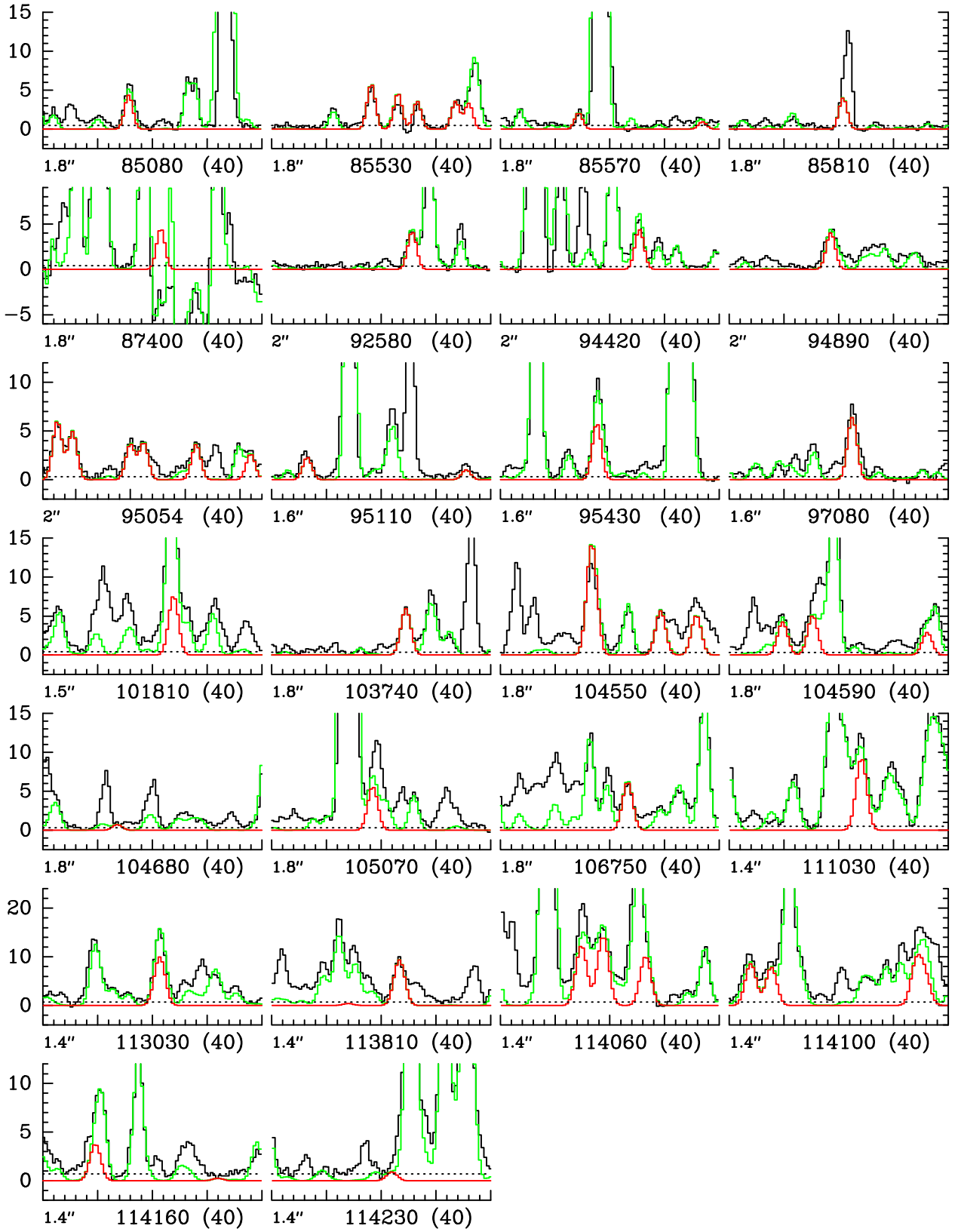


Fig. 62. Same as Fig. 1 for $\text{C}_2\text{H}_3\text{CN}$, $v_{15} = 1$.

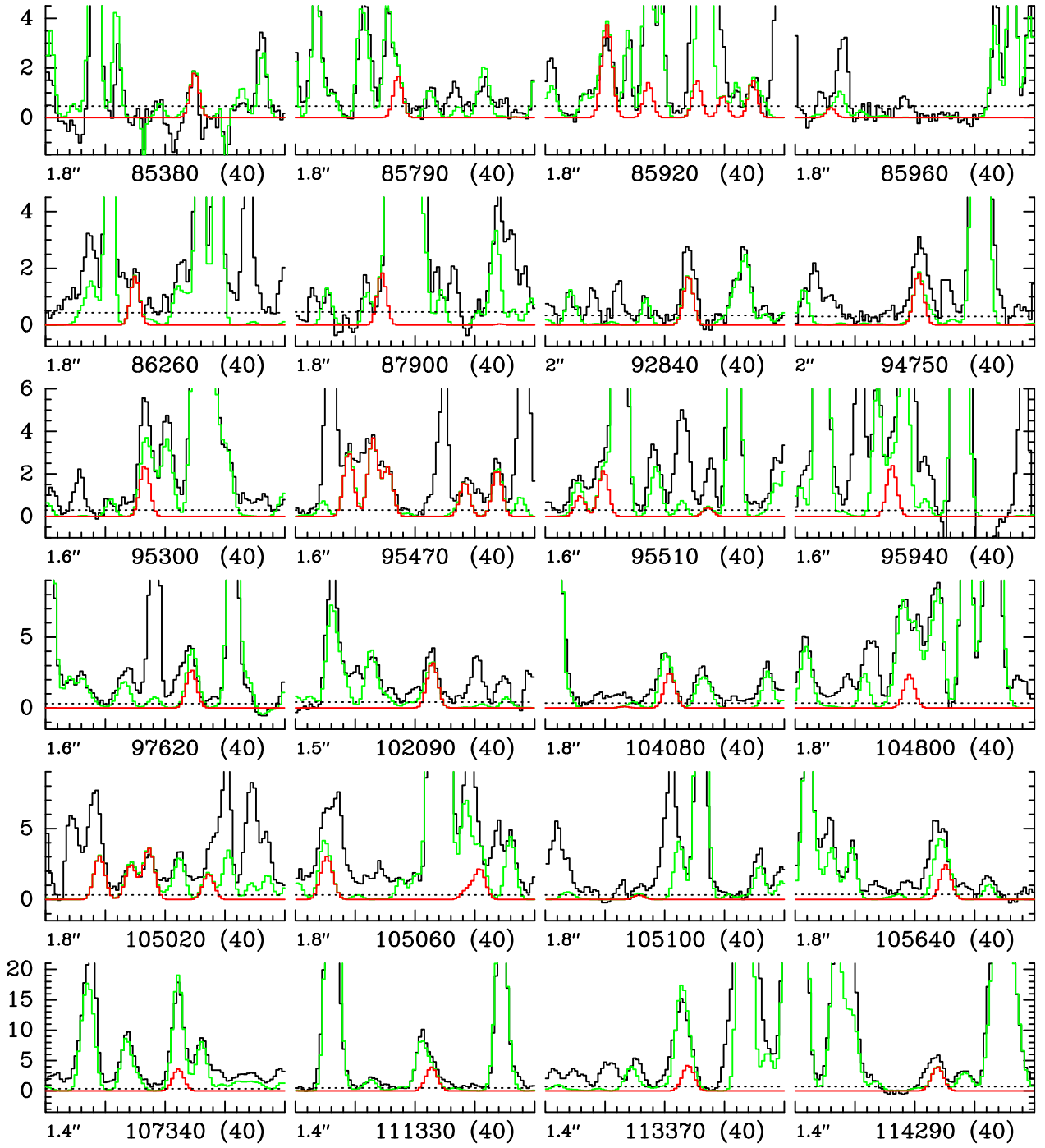


Fig. 63. Same as Fig. 1 for $\text{C}_2\text{H}_3\text{CN}$, $v_{11} = 2$.

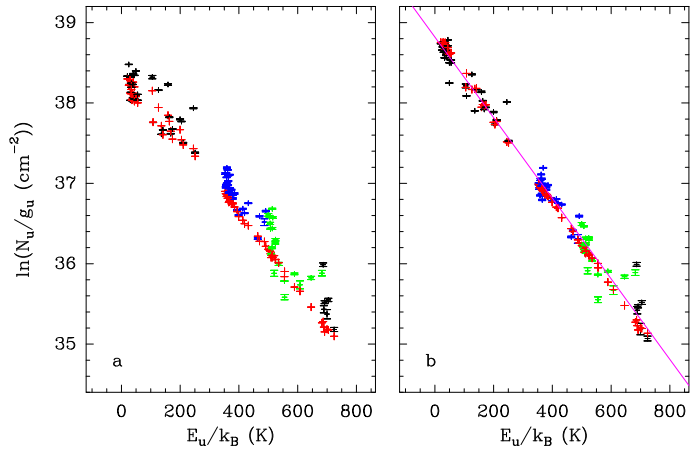


Fig. 64. Same as Fig. 6 for $\text{C}_2\text{H}_3\text{CN}$, $v = 0$, $v_{11} = 1$, $v_{15} = 1$, and $v_{11} = 2$.

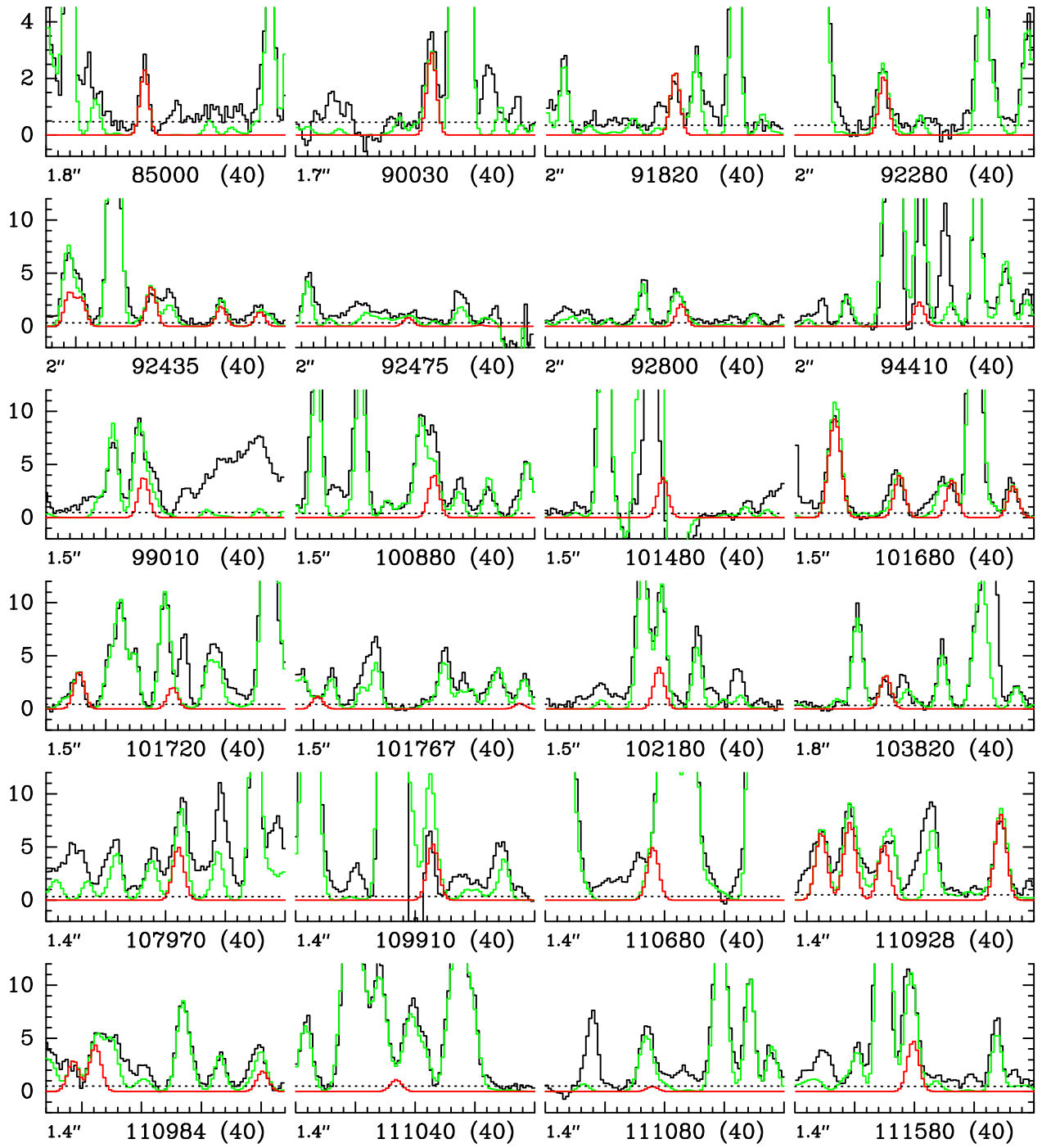


Fig. 65. Same as Fig. 1 for $^{13}\text{CH}_2\text{CHCN}$, $v = 0$.

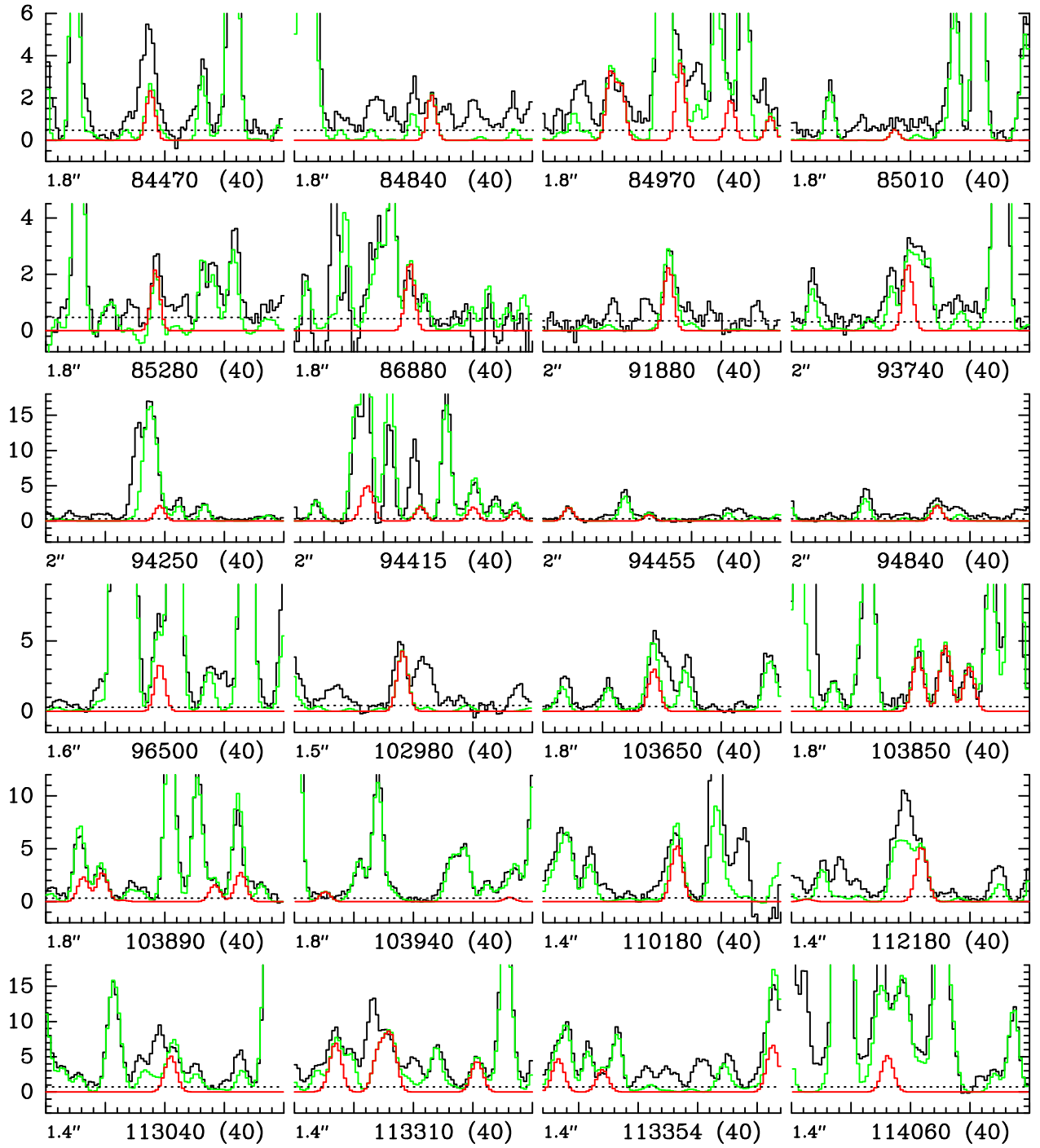


Fig. 66. Same as Fig. 1 for $\text{CH}_2^{13}\text{CHCN}$, $v = 0$.

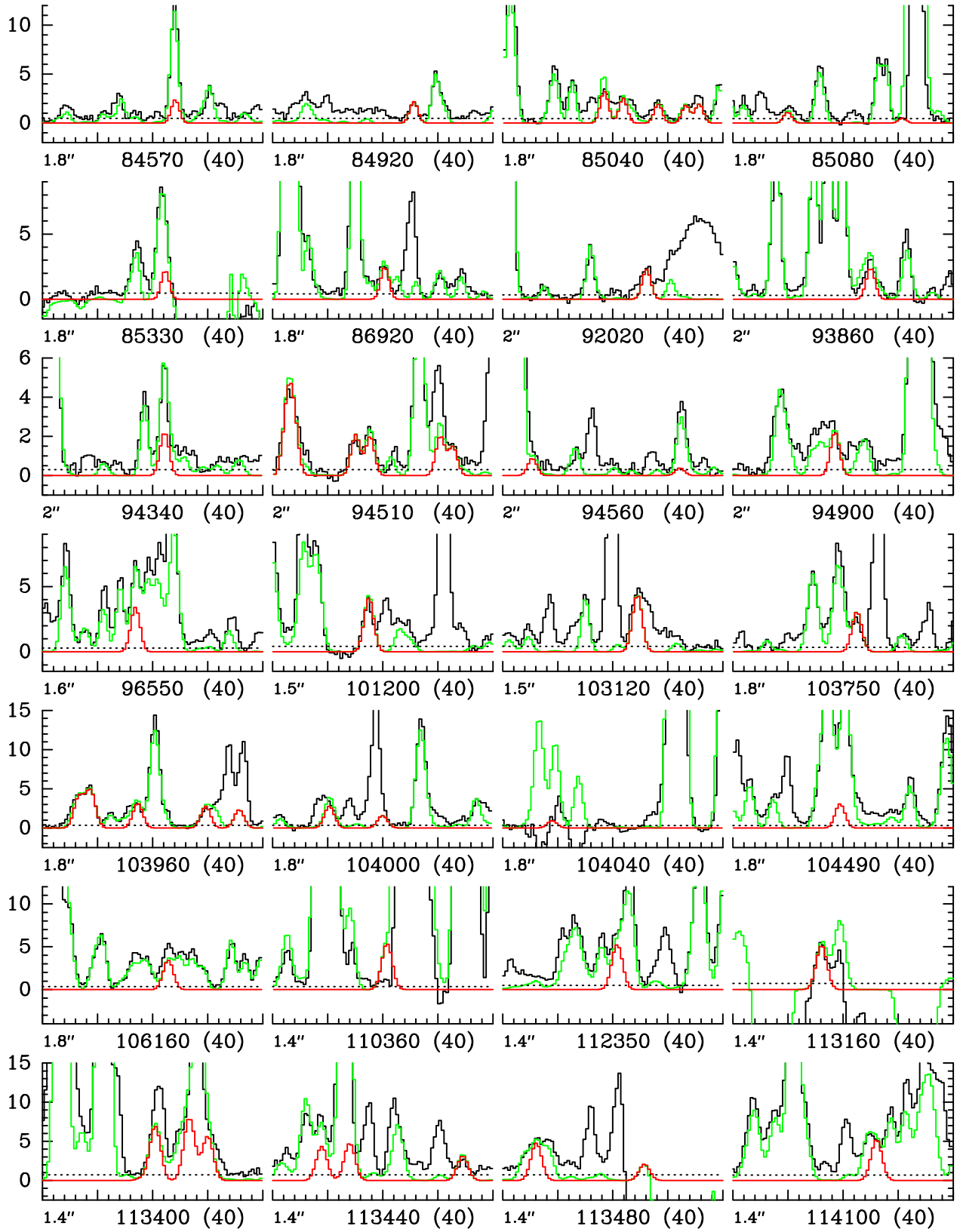


Fig. 67. Same as Fig. 1 for $\text{C}_2\text{H}_3^{13}\text{CN}$, $v = 0$.

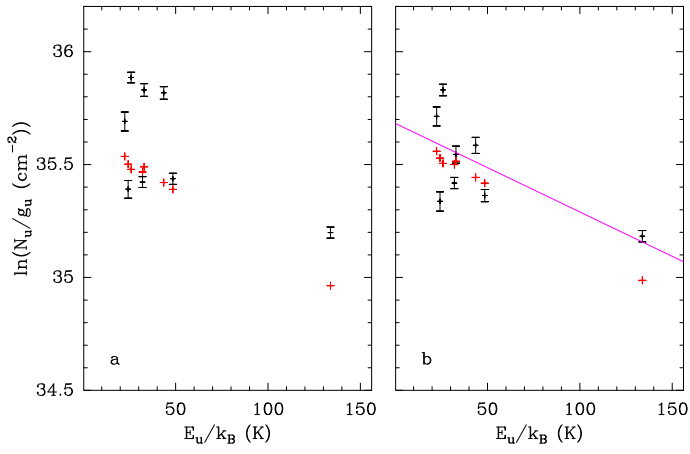


Fig. 68. Same as Fig. 6 for $^{13}\text{CH}_2\text{CHCN}$, $v=0$.

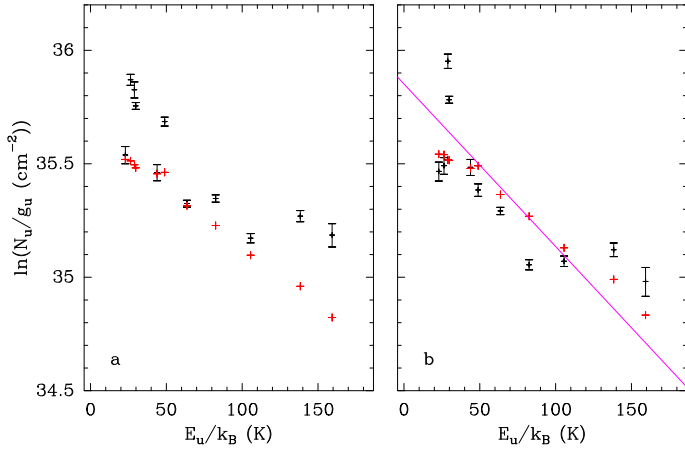


Fig. 69. Same as Fig. 6 for $\text{CH}_2^{13}\text{CHCN}$, $v=0$.

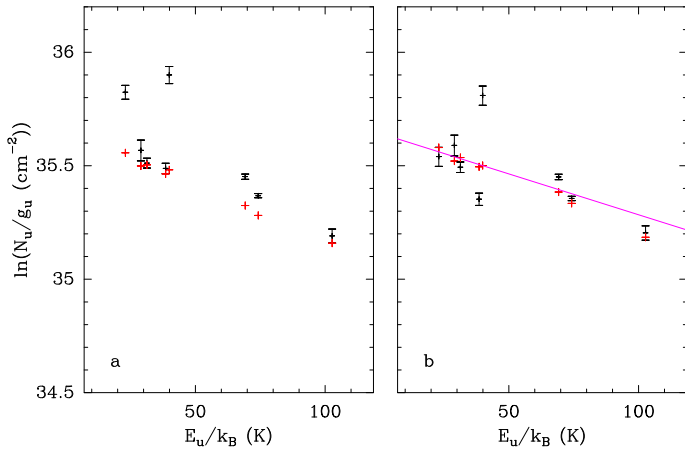


Fig. 70. Same as Fig. 6 for $\text{CH}_2\text{CH}^{13}\text{CN}$, $v=0$.

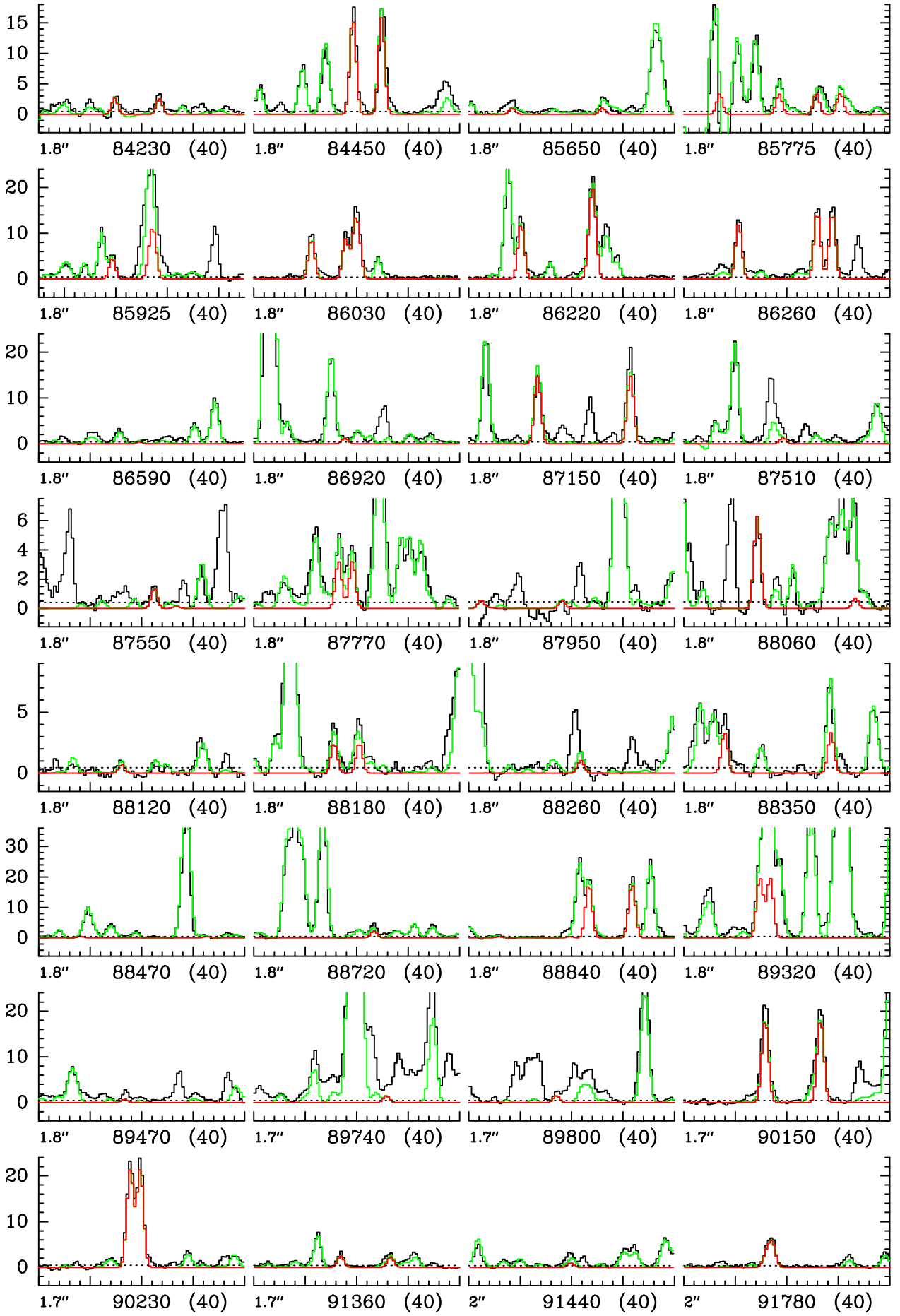


Fig. 71. Same as Fig. 1 for CH_3OCHO , $v_t = 0$.

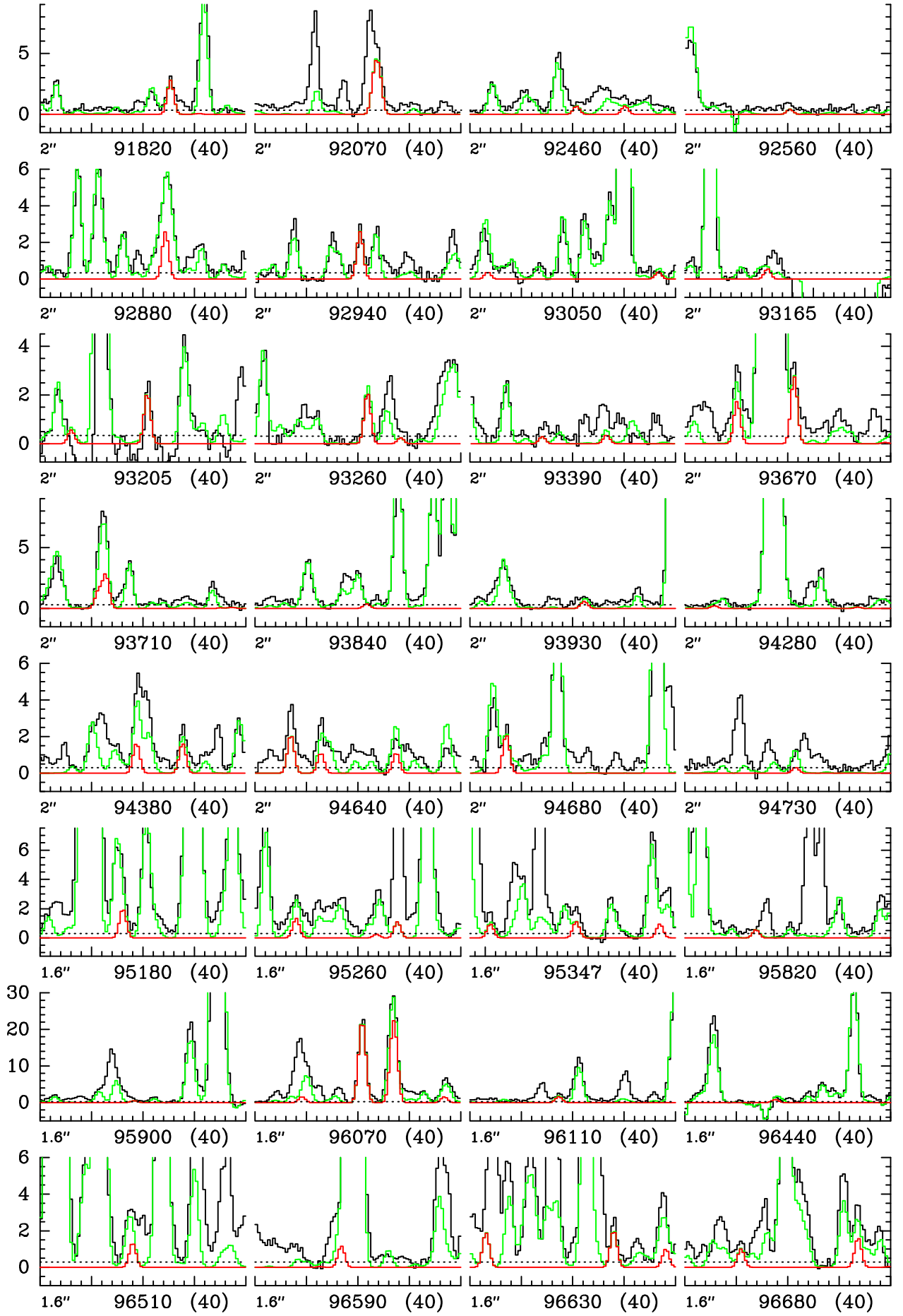


Fig. 71. continued.

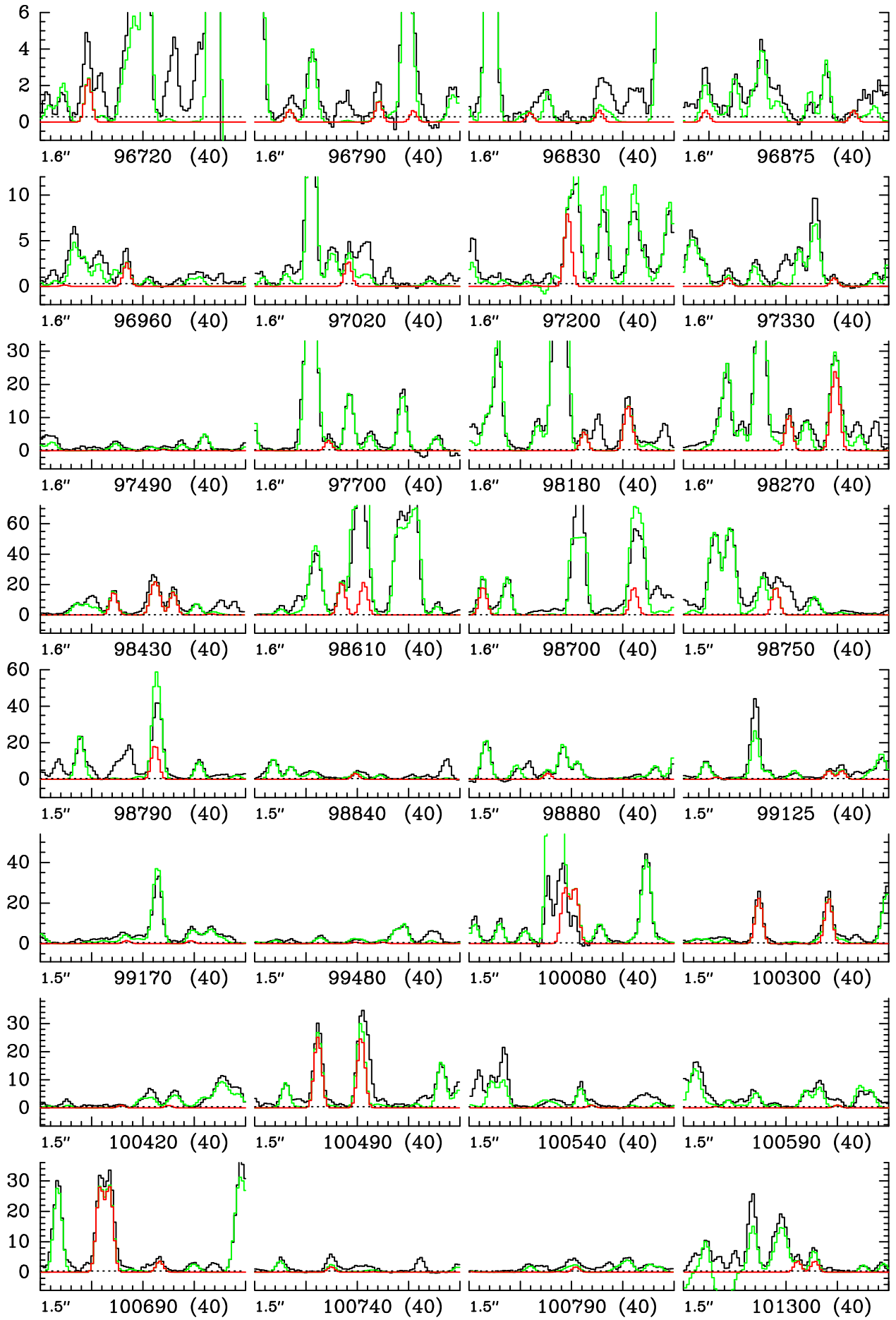


Fig. 71. continued.

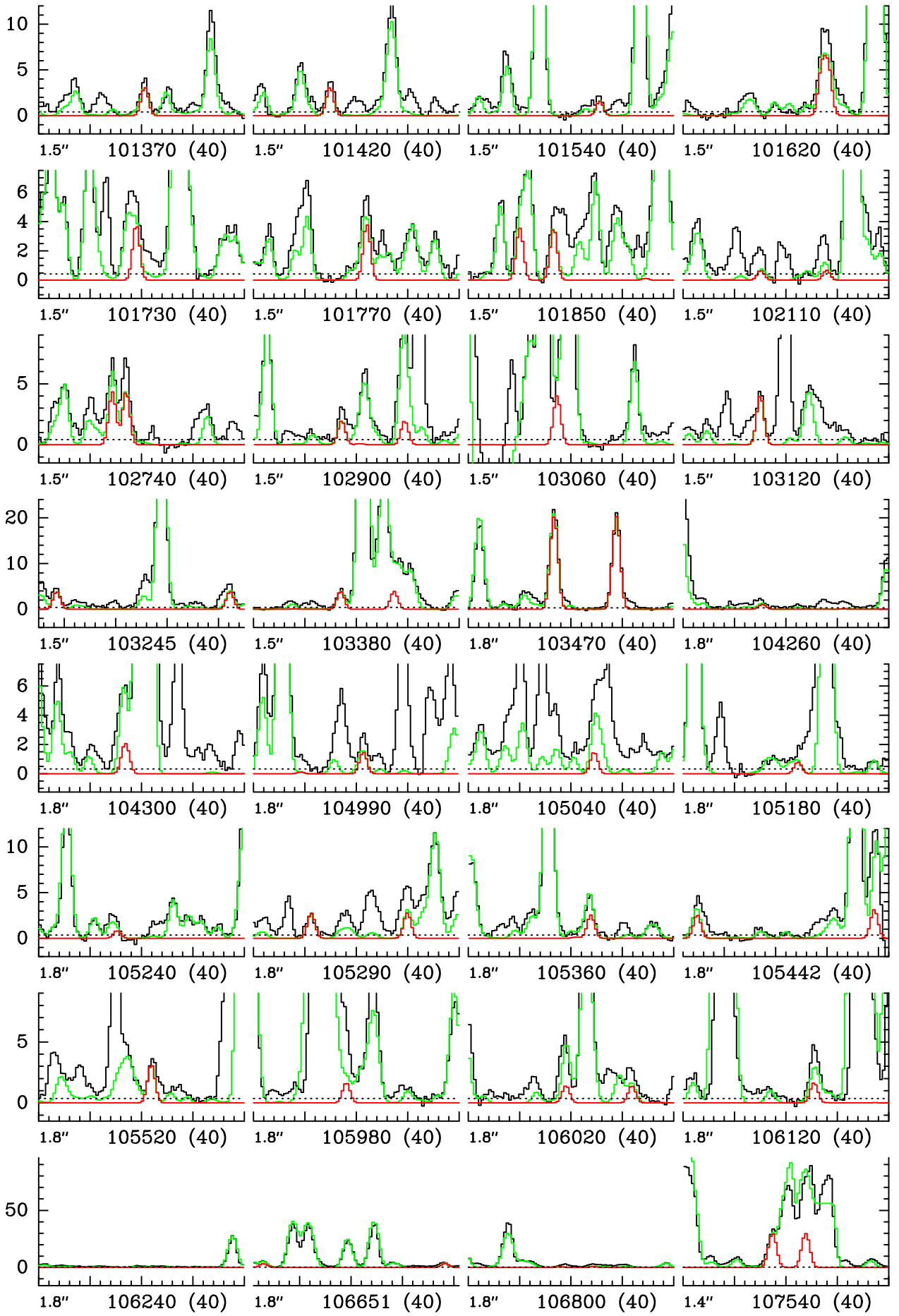


Fig. 71. continued.

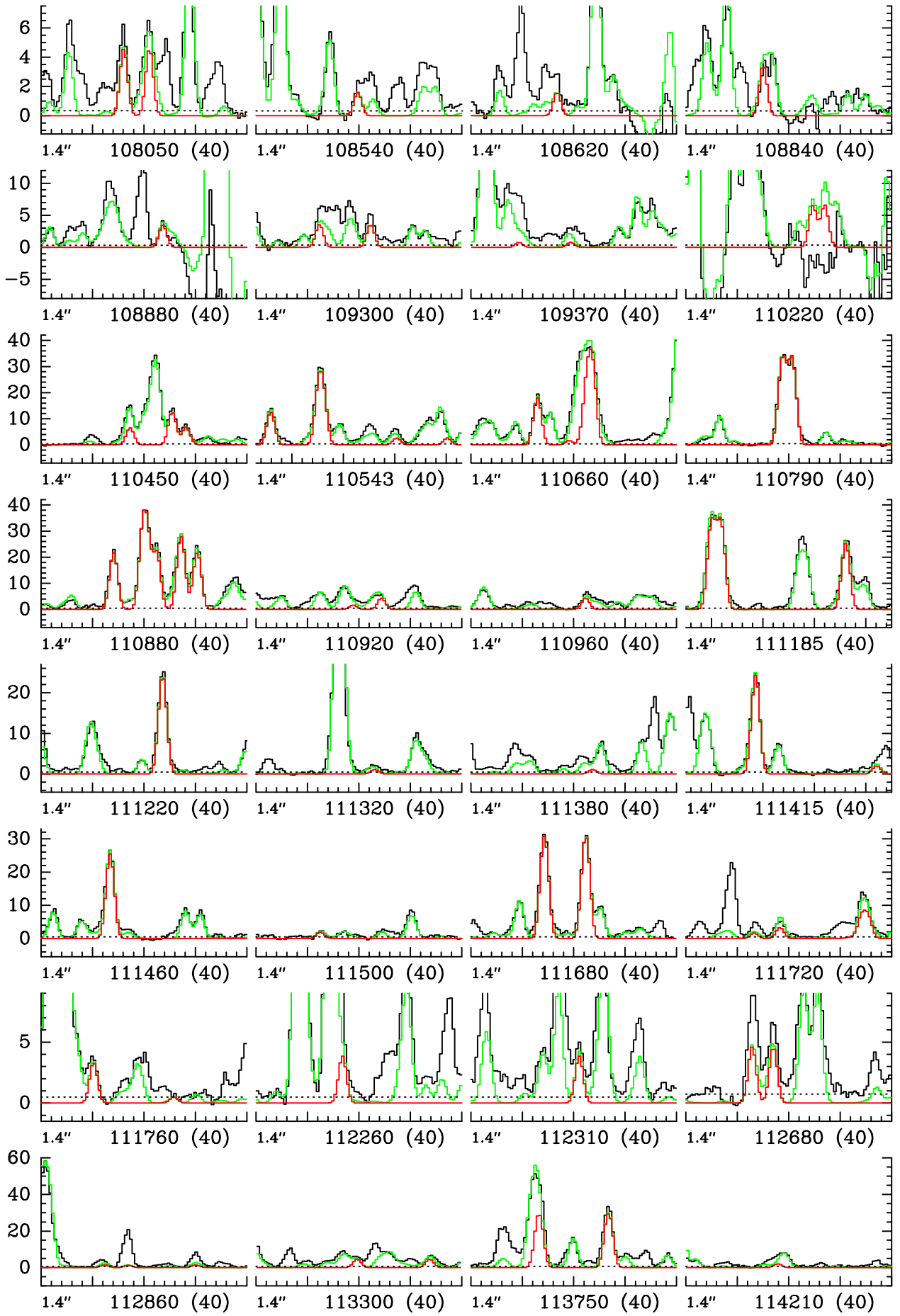


Fig. 71. continued.

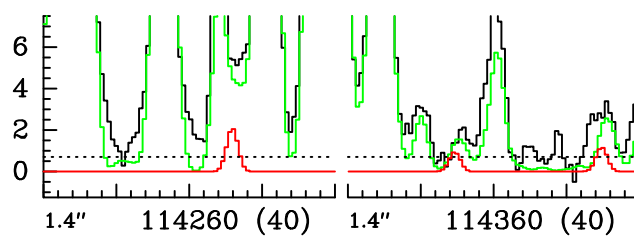


Fig. 71. continued.

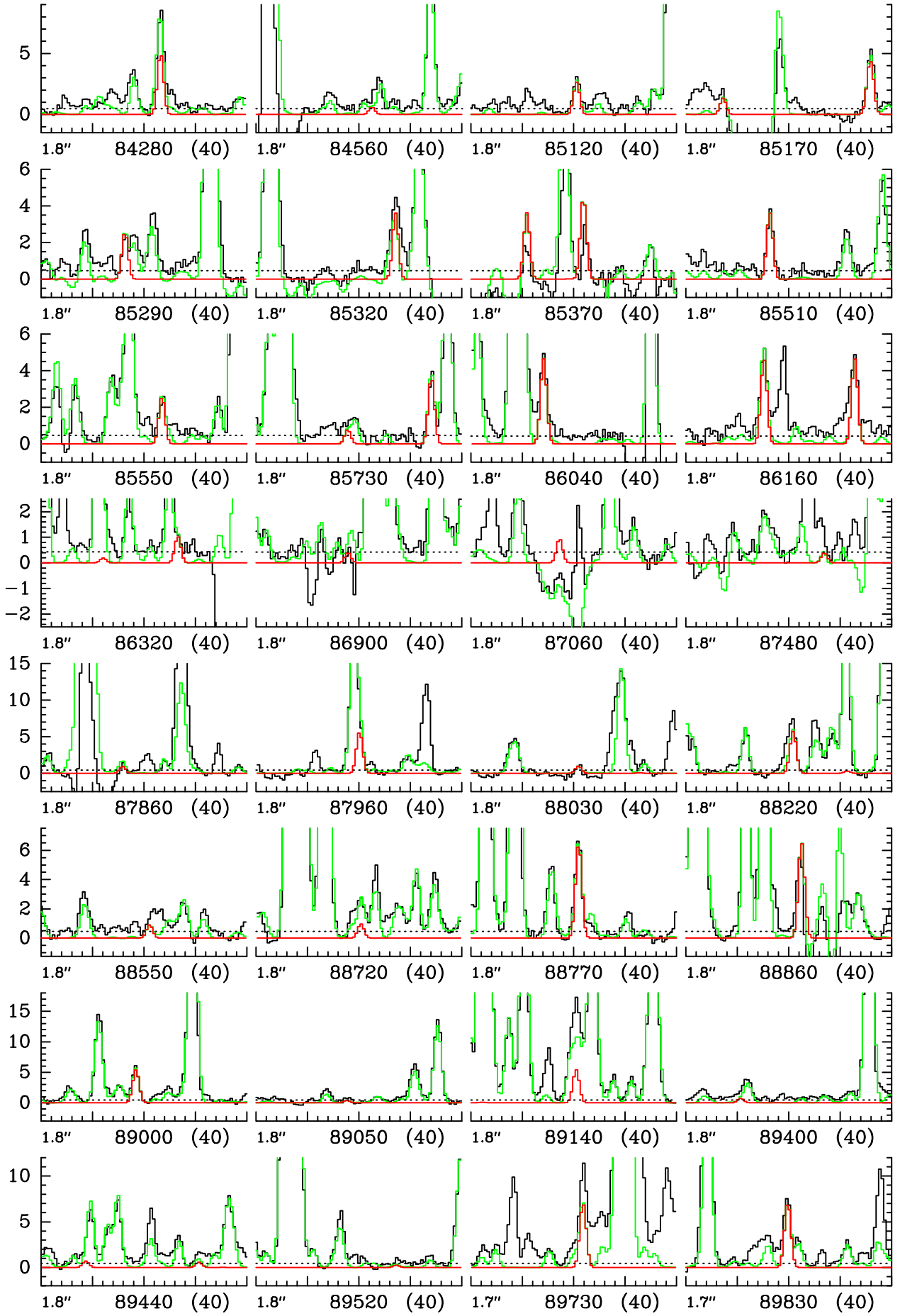


Fig. 72. Same as Fig. 1 for CH_3OCHO , $v_t = 1$.

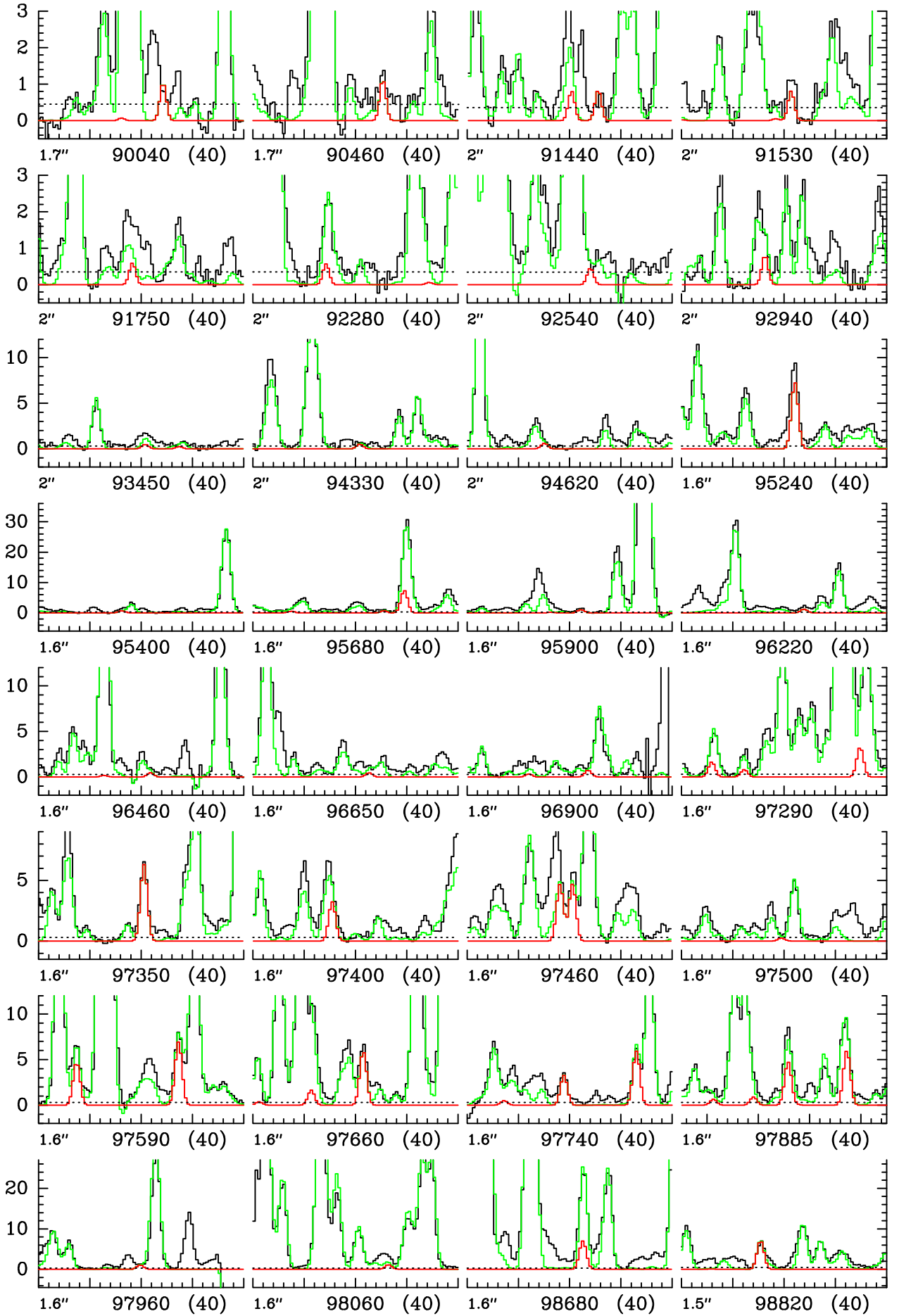


Fig. 72. continued.

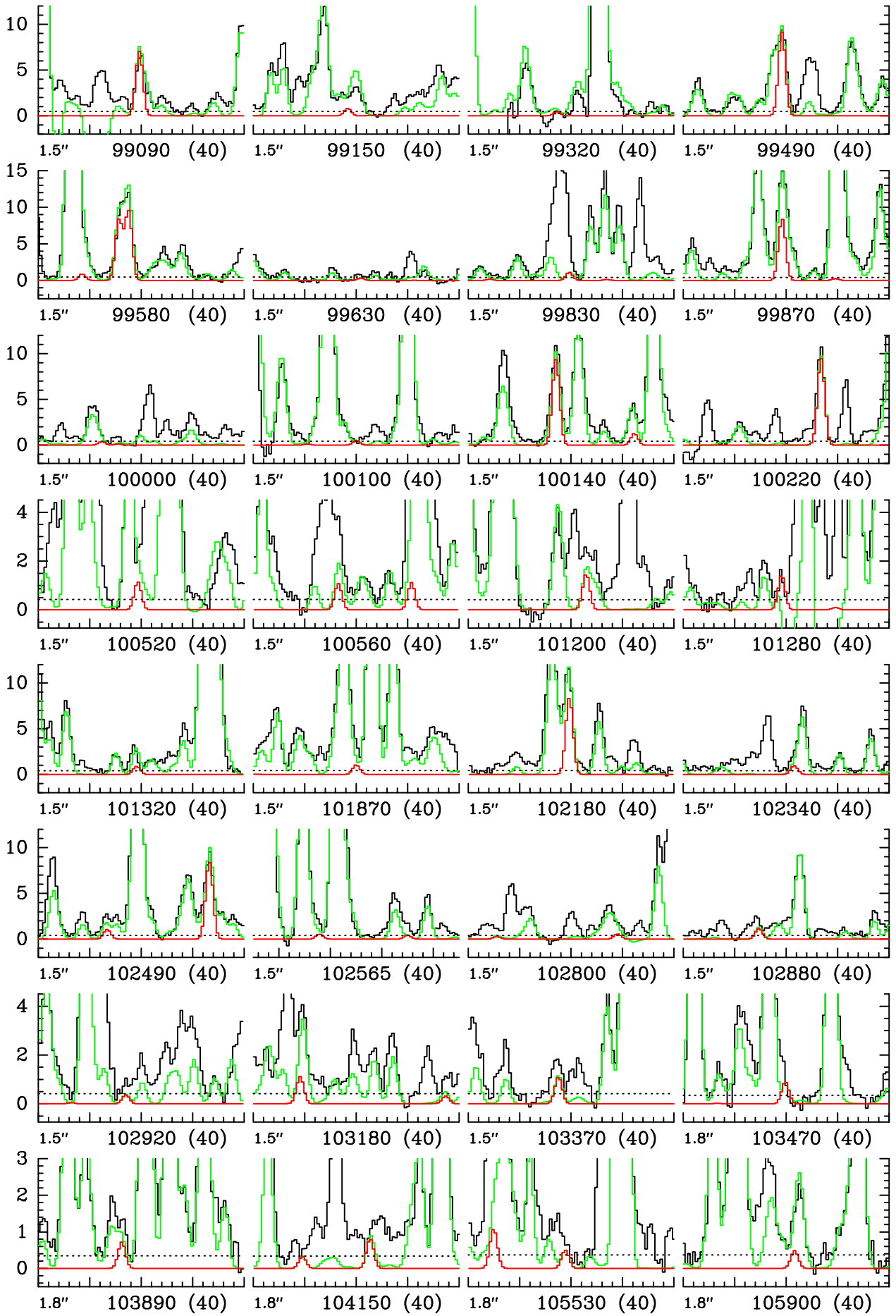


Fig. 72. continued.

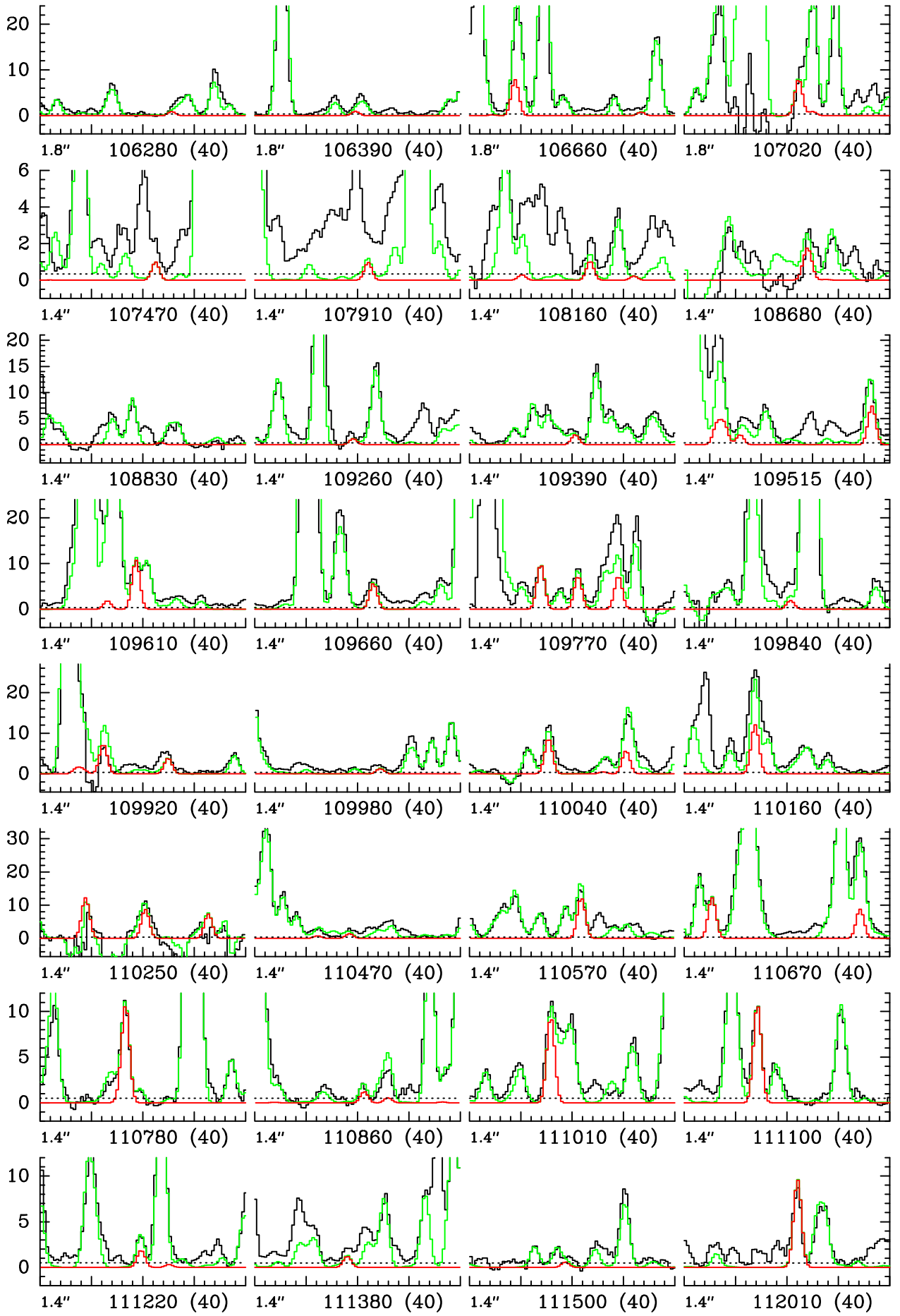


Fig. 72. continued.

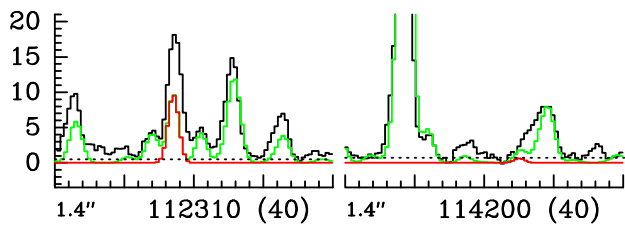


Fig. 72. continued.

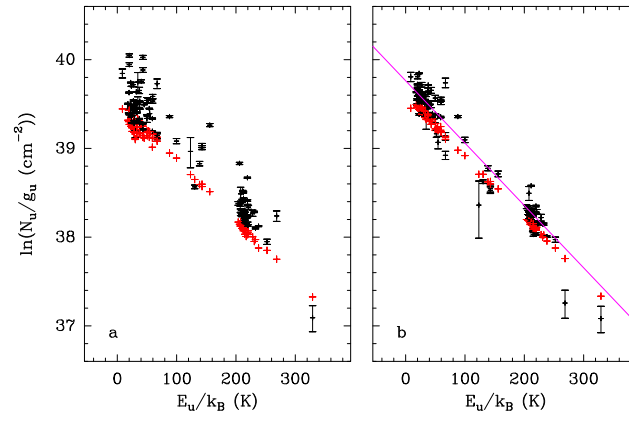


Fig. 73. Same as Fig. 6 for CH_3OCHO , $v_t = 0$ and $v_t = 1$.